

8-2016

Synthesis and Applications of Highly Concentrated Silver Nanoparticles with an Ultra-Thin Silica Shell

Daniel R. Willett
Clemson University

Follow this and additional works at: https://tigerprints.clemson.edu/all_dissertations

Recommended Citation

Willett, Daniel R., "Synthesis and Applications of Highly Concentrated Silver Nanoparticles with an Ultra-Thin Silica Shell" (2016).
All Dissertations. 1689.
https://tigerprints.clemson.edu/all_dissertations/1689

This Dissertation is brought to you for free and open access by the Dissertations at TigerPrints. It has been accepted for inclusion in All Dissertations by an authorized administrator of TigerPrints. For more information, please contact kokeefe@clemson.edu.

SYNTHESIS AND APPLICATIONS OF HIGHLY CONCENTRATED SILVER
NANOPARTICLES WITH AN ULTRA-THIN SILICA SHELL

A Dissertation
Presented to
the Graduate School
of Clemson University

In Partial Fulfillment
of the Requirements for the Degree
Doctor of Philosophy
Chemistry

by
Daniel R. Willett
August 2016

Accepted by:
George Chumanov, Committee Chair
R. Kenneth Marcus
Jeffrey N. Anker
Brian N. Dominy

ABSTRACT

The synthesis of chemically clean silver nanoparticles by hydrogen reduction of silver(I) oxide in water was first reported in our lab by David Evanoff a little over a decade ago, during which these nanoparticles have provided the backbone for research performed in this laboratory. Despite the seemingly relative simplicity of the reaction, much of the intricacies behind it are still being discovered. Presented here we report a proposed mechanism in which the reaction proceeds via a silica catalyzed pathway. In addition, we take advantage of this discovery to greatly increase the concentration of particles obtained as well as generate an ultra-thin silica shell on the surface which provides both a scaffold for functionalization through well-established silane chemistry in addition to imparting excellent stability.

These nanoparticles are then incorporated into substrates for various sensing and detection applications. A sensor based on localized surface plasmon resonance sensing is designed that takes advantage of the ability to assemble these nanoparticles into strongly coupled 2D array. These 2D arrays can then also be used as a simple and effective surfaced-enhanced Raman scattering substrate. A chemiresistor is designed that takes advantage of both the ultra-thin silica shell and high concentrations for vapor sensing applications. They are also cast into 2D & 3D polymer matrixes. It is believed that these nanoparticles hold a unique position in their ability to be easily integrated into numerous analytical techniques that can benefit from having highly concentrated silver nanoparticles with an ultra-thin silica shell as well as having a high potential for commercial viability.

(blank)

DEDICATION

This dissertation is dedicated to Lynn Zhang. Her support and encouragement is the reason I have made it to this stage in my life. She has believed in me and been there to lend a helping hand at every step throughout this process, from grad school applications to dissertation formatting and everything in between. Without her I would not be where I am today. I'm grateful we were able to take this journey together and I look forward to the next step in our life. To our cat, Bean, for keeping me company after Lynn graduated and always being willing to knock something off the counter after my alarm would go off to make sure I didn't fall prey to the snooze button.

This dissertation is also dedicated to the friends I have made here at Clemson University who have helped to keep me sane and make my time in grad school an enjoyable one. To Jamie, Sting & Jerry, we started the program together and though it has been a long journey, I'm glad that we made it through to the end. To Sheng & Ben, you guys helped Lynn and I get started here at grad school and continued helping even after you moved on to post-grad life. To Maria & Tim for being good friends that I could always confide in and count on to be there if I needed anything, even if it was just a night out at Backstreets or a bonfire in my backyard.

“God made the bulk; surfaces were invented by the Devil.”

~ Dr. Wolfgang Pauli

ACKNOWLEDGMENTS

First and foremost, I must thank my advisor Dr. George Chumanov for giving me the opportunity to work in his lab. His focus on teaching fundamentals and analytical thinking above all else, has been pivotal in my ability to tackle the various challenges I encountered both in research and life in general with confidence. From daily conversations on the intricacies behind the nanoparticle synthesis that could immediately turn into discussions on coffee brewing methods or the newest Stone IPA, it all contributed to the learning experience and environment. I would also like to thank my group members, Yi Jin & Yimei Wen. Yi for bringing to the lab his passion for research and learning and Yimei for the charismatic way she approaches all aspects of her life and for brightening the lab with her positive attitude.

I am also grateful to the Kolis, Marcus, Anker, Dominy & Pennington research groups here at Clemson University for providing me opportunities for collaborative research that has helped expand my skill set and to Taghi at the EM lab for his passion in teaching, and occasionally re-teaching, the various electron microscopes at the EM facilities.

TABLE OF CONTENTS

	Page
CHAPTER ONE INTRODUCTION	1
1.1 INTRODUCTION	1
1.1.1 <i>Optical Properties of Metallic Nanostructures</i>	5
1.2 REFERENCES.....	12
CHAPTER TWO ONE-STEP SYNTHESIS AND INVESTIGATION OF HIGHLY CONCENTRATED SILVER NANOPARTICLES WITH AN ULTRA-THIN SILICA SHELL	15
2.1 INTRODUCTION	15
2.2 MATERIALS AND METHODS.....	18
2.2.1 <i>Materials</i>	18
2.2.2 <i>Instrumentation</i>	18
2.2.3 <i>Synthesis of AgNP with UTSS</i>	19
2.2.4 <i>Preparation of 2D Arrays</i>	19
2.2.5 <i>Post-Synthesis Shell Growth and Stability Study</i>	20
2.3 RESULTS AND DISCUSSION	20
2.4 CONCLUSION.....	37
2.5 ACKNOWLEDGEMENTS	38
2.6 REFERENCES.....	38
CHAPTER THREE LSPR SENSOR COMBINING SHARP RESONANCE AND DIFFERENTIAL OPTICAL MEASUREMENTS.....	43
3.1 INTRODUCTION	43
3.2 MATERIALS AND METHODS.....	46
3.2.1 <i>Materials</i>	46
3.2.2 <i>Instrumentation</i>	47
3.2.3 <i>Synthesis of Silver Nanoparticles</i>	49
3.2.4 <i>Fabrication of AgNP Arrays</i>	49
3.2.5 <i>Data Collection</i>	50
3.3 RESULTS AND DISCUSSION	51
3.4 CONCLUSION.....	62
3.5 ACKNOWLEDGMENTS.....	63
3.6 REFERENCES.....	63
CHAPTER FOUR SURFACE-ENHANCED RAMAN SPECTROSCOPY AND CHEMIREISTOR APPLICATIONS.....	68
4.1 INTRODUCTION	68
4.1.1 <i>Surface-Enhanced Raman Spectroscopy</i>	68
4.1.2 <i>Chemiresistor</i>	71
4.2 MATERIALS & METHODS	74
4.2.1 <i>Materials</i>	74
4.2.2 <i>Instrumentation</i>	75
4.2.3 <i>Synthesis of Silver Nanoparticles</i>	75
4.2.4 <i>Preparation of SERS Substrates</i>	76
4.2.5 <i>Preparation of Chemiresistor Vapor Sensor</i>	76
4.2.6 <i>Preparation of 2D & 3D Assemblies of AgNPs in Polymer Matrix</i>	78

Table of Contents (Continued)	Page
4.3 RESULTS AND DISCUSSION	79
4.3.1 Aggregation Study of SERS Substrate.	80
4.3.2 Chemiresistor Vapor Sensor.....	88
4.3.3 Fabrication of 2D & 3D Assemblies of AgNPs in a Polymer Matrix.....	95
4.4 CONCLUSIONS	98
4.5 ACKNOWLEDGEMENT.....	98
4.6 REFERENCES.....	99
CHAPTER FIVE SUMMARY & FUTURE WORK.....	103
APPENDICES.....	106
APPENDIX A. SYNTHESIS OF COPPER IODIDE NANOPARTICLES FOR DENTAL ADHESIVE APPLICATIONS.....	107
A.1 INTRODUCTION	107
A.2 MATERIALS & METHODS	108
A.2.1. Synthesis of PAA Coated Copper Iodide Nanoparticles.....	108
A.3 REFERENCES.....	111
APPENDIX B. SINGLE CRYSTAL RAMAN SPECTROSCOPY OF $\text{Ca}_{19}\text{Al}_{13}\text{Si}_{18}\text{O}_{71}(\text{OH})_7$.....	114
B 1. INTRODUCTION	114
B 2. EXPERIMENTAL	114
B 3. DISCUSSION	115
B 4. CONCLUSION	119
B 5. ACKNOWLEDGEMENT	120
B 6. REFERENCES	121

LIST OF FIGURES

Figure	Page
Figure 1.1 Graphical representation for the one-step synthesis resulting in AgNPs with an ultra-thin silica shell	2
Figure 1.2 Graphical representation of the entire LSPR sensor using differential optical measurements.....	3
Figure 1.3 Aliquots taken from a single reaction vessel in 15 minute intervals for AgNPs grown to 125 nm in diameter.	6
Figure 1.4 Schematic of plasmon oscillation for a metal sphere showing the displacement of the conduction electron charge cloud relative to the nuclei.....	7
Figure 1.5 SEM of AgNPs grown by hydrogen reduction method to ~300 nm in size.	8
Figure 1.6 UV-Vis spectra of AgNPs grown to 300 nm in size with spectra taken every 1 hour.....	10
Figure 1.7 UV-Vis showing shift in plasmon resonance as environment changed from water (black) to ethanol (blue) resulting in a red shift due to the increase in refractive index of the medium.....	11
Figure 2.1 UV-Vis spectra of (A) 10 mM Ag ₂ SO ₄ under H ₂ for 2 hours (B) following addition of 3 mM Na ₂ SiO ₃ (C) after reaction placed back under H ₂ for 1 hour (10x dilution). All steps were performed in a Teflon® reactor.	23
Figure 2.2 Size distribution analysis of 50 AgNPs giving a size distribution of 114.53 ± 3.75 nm to demonstrate the monodispersity of the AgNPs obtained via this method.	26
Figure 2.3 SEM images of AgNPs grown to 100 nm in Pyrex® (A) and AgNPs grown to 100 nm in quartz with the addition of 1 mM fumed silica (B)	27
Figure 2.4 UV-Vis of polyhedron (blue) and spherical (black) AgNPs with accompanying SEM images.	28
Figure 2.5 UV-Vis of 2D array of AgNPs exposed to saturated silver(I) oxide water (A) and ultra-pure water (B) showing the degradation of the 353 nm peak. Spectra taken immediately (black), 1 day (blue) and 3 days (red) later.	29

Figure 2.6 HR-TEM images of AgNPs grown to 100 nm in Pyrex® without additional silica show a ~1.1 nm silica shell.....	30
Figure 2.7 TEM of AgNPs grown with 0.8 mM Na ₂ SiO ₃ taken at 30 minutes (A) and 4 hours (B) & AgNPs grown with 1 mM fumed silica taken at 30 minutes (C) and 4 hours (D).....	32
Figure 2.8 TEM images of AgNPs grown to ~50 nm AgNP with 0.8 mM (A) and 6 mM (B) of sodium silicate added. (A) with an O.D. of 2.7 was obtained after 30 minutes while (B) an O.D. of 84 required 5 hours.	33
Figure 2.9 HR-TEM images of AgNPs grown to ~250 nm (A) and ~400 nm (B) with 1.27 & 0.5 mM fumed silica, respectively.	34
Figure 2.10 UV-Vis and TEM of AgNPs with 1.6 nm Si shell after introduction of 0 mM (A) 1 mM (B) & 2 mM (C) Na ₂ SiO ₃ and addition to EtOH.....	35
Figure 2.11 UV-Vis of AgNPs with 1 nm Si shell (A) and 15 nm Si shell (B) after exposure to 3 mM Na ₂ S over a period of 20 hours.	36
Figure 3.1 Graphic demonstrating the method for differential measurements using the sharp plasmon resonance achieved from 2D arrays of AgNPs.....	46
Figure 3.2 Schematic of the differential LSPR instrumentation.....	48
Figure 3.3 Photo of completed differential LSPR instrumentation.....	49
Figure 3.4 Coherent plasmon coupling in 2D array (black) and the same AgNPs in the suspension (blue). Inset: EM images of a coupled 2D array.....	52
Figure 3.5 UV-Vis of coupling as a result of sodium sulfate concentration of AgNPs in 2D arrays for 0 mM (a) 0.5 mM (b) 1 mM (c) 1.5 mM (d) & 2 mM (e) salt concentrations.....	54
Figure 3.6 UV-Vis of a 2D array demonstrating how the resonance blue shifts and sharpens over a period of 3 days. Inset is zoomed in view of peak region.	55
Figure 3.7 Spectral shift of the resonance after changing the refractive index of the medium by 1.4E-3 units and measured using conventional UV-Vis spectroscopy. Inset: Magnified region around the peak of the resonance.	57
Figure 3.8 Linear relationship between the differential signal and the change of the refractive index.....	59
Figure 3.9 Differential signal as a function of serial addition of sucrose solution. Vertical lines correspond to the noise spikes due to the injection. Percentages	

correspond to final concentration of sucrose in solution. Data was collected for 2.5 minutes before next addition was performed.	60
Figure 3.10 Data collected after inducing a change in refractive index of $1.4E-562$	
Figure 4.1 Energy level diagram illustrating Rayleigh, Stokes & anti-Stokes scattering.	69
Figure 4.2 Basic schematic of a simple chemiresistor.	72
Figure 4.3 Picture of entire chemiresistor setup & sampling method.	78
Figure 4.4 SEM images of 2D array dried from a low surface tension solvent (left) and water (right).....	81
Figure 4.5 UV-Vis of slide exposed to 1 mM guanine in water before (black) and after (blue) drying. Insert: SEM of slide after drying.	82
Figure 4.6 SERS of 2D arrays of AgNPs exposed to 10 μ M guanine (a) & 10 μ M adenine (b) in water (1) then dried to induce aggregation and back in water (2)	84
Figure 4.7 SERS of 1 μ M ssDNA on 2D array of AgNPs before (black) and after (blue) drying. Spectra taken in water in both cases.	86
Figure 4.8 SERS of quinoxalinol salen ligand bound to uranyl ion after 10 minutes (a), 1 day (b) 4 days (c) and the ligand itself after 4 days (d) to show time release of uranyl species into DI water.	88
Figure 4.9 Photo of sensor taken on an optical microscope under 20x objective. Insert shows the AgNP distribution on the edges of the sensor.....	90
Figure 4.10 SEM of 2.5 μ L of O.D. 2500 AgNPs (510 nm dipole) used to fabricate chemiresistor.....	91
Figure 4.11 Conductivity response for air, water vapor & acetone vapor over a period of 500 seconds at a potential of +1 V. Water & acetone were introduce on and off for 50 seconds starting at 50 seconds to show reversible response.	93
Figure 4.12 Conductivity response for air, water vapor & acetone vapor over a period of 500 seconds at a potential of -0.05 V. Water & acetone were introduce on and off for 50 seconds starting at 50 seconds to show reversible response. .	94
Figure 4.13 UV-Vis spectra of “conditioned” AgNP solution (black), prepared casting solution (blue) and polymerized film (red). Note: Spectra are offset to the quadrupole of “conditioned” solution for easier comparison of resulting shift.....	96

Figure 4.14 UV-Vis spectra of 2D array of AgNPs in water (black), dry (blue) and embedded into polymerized PEGMDA film (red)	97
Figure A.1 SEM from the synthesized CuI nanoparticles demonstrating polydispersity in size.	109
Figure A.2 EDX spectrum (a) from the selected area of the sample outlined by the magenta triangle (b). The measured elemental composition is in the figured table	110
Figure. B.1 Schematic & microscope image illustrating laser illumination along the crystallographic c-axis using a 20x objective prior to micro-Raman measurements.	115
Figure. B.2 Schematic & microscope image illustrating laser illumination along the crystallographic a/b-axis using a 20x objective prior to micro-Raman measurements	116
Figure. B.3 Raman of a/b-axis with P-polarized (A) 7 S-polarized (B) light. Raman of c-axis with P-polarized (C) & S-polarized (D) light. Literature Raman spectra of vesuvianite from RRUFF database for P-polarized (E) & S-polarized (F) light.	118
Figure. B.4 Zoomed in region of the Raman of the a/b-axis with P-polarized (A) & S-polarized (B) light to highlight the area with the most differences between the two polarizations.	119

CHAPTER ONE

INTRODUCTION

1.1 Introduction

Materials on the nanoscale can exhibit unique properties that are not observed or present for the same material on the macroscopic scale. As a result of this, new and unique properties of nanoparticles, assemblies and composites are constantly being discovered. To facilitate these advances it is important to have large scale and reproducible synthesis of nanomaterials with long shelf lives and excellent stability. The difficulty in producing these nanomaterials in the desired size and shape continues to press the need for new and refined synthetic techniques. While top-down approaches such as lithographic techniques can allow for precise and reproducible control of nanostructures they are typically limited in the total area they can fabricate while also requiring expensive and specialized equipment to produce.¹ This dissertation will focus on a bottom-up approach to synthesis silver nanoparticles (AgNPs) and fabricating them into various substrates for applications including localized plasmon resonance (LSPR) sensing, surface-enhanced Raman spectroscopy (SERS) and chemiresistors.

In Chapter 2 a novel one-step synthesis of AgNPs with an ultra-thin silica shell is described (**Figure 1.1**). This synthesis is derived from the original hydrogen reduction method developed in this lab² and results in highly concentrated spherical silver nanoparticles from 40-400 nm with an ultra-thin silica shell from 1-

5 nm that provides a scaffold for well-developed silane chemistry for further functionalization. These nanoparticles exhibit remarkable stability and can be concentrated to as high as 50% by weight in water and some organic solvents. In addition this chapter introduces the first observation that silica species catalyze the seeding and growth of silver nanoparticles. This work has been submitted to *RSC Advances*. These AgNPs are then incorporated into various applications in the following chapters.

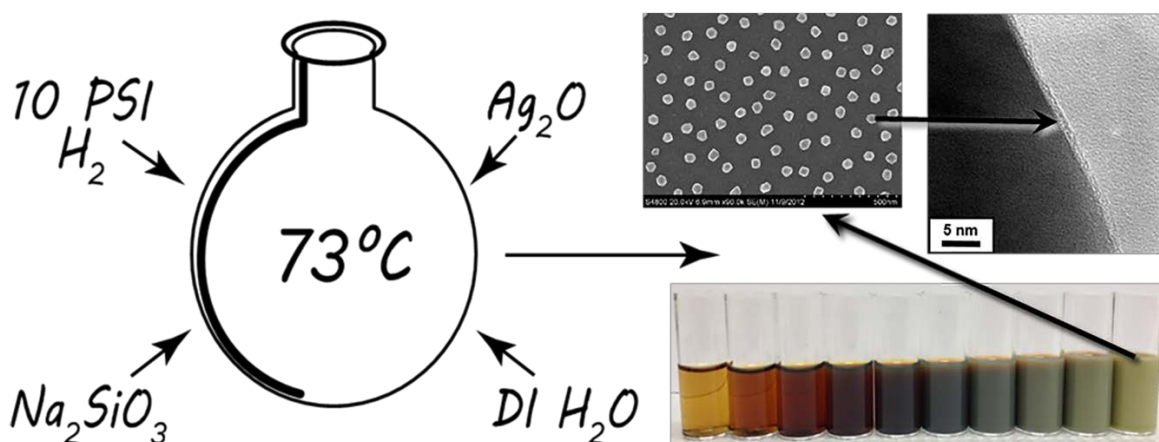


Figure 1.1 Graphical representation for the one-step synthesis resulting in AgNPs with an ultra-thin silica shell

Chapter 3 focuses on work published in *Plasmonics* incorporating the AgNPs with an ultra-thin silica shell into self-assembled 2D arrays and then designing a new optical sensor based on LSPR. The 2D arrays result in a coherent plasmon coupling that manifests as a sharp peak in the blue spectral region. To take advantage of this sharp resonance, a differential optical measurement method was developed in which the LSPR shift was monitored by measuring the difference between light extinction at two different wavelengths selected on either side of the

peak (**Figure 1.2**). This sharpness of the peak combined with the differential measurement method enabled an extremely high sensing resolution in bulk for a LSPR sensor. The citation for the manuscript is as follows:

Willett, D. R.; Chumanov, G., LSPR Sensor Combining Sharp Resonance and Differential Optical Measurements. *Plasmonics* **2014**, 9 (6), 1391-1396.

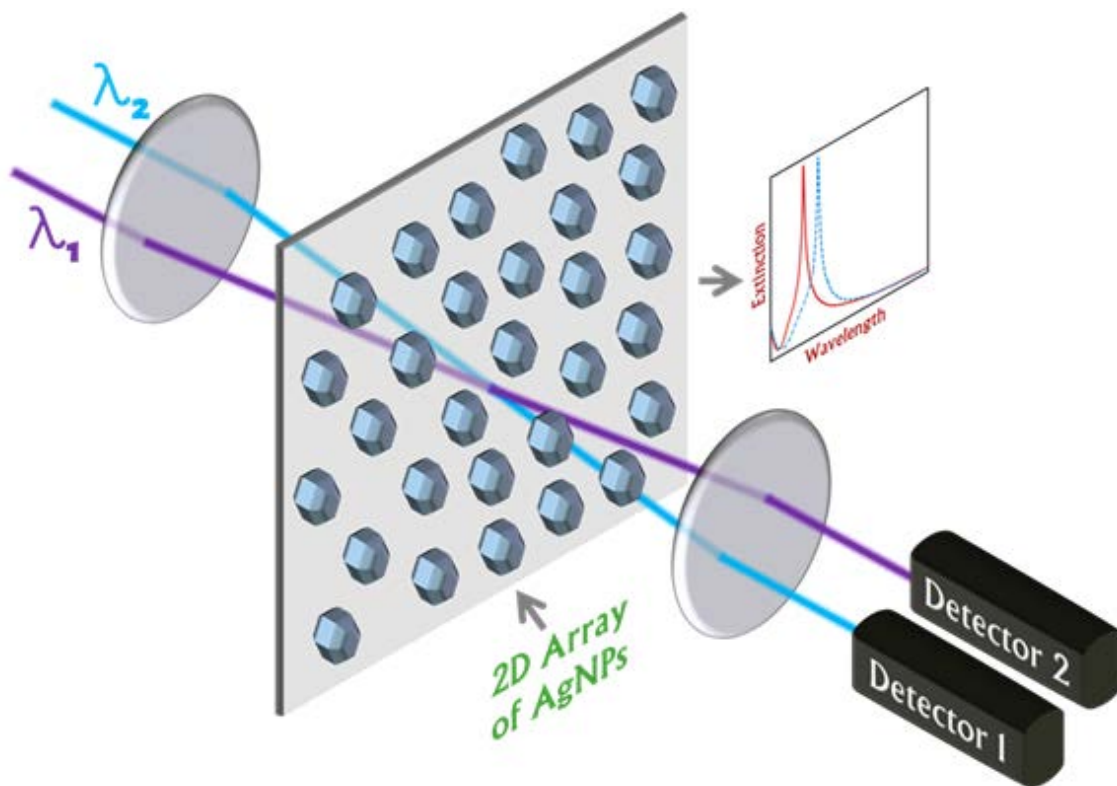


Figure 1.2 Graphical representation of the entire LSPR sensor using differential optical measurements.

Chapter 4 involves two currently unpublished applications. The first part will discuss taking advantage of the ultra-thin silica shell to incorporate these nanoparticles into applications involving shell-isolated nanoparticle enhanced Raman spectroscopy (SHINERS). In particular, this will focus on the SERS enhancement obtained from induced aggregation of AgNPs to sandwich analytes

between nanoparticles on 2D arrays. The second part will take advantage of both the ultra-thin silica shell and the extremely high concentration that can be obtained to develop a solid-state electrochemical sensor in which the particles are drop-dried between two electrodes and the current across this system is monitored. Different vapors are introduced that elicit a response in the current monitored which is reversible when they are removed. Finally we demonstrate their ability to be incorporated into 2D & 3D polymer matrices. Chapter 5 provides a general conclusion about the research findings with some possible direction for future work. In the appendixes is collaborative work with outside groups that didn't fit in the big picture of this dissertation involving unpublished single crystal Raman studies as well as the synthesis of copper iodide nanoparticles for dental applications with the following citation:

Renne, W. G.; Lindner, A.; Mennito, A. S.; Agee, K. A.; Pashley, D. H.; **Willett, D. R.**; Sentelle, D.; Deffe, M.; Schmidt, M.; Sabatini, C., Antibacterial Properties of Copper Iodide Doped Glass Ionomer-based Materials and Effect of Copper Iodide Nanoparticles on Collagen Degradation. *Clinical Oral Investigations* **In Press**.

In addition to the studies discussed above, I collaborated in projects involving Raman characterization of various complex inorganic vanadate crystals grown by hydrothermal synthesis in Dr. Kolis' group at Clemson University. The citations for these manuscripts are as follows:

Sanjeewa, L. D.; McMillen, C. D.; **Willett, D. R.**; Chumanov, G.; Kolis, J. W., Hydrothermal Synthesis of Single crystals of Transition Metal Vanadates in the Glaserite Phase. *J. Solid State Chem.* **2016**, 236, 61-68.

Sanjeewa, L. D.; McGuire, M. A.; Pellizzeri, T. M.; McMillen, C. D.; Garlea, V. O.; **Willett, D. R.**; Chumanov, G.; Kolis, J. W., Synthesis and Characterization of New Fluoride-Containing Manganese Vanadates $A_2Mn_2V_2O_7F_2$ ($A=Rb, Cs$) and Mn_2VO_4F . *J. Solid State Chem.* **In Press.**

Sanjeewa, L. D.; McGuire, M. A.; McMillen, C. D.; Garlea, V. O.; **Willett, D. R.**; Chumanov, G.; Kolis, J. W., Honeycomb-like $S = 5/2$ Spin Lattices in New Manganese(II) Vanadates. *Inorganic Chemistry*. **Submitted.**

In a separate study, the LSPR wavelength of the AgNPs synthesized by the modified hydrogen reduction method were tuned by mechanical deformation in Dr. Ankers' group at Clemson University and thoroughly characterized. This technique of mechanical deformation required no lithographic templates and thus has the potential for quick, reliable, low-cost and scalable tuning of nanoparticle shape, surface area and LSPR while maintaining particle volume. The citation is as follows:

Ameer, F. S.; Varahagiri, S.; Benza, D. W.; **Willett, D. R.**; Wen, Y.; Wang, F.; Chumanov, G.; Anker, J., Tuning Localized Surface Plasmon Resonance Wavelengths of Silver Nanoparticles by Mechanical Deformation. *J. Phys. Chem.* **In Press.**

These publications are not discussed further in this dissertation.

1.1.1 Optical Properties of Metallic Nanostructures

Since they were first reported by Michael Faraday in the mid 1800's, who observed that the optical properties of gold colloids differed from the bulk metal, metallic nanoparticles have been of great interest for a wide variety of applications due to their outstanding optical, catalytic and electronic properties.³ These properties and resulting integration into these various applications are largely determined by the morphological characteristics such as size and shape. Of all

the metallic nanoparticles, silver is of particular interest because it undergoes the most efficient interaction with light compared to any other metal nanoparticle or known inorganic or organic chromophore.⁴ The optical cross-section of AgNPs is almost five times that for similarly sized gold nanoparticles.⁵ The light-interaction cross section for silver can be approximately ten times that of the geometric cross-section meaning that the AgNPs are able to capture more light than is physically incident on them.⁶ AgNPs can also be tuned to have a maximum at any wavelength in the visible spectrum. **Figure 1.3** shows the color change of AgNP colloid as the size increases from 30 nm to 125 nm. AgNPs must be small enough that the optical properties change with AgNP size, shape and local dielectric (less than the wavelength of incident light), but must be large enough to have free electron density (c.a. 10 or more atoms).⁷ While gold nanoparticles are still used for many applications where their stability and resistance to oxidation is of primary importance, this dissertation will focus on synthesis and optical applications of AgNPs utilizing an ultra-thin silica shell to promote stability and assist in alleviating issues with oxidation.



Figure 1.3 Aliquots taken from a single reaction vessel in 15 minute intervals for AgNPs grown to 125 nm in diameter.

The optical properties are mainly dominated by surface plasmon resonances which are collective oscillations of conduction electrons on the surface of the particles. When a surface plasmon is confined to a small domain, such as that represented by a nanoparticle, the resulting induced electric field is enhanced in the region of the nanoparticle. When incoming light waves are incident on metallic nanoparticles the electric field induces a polarization of the electrons. As a result of this, a net charge difference occurs on the surface of the nanoparticles giving a strong localized electric field that extends from the surface of the nanoparticles as can be seen in **Figure 1.4**. It is this strong localized electric field from these surface plasmons that is attributed to many of the optical enhancements resulting from metallic nanoparticles.⁸ When the particles are spherical and smaller than the wavelength of the incident light the localized electric field can be treated as an oscillating dipole.

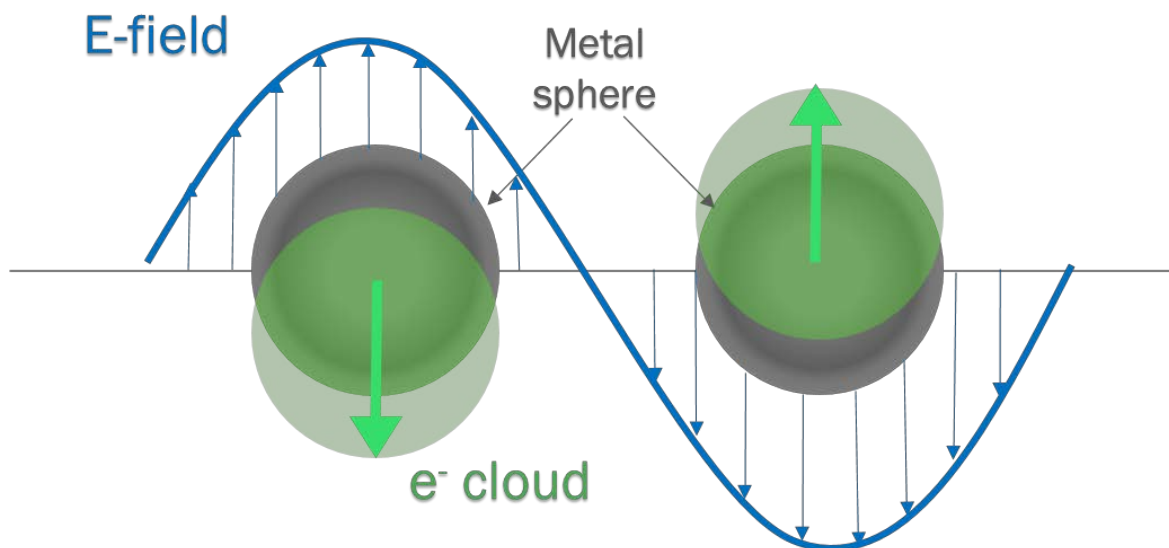


Figure 1.4 Schematic of plasmon oscillation for a metal sphere showing the displacement of the conduction electron charge cloud relative to the nuclei.

These surface plasmon resonances can be visualized by their strong UV-Vis extinction band of which the magnitude, shape and peak wavelength are dependent on the particle's shape, size and dielectric function of the particle and the surrounding medium.⁹ The plasmon resonance for spherical AgNPs scales with the diameter of the particle. **Figure 1.5** shows a scanning electron microscope (SEM) image to demonstrate the polyhedron shape of the AgNPs used throughout this dissertation and shows the high degree of crystallinity.

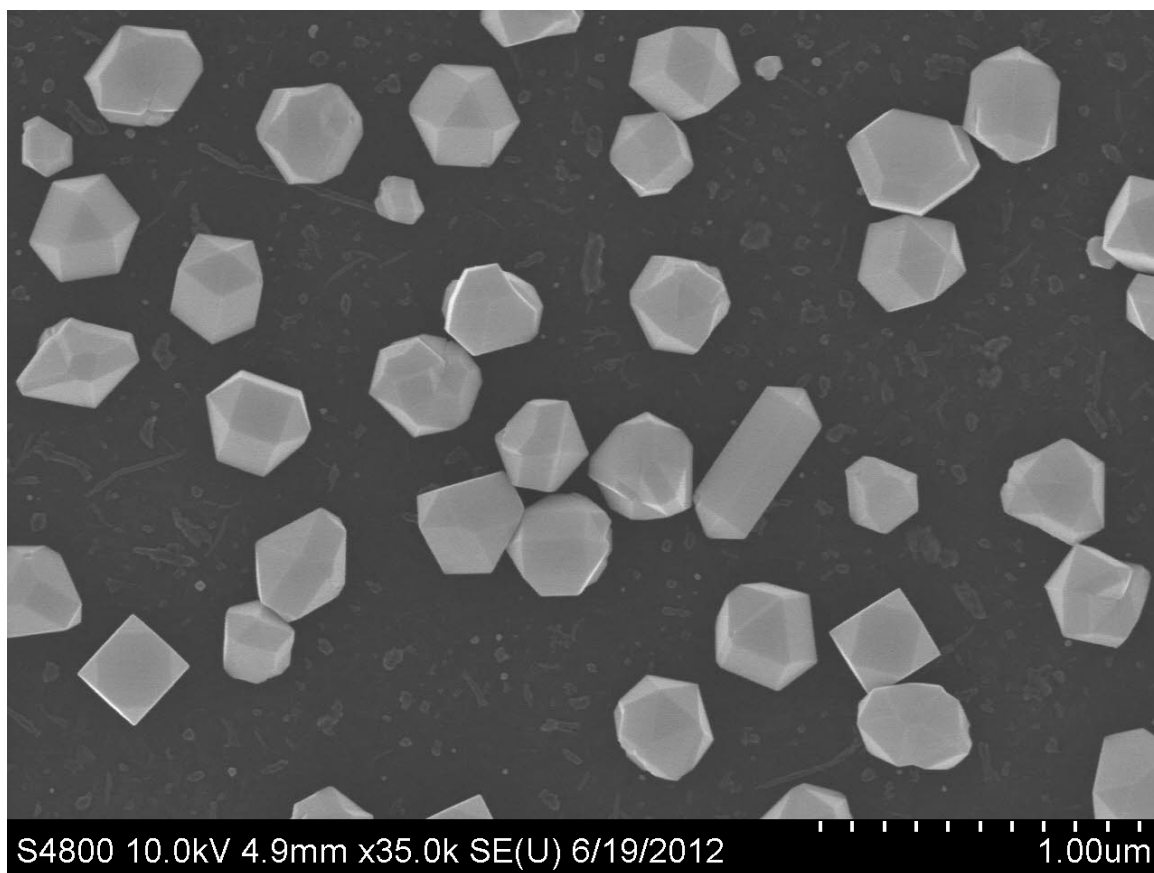


Figure 1.5 SEM of AgNPs grown by hydrogen reduction method to ~300 nm in size.

The shape of the extinction band corresponding to the plasmon resonance remains as a single peak until the AgNP diameter approaches the wavelength of incident light. When this happens, the phase of the electric vector of light experiences retardation across the AgNP resulting in multipolar oscillation of the electron density. The efficient emission (scattering) of photons reduces the lifetime of the plasmon oscillations and broadens the plasmon band.¹⁰ As the particles grow in size the plasmon peak experiences a red shift and the plasmon bandwidth also increases due to the excitation of multipole modes (dipole, quadrupole, octapole, etc) that yield a larger contribution as size increases (**Figure 1.6**). **Figure 1.6** shows the spectra of AgNPs grown for a period of 12 hours to a size of ~300 nm with UV-Vis taken every 1 hour. The resulting spectra is raw unscaled data from the reaction. As the AgNPs grow larger in size the dipole first appears followed by the resulting multipoles as the dipole is shifted far into the red with the final 300 nm AgNPs demonstrating the appearance of the hexadecapole. As illustrated in **Figure 1.4**, the excitation of plasmon resonances in AgNPs produces a local electromagnetic field that extends into the surrounding environment from the particle surface. This field is 'enhanced' compared to the incident field, in our lab it was experimentally demonstrated that for ~85 nm AgNPs the local electromagnetic field extended approximately $\frac{1}{2}$ the AgNP diameter.¹¹

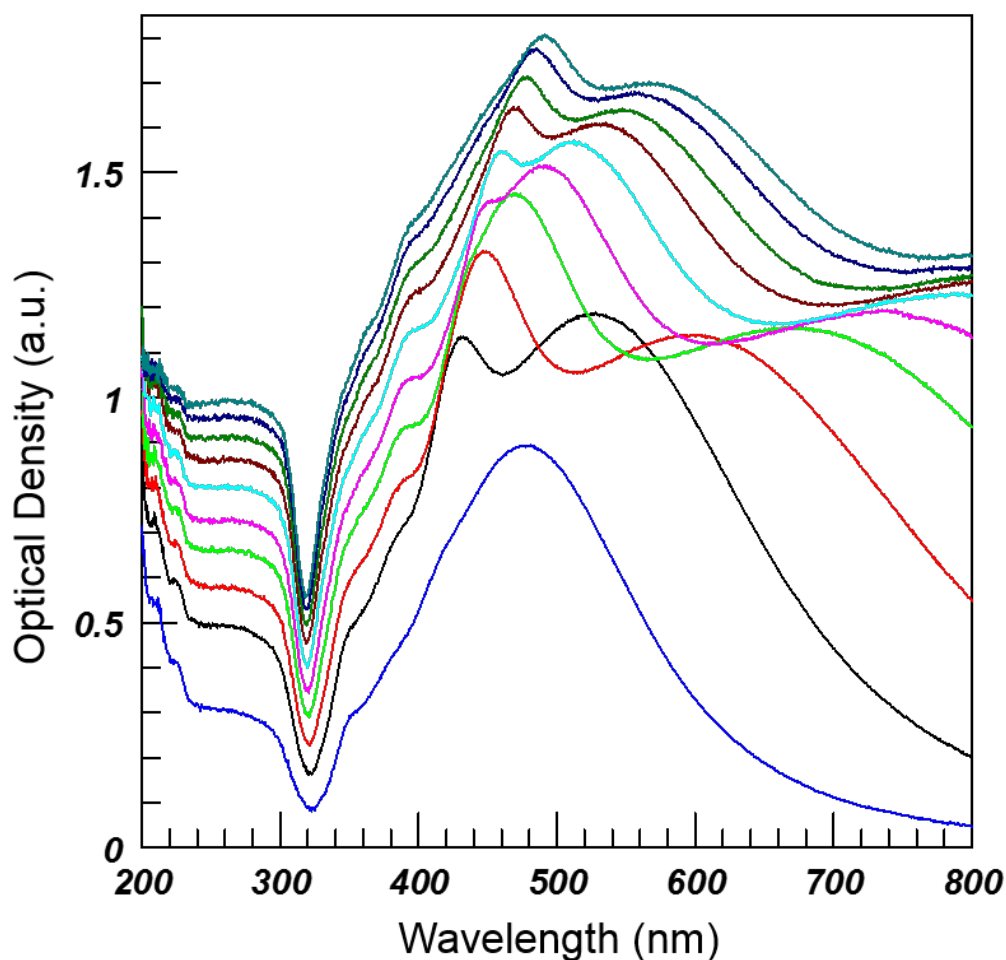


Figure 1.6 UV-Vis spectra of AgNPs grown to 300 nm in size with spectra taken every 1 hour.

Discussion thus far has centered on AgNPs in suspension, when the same particles are assembled into 2D arrays they exhibit new optical properties that are not observed for colloids. When the particles are spaced close enough, the local electromagnetic fields for the individual particles can overlap with their neighbors resulting in plasmon coupling. This resulting plasmon coupled peak will still be dependent on the particle size, shape and local dielectric environment in addition to interparticle spacing and the nature of the supporting substrate.^{6, 12} Theoretical calculations show that when the interparticle distance is comparable to the

diameter of the nanoparticle, then coupling occurs.¹¹ As the refractive index of the local dielectric environment around the particle increases, a red-shift of the plasmon coupled peak is observed as can be seen in **Figure 1.7** where a 2D array was exposed to water and then ethanol.¹³ In our laboratory we have assembled 2D arrays of AgNPs that result in a sharp band in the blue spectra region corresponding to a coherent plasmon mode.^{12b} No other experimental observations of this sharp band have been reported in the literature, however it has been theoretically calculated by other groups.¹⁴ The sensitivity of this sharp resonance that occurs in 2D arrays is exploited in the LSPR sensor discussed in Chapter 3.

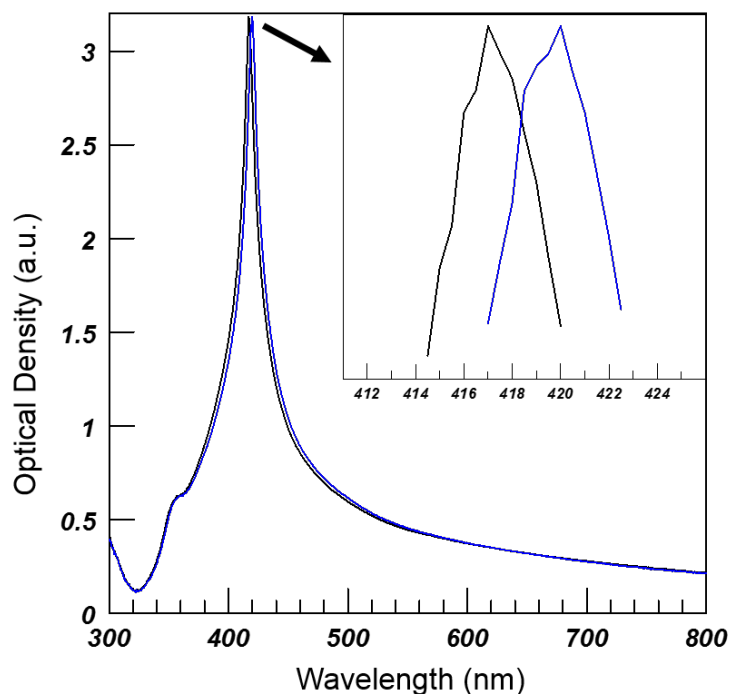


Figure 1.7 UV-Vis showing shift in plasmon resonance as environment changed from water (black) to ethanol (blue) resulting in a red shift due to the increase in refractive index of the medium.

1.2 References

1. Wang, Q.; Yu, C. X., Chemical and Biological Sensing and Imaging Using Plasmonic Nanoparticles and Nanostructures. In *Biomedical Nanosensors*, Irudayaraj, J., Ed. Pan Stanford Publishing Pte. Ltd.: Singapore, 2013; Vol. 3, pp 59-96.
2. Evanoff, D. D.; Chumanov, G., Size-controlled Synthesis of Nanoparticles. 1. "Silver-only" Aqueous Suspensions via Hydrogen Reduction. *J. Phys. Chem. B* **2004**, *108* (37), 13948-13956.
3. Anker, J. N.; Hall, W. P.; Lyandres, O.; Shah, N. C.; Zhao, J.; Van Duyne, R. P., Biosensing with plasmonic nanosensors. *Nat. Mater.* **2008**, *7* (6), 442-453.
4. Evanoff, D. D., Jr.; Chumanov, G., Synthesis and optical properties of silver nanoparticles and arrays. *ChemPhysChem* **2005**, *6* (7), 1221-1231.
5. Otto, M.; Dimitris, C.; Natalia Del, F.; Fabrice, V., Optical response of a single noble metal nanoparticle. *Journal of Optics A: Pure and Applied Optics* **2006**, *8* (4), S264.
6. Kelly, K. L.; Coronado, E.; Zhao, L. L.; Schatz, G. C., The Optical Properties of Metal Nanoparticles: The Influence of Size, Shape, and Dielectric Environment. *J. Phys. Chem. B* **2003**, *107* (3), 668-677.
7. Kelly, K. L.; Lazarides, A. A.; Schatz, G. C., Computational Electromagnetics of Metal Nanoparticles and Their Aggregates. *Computing in Science and Engg.* **2001**, *3* (4), 67-73.
8. Cottancin, E.; Broyer, M.; Lerme, J.; Pellarin, M. In *Optical properties of metal clusters and nanoparticles*, CRC Press: 2011; pp 24/1-24/25.

9. (a) Kinnan, M. K.; Kachan, S.; Simmons, C. K.; Chumanov, G., Plasmon Coupling in Two-dimensional Arrays of Silver Nanoparticles: I. Effect of the Dielectric Medium. *J. Phys. Chem. C* **2009**, *113* (17), 7079-7084; (b) Kinnan, M. K.; Chumanov, G., Plasmon Coupling in Two-dimensional Arrays of Silver Nanoparticles: II. Effect of the Particle Size and Interparticle Distance. *J. Phys. Chem. C* **2010**, *114* (16), 7496-7501.
10. Kreibig, U.; Vollmer, M., *Optical properties of metal clusters*. Springer: Berlin; New York, 1995.
11. Evanoff, D. D.; White, R. L.; Chumanov, G., Measuring the Distance Dependence of the Local Electromagnetic Field from Silver Nanoparticles. *The Journal of Physical Chemistry B* **2004**, *108* (5), 1522-1524.
12. (a) Haes, A. J.; Van Duyne, R. P., A Nanoscale Optical Biosensor: Sensitivity and Selectivity of an Approach Based on the Localized Surface Plasmon Resonance Spectroscopy of Triangular Silver Nanoparticles. *Journal of the American Chemical Society* **2002**, *124* (35), 10596-10604; (b) Malynych, S.; Chumanov, G., Light-induced Coherent Interactions between Silver Nanoparticles in Two-dimensional Arrays. *J. Am. Chem. Soc.* **2003**, *125* (10), 2896-2398; (c) Jensen, T. R.; Duval, M. L.; Kelly, K. L.; Lazarides, A. A.; Schatz, G. C.; Van Duyne, R. P., Nanosphere Lithography: Effect of the External Dielectric Medium on the Surface Plasmon Resonance Spectrum of a Periodic Array of Silver Nanoparticles. *J. Phys. Chem. B* **1999**, *103* (45), 9846-9853.

13. Andersen, P. C.; Rowlen, K. L., Brilliant Optical Properties of Nanometric Noble Metal Spheres, Rods, and Aperture Arrays. *Applied Spectroscopy* **2002**, 56 (5), 124A-135A.
14. Zou, S. L.; Janel, N.; Schatz, G. C., Silver nanoparticle array structures that produce remarkably narrow plasmon lineshapes. *Journal of Chemical Physics* **2004**, 120 (23), 10871-10875.

CHAPTER TWO

ONE-STEP SYNTHESIS AND INVESTIGATION OF HIGHLY CONCENTRATED SILVER NANOPARTICLES WITH AN ULTRA-THIN SILICA SHELL

2.1 Introduction

Metallic nanoparticles, and in particular silver nanoparticles (AgNPs), have attracted significant interest in a large variety of applications¹ including catalysis², optics³, sensing⁴ and therapeutics⁵. As a result, a large spectrum of synthetic methods have emerged, resulting in colloidal AgNPs with a variety of morphologies.⁶ These synthetic methods, that generally involve the reduction of silver salts in the presence of capping or stabilizing agents for the control of particle size and stability, typically give low AgNP concentrations (less than 1 mM)⁷ and therefore are not suitable for large-scale production. Few examples exist in literature of higher concentrations being achieved, all of which require the addition of stabilizing ligands and generally use organic solvents.⁸

Ultra-thin silica shells (UTSS) are an effective way to improve the stability and compatibility of metallic nanoparticles without significantly attenuating their optical properties. This is of particular importance to plasmonic particles used in sensing applications such as localized surface plasmon resonance (LSPR) or surface enhanced Raman spectroscopy (SERS).⁹ For AgNPs an UTSS can hinder the oxidation of Ag in both air and water and provide a scaffold for functionalization through well-established silane chemistry. In addition, the silica shell inhibits the

dissolution of silver that produces potentially harmful silver ions in bio-applications. Therefore the development of a simple and reliable method to produce AgNPs with an UTSS will improve upon numerous already existing applications as well as stimulate new applications, specifically in the area of optical labeling and plasmonics.

The vast majority of methods for producing silica layers around metallic nanoparticles are derived from the Stöber¹⁰ method that uses alkoxysilanes, most commonly tetraethyl orthosilicate (TEOS), as SiO₂ precursors. Condensation and nucleation reactions form a silica shell around the metallic core under the catalytic action of ammonia causing the hydrolysis of alkoxysilanes.¹¹ Another less common approach introduced by Mulvaney *et al.*, demonstrated that gold and silver nanoparticles could be made vitreophilic using a silane coupling agent such as (3-aminopropyl)-trimethoxysilane (APTMS), which generates a monolayer on the surface of the particles. The layer can be further grown by the addition of sodium silicate and controlled precipitation by the addition of ethanol.¹² One of the issues with using sodium silicate as a precursor is that it results in suspensions with high ionic strength thereby leading to particle aggregation.¹³ Using common methods to produce silver nanoparticles described by Lee and Meisel¹⁴ only add to the ionic strength. Aggregation increases with the particle concentration making high ionic strength unacceptable when a high concentration of nanoparticles in solution is required. Haran and Zohar were able to avoid excess of sodium ions by using AgNPs synthesized by the hydrogen reduction method developed in this

laboratory.¹⁵ In a multistep process, these particles were then coated with APTMS followed by silica deposition using sodium silicate and ethanol.¹⁶

Here, we report a one-step method for synthesizing 40-400 nm AgNPs with an UTSS. This method allows for the production of fairly monodisperse spherical silver nanoparticles in concentrations, for example, up to 4.8×10^{13} AgNP (0.3% of Ag by weight) per litre for 100 nm AgNP with 1 nm silica shell. The shell can be made between <1 nm to 5 nm depending on initial silica concentration and reaction time. This silica shell greatly improves the particle stability allowing for further concentration of the particles in water to 43% Ag by weight. The AgNPs exhibited shelf stability of >3 years in typical laboratory conditions under ambient light. To the best of our knowledge this is the first example of silica coated AgNPs synthesized in a one-step reaction resulting in highly concentrated, stable AgNPs without a stabilizing ligand. In addition, care is taken to have a more complete understanding of the mechanism behind the reaction in addition to identification of the 353 & 384 nm peaks present in the UV-Vis spectra. Because of the nanoparticles exceptional stability and the ability to achieve very high particle concentrations, it is also expected that the described method will find commercial importance. It is important to note that when high optical densities (>3) are reported it is merely the dilution factor since it will likely not be the true optical density of highly concentrated AgNPs due to multiple scattering. So an optical density of 2,500 means it was diluted 2,500 times yielding an optical density of 1 in the UV-Vis spectra.

2.2 **Materials and Methods**

2.2.1 *Materials.*

Deionized water with a nominal resistivity of 18 M Ω ·cm was obtained from a Millipore Milli-Q water purification system. Silver(I) oxide (99.99%) and anhydrous sodium sulfate (99.99%) were acquired from Alfa Aesar. Poly(4-vinylpyridine) (PVP) and ACS grade sodium sulfide nonahydrate were purchased from Sigma-Aldrich. USP grade absolute 200 proof ethanol was obtained from Aaper Alcohol & Chemical Company. Sodium metasilicate (SiO₂ 44-47%) and fumed silica (99.8%) were purchased from Sigma-Aldrich and purified by heating at 500 °C for 5 hours under vacuum. Ultra-high-purity hydrogen and ultra-high-purity nitrogen were purchased from Air Gas. Indium tin oxide (ITO) glass (8-12 Ω /sq inch) was received from Sigma and Delta Technologies, LTD. Unless specified, all reagents and solvents were used as received.

2.2.2 *Instrumentation*

UV-vis spectra were recorded using a Shimadzu UV-2501 PC spectrometer. Scanning electron microscopy (SEM) images were taken using a Hitachi SEM-4800 and high resolution transmission electron microscopy (TEM) images were obtained with a Hitachi TEM-H9500. Slides for SEM imaging were prepared by roll coating ITO slides in a 0.25% PVP in ethanol solution for 4 hours followed by roll coating in AgNP solutions with 1 mM sodium sulfate to increase packing density for 12 hours.

2.2.3 *Synthesis of AgNPs with UTSS*

AgNPs with UTSS synthesis was derived from the hydrogen reduction method, previously developed in this lab.¹⁵ Sodium metasilicate or fumed silica was added to 250 mL of DI water in a 500 mL quartz round-bottom flask to obtain concentrations between 0.1 to 6 mM and then sonicated for 30 seconds to disperse. Following this, 0.25 to 2 grams of silver(I) oxide was added to the solution and hand shaken for 1 minute. The flask was then connected to a condenser and hydrogen line followed by heating to 73 °C with stirring under ambient conditions. Once the temperature has stabilized, the vessel was flushed with hydrogen and pressurized to 10 psi hydrogen to initiate the reaction. Typical reactions would range between 3-20 hours depending on the desired thickness of shell, concentration and size of the particles. AgNPs were washed to remove excess silica using DI water saturated with silver(I) oxide for particle stability and could be further concentrated by centrifugation.

2.2.4 *Preparation of 2D Arrays*

Standard microscope slides were cut into 11 mm x 25 mm sized pieces and cleaned by sonication in water for 15 minutes followed by drying with nitrogen gas and plasma treating for 10 minutes. After cleaning, the slides were placed into a 0.1% PVP solution and rotated for 4 hours. Following PVP exposure, ethanol and water rinses were performed after which the slides were dried with nitrogen gas and annealed at 120 °C for 3 hours. Next, slides were quickly cooled with a stream of nitrogen gas and rolled overnight in aqueous suspensions of AgNPs with an optical density (O.D.) of 3 containing 1.5 mM sodium sulfate.

2.2.5 *Post-Synthesis Shell Growth and Stability Study*

AgNP obtained using the above method with an ~1 nm silica shell were diluted from an optical density of 27.31 with varying concentrations of sodium silicate in water to achieve a solution with an optical density of 2 and a concentration of sodium silicate between 0-2 mM. To promote condensation of the silica onto the particle surface, 1 mL of each solution was pipetted into 3 mL of ethanol. UV-Vis was taken revealing a red shift of the dipole that increased for increasing silica concentration. UV-Vis spectra was taken before and after each step. To test the permeability of the silica shell the particles were exposed to 3 mM sodium sulfide and UV-Vis was taken in regular intervals to monitor the plasmon resonance.

2.3 **Results and Discussion**

It was originally observed that the glass surface of the reaction vessel plays a major role in the AgNP synthesis during the reaction of hydrogen gas with silver oxide.¹⁵ A mechanism was implicated suggesting a possible catalytic role of a glass surface on the formation of initial silver seed on the surface followed by their release and further growth in the solution. This was further corroborated by comparing reaction results obtained in Pyrex[®], quartz, and fluorinated-silane coated vessels.¹⁵ A typical growth in a Pyrex[®] vessel results in mostly spherical AgNPs with an optical density (O.D.) of ~1.5 for 100 nm AgNPs. When the reaction was performed under the same conditions in a high-purity quartz vessel the obtained O.D. was at least an order of magnitude lower, though the particle size and shape distribution was similar to those in the Pyrex[®] vessel. Using a Pyrex[®]

vessel coated with a cross-linked fluorosilane, a particle O.D. of ~ 0.4 was obtained under the same conditions and the particles were primarily square platelets.¹⁵ After growing AgNPs in uncoated Pyrex[®], the interior glass walls were covered with AgNPs forming a dense mirror film. Quartz and fluorinated vessels produced some coloration due to AgNP formation on the surface, however the films were not nearly as dense compared to the Pyrex[®] surface. These initial observations prompted more detailed studies with the goal of further understanding the role of the glass surface (silica) during the hydrogen reduction of silver oxide and ultimately developing an efficient, fully controlled method for synthesis of high quality stable AgNPs.

A Teflon[®] reactor was used to eliminate the effect of glass walls on the reduction reaction. Neither silver(I) oxide nor soluble silver salts could be reduced to significant extent by hydrogen gas (**Figure 2.1A**). This was a somewhat surprising result considering the fact that the standard redox potential of silver is highly positive (0.79 V) against SHE. Even though further studies are required to fully understand this behavior, the available literature mentions the formation of silver hydride as a preferred reaction instead of the reduction to silver metal.¹⁷ The addition of silica species, either in the form of fumed silica or sodium silicate, to the Teflon[®] reactor containing 10 mM of Ag₂SO₄ and hydrogen gas at 70 °C effectively produced a nanoparticle suspension with O.D. 13 (**Figure 2.1C**). The results point to silica species catalyzing the reduction of silver and formation of AgNPs. The reaction without silica produced particles with O.D. ~ 0.08 , most likely due to uncontrolled impurities capable of catalyzing the reduction. The addition of sodium

silicate without hydrogen resulted in the formation of insoluble silver silica, as evident from UV-Vis spectra, **Figure 2.1B**. In the case of a Pyrex[®] reaction vessel, a small amount of silica dissolved from the walls forms silver silicate that then is reduced to silver metal by hydrogen gas. The pH value of saturated silver oxide in water at 73 °C is ~10 which will facilitate the solubility of the glass surface, producing more silica species into the solution and is what likely produces the AgNPs seen without additional silica in the original reaction.¹⁸

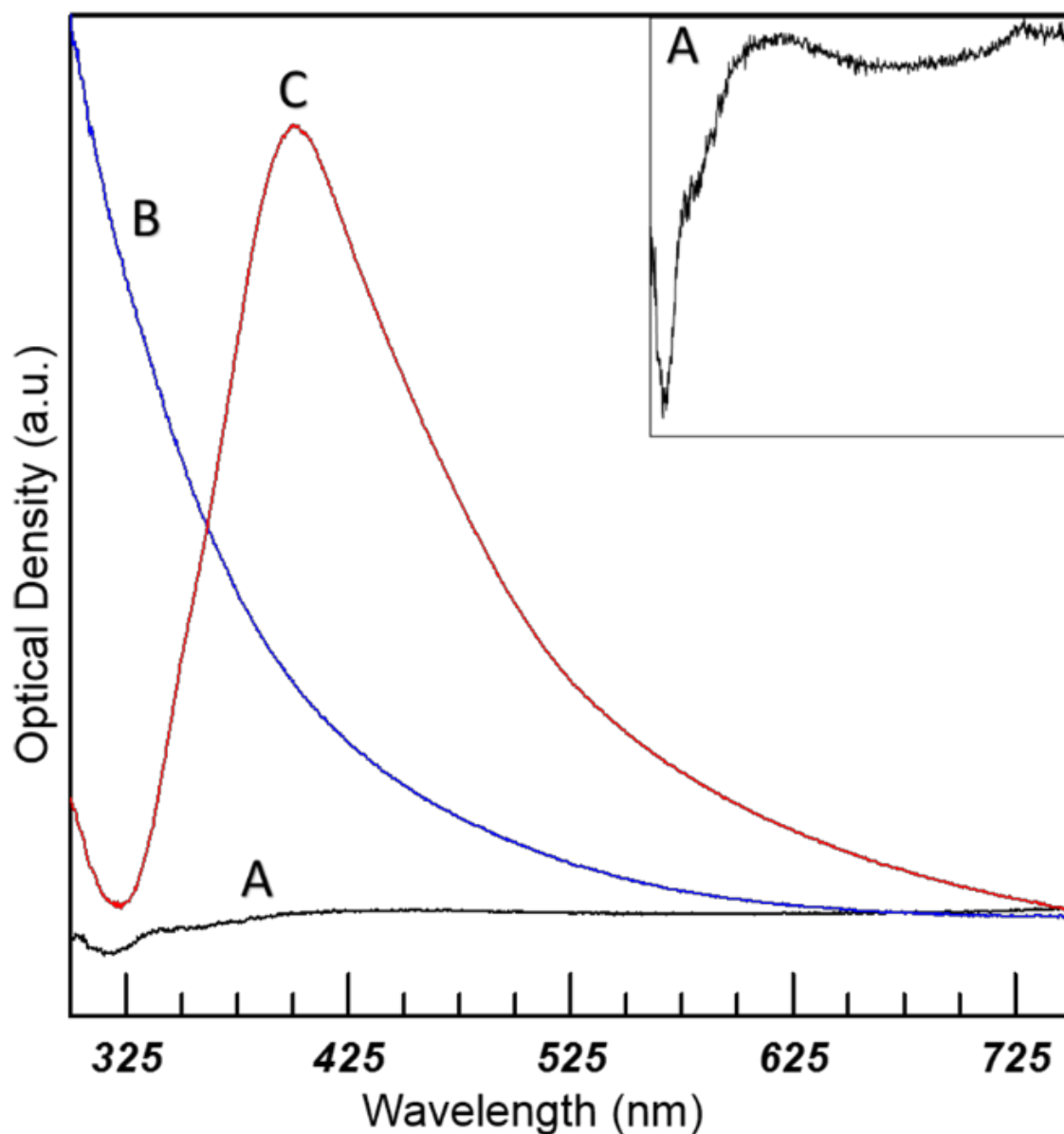


Figure 2.1 UV-Vis spectra of (A) 10 mM Ag_2SO_4 under H_2 for 2 hours (B) following addition of 3 mM Na_2SiO_3 (C) after reaction placed back under H_2 for 1 hour (10x dilution). All steps were performed in a Teflon[®] reactor.

To build upon the observation that silica species catalyze the reduction of silver seeds and particle growth, both fumed silica and sodium silicate in concentrations between 0.1 and 6 mM were studied. A quartz vessel was used so that the contribution from the dissolution of glass walls would be minimized,

because pure quartz has a significantly lower solubility than Pyrex[®].¹⁹ It was immediately evident that the addition of the silica species greatly increased the concentration of resulting particles. Optical density 10-100x greater than that achieved in a typical Pyrex[®] vessel was obtained, with the final concentration being largely dependent on the reaction time and concentration of silica species.

Approximately 5% of the AgNPs synthesized in a Pyrex[®] vessel without the addition of silica are in the form of long rods and flat platelets. This result can be attributed to a low concentration of silica that was dissolved from the walls of the Pyrex[®] vessel. The silica species in water are highly hydrated and form hydrogel particles of various shapes and sizes. A number of small hydrogel particles are expected in solutions with low concentrations of silica, such as those expected from the dissolution of Pyrex[®]. A small hydrogel particle can form only one silver seed; if more than one small seed is initially formed, the seeds will coalesce into a bigger seed because not enough silica is available for the stabilization of several seeds. To the contrary, several seeds can be stabilized by the silica matrix in larger hydrogel particles. Once a single seed starts to grow in a small hydrogel particle, it will push the silica to one side resulting in an asymmetric silica/silver cluster because there is not enough silica to form a uniform silica shell. Assuming that silica catalyzes the reduction of silver, the silver growth will occur at the silica/silver interface and proceed in one direction, resulting in the formation of silver rods. The formation of silver platelets can be similarly explained by the presence of slightly larger hydrogel particles capable of catalyzing the growth of AgNPs in two dimensions. For even larger silica hydrogel particles, the growth proceeds in three

dimensions resulting in polyhedral shaped AgNPs. A similar seed-mediated approach to growing rods has also been described in the literature to synthesize silver nanorods using 16 nm Pd decahedra seeds as a cap on one side.²⁰

Only polyhedral AgNPs were observed when sodium silicate or fumed silica was added to the reaction. In this case, the concentration of silica was sufficient to form only large hydrogel particles. There was enough silica to completely encapsulate the seeds and, because the silver reduction takes place at the silver/silica interface, the seeds grow more or less in three dimensions resulting in the polyhedral shape with a thin silica shell. The silica matrix serves a dual purpose; a capping agent encapsulating the AgNPs and a catalyst for the silver reduction. Common methods to produce nanoparticles incorporate capping agents such as surfactants, polymers and ligands that typically result in spherical particles.²¹ In addition, these AgNPs are very uniform in size, data in **Figure 2.2** shows size distribution of 50 different AgNPs for a system grown with 0.8 mM fumed silica giving a distribution of 114.53 ± 3.75 nm.

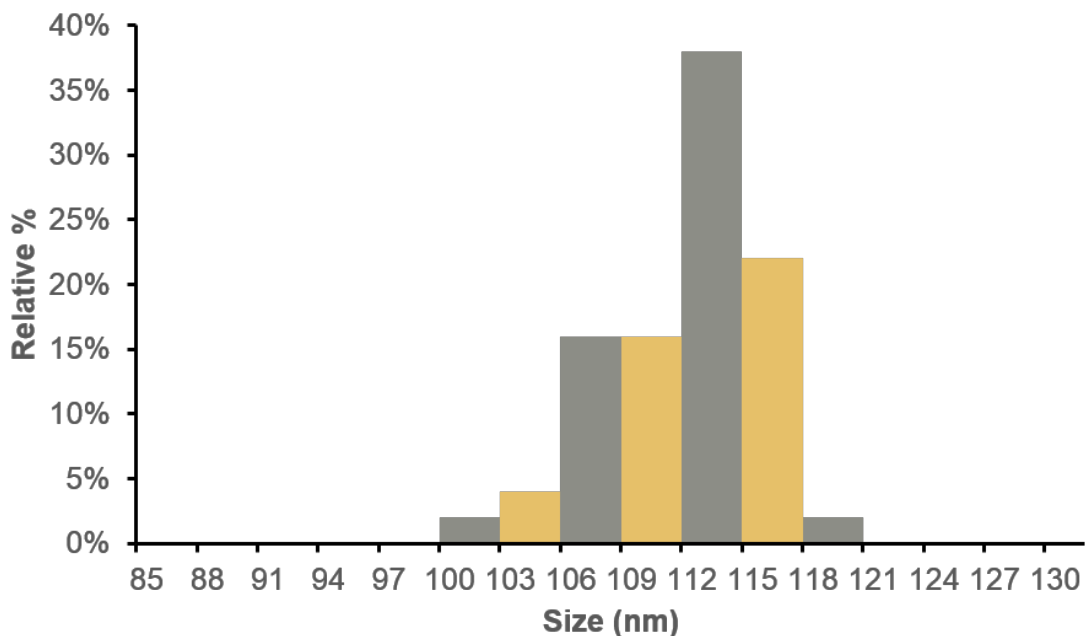


Figure 2.2 Size distribution analysis of 50 AgNPs giving a size distribution of 114.53 ± 3.75 nm to demonstrate the monodispersity of the AgNPs obtained via this method.

As can be seen in **Figure 2.3**, AgNPs grown with the addition of silica were monodispersed and homogeneous as compared to those grown in a Pyrex[®] vessel where a significant size and shape polydispersity can be seen. While the rods and platelets produced in Pyrex[®] can be largely removed by filtration, this additional step can cause particle aggregation. The use of silica in the reaction provides an opportunity to grow monodispersed AgNPs in high concentrations.

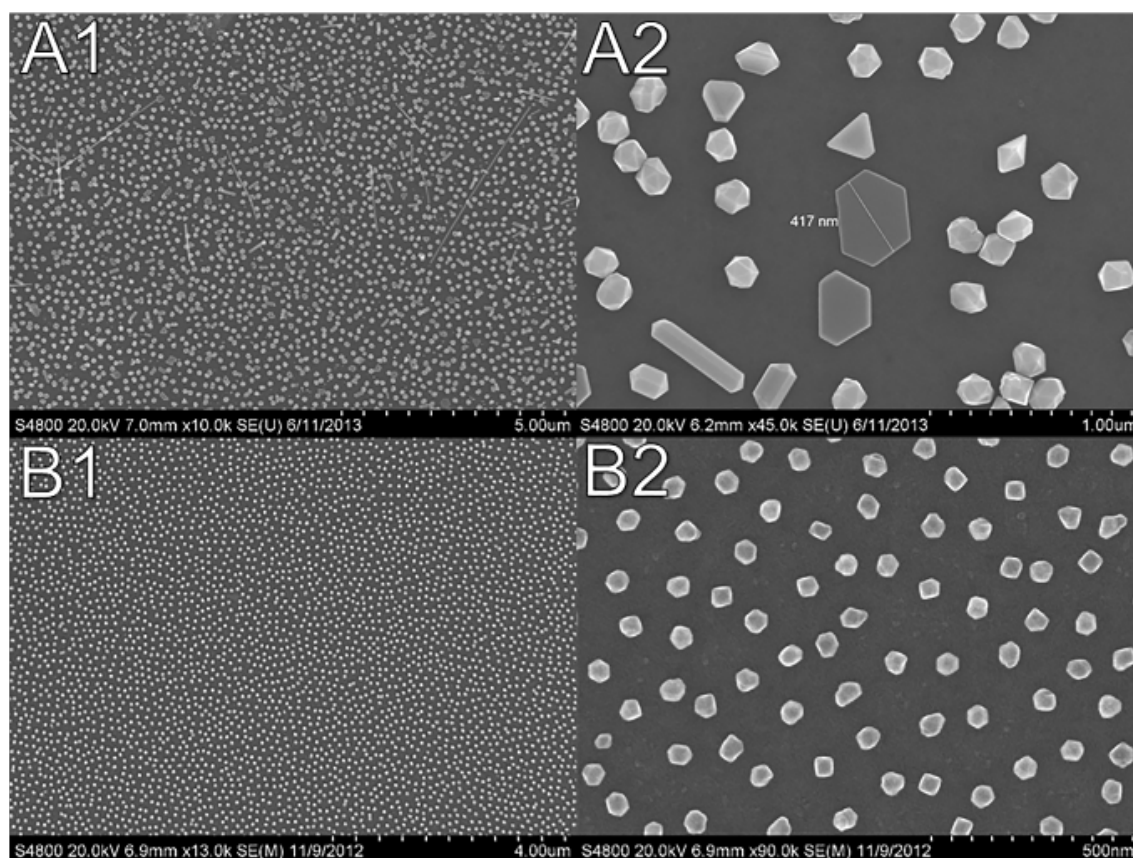


Figure 2.3 SEM images of AgNPs grown to 100 nm in Pyrex® (A) and AgNPs grown to 100 nm in quartz with the addition of 1 mM fumed silica (B)

In addition to the study of the effect of silica on the reaction, the presence of shoulder peaks at 353 & 380 nm were investigated. The 380 nm peak results from the polyhedron nature of the AgNPs and is not present for AgNP spheres of the same size.²² By etching the edges of our AgNPs we were able to also show this experimentally. AgNPs were grown to 100 nm in size and a fraction of this was spun down twice using ultra-pure water. This causes a dissolution of the AgNPs with the edges essentially rounding due to their high surface area relative to the rest of the nanoparticle. **Figure 2.4** shows AgNPs before (blue) and after (black) the dissolution. The AgNPs become more spherical in nature, this is seen in both

the SEM image as well as by the disappearance of the 380 nm shoulder in the accompanying UV-Vis spectra.

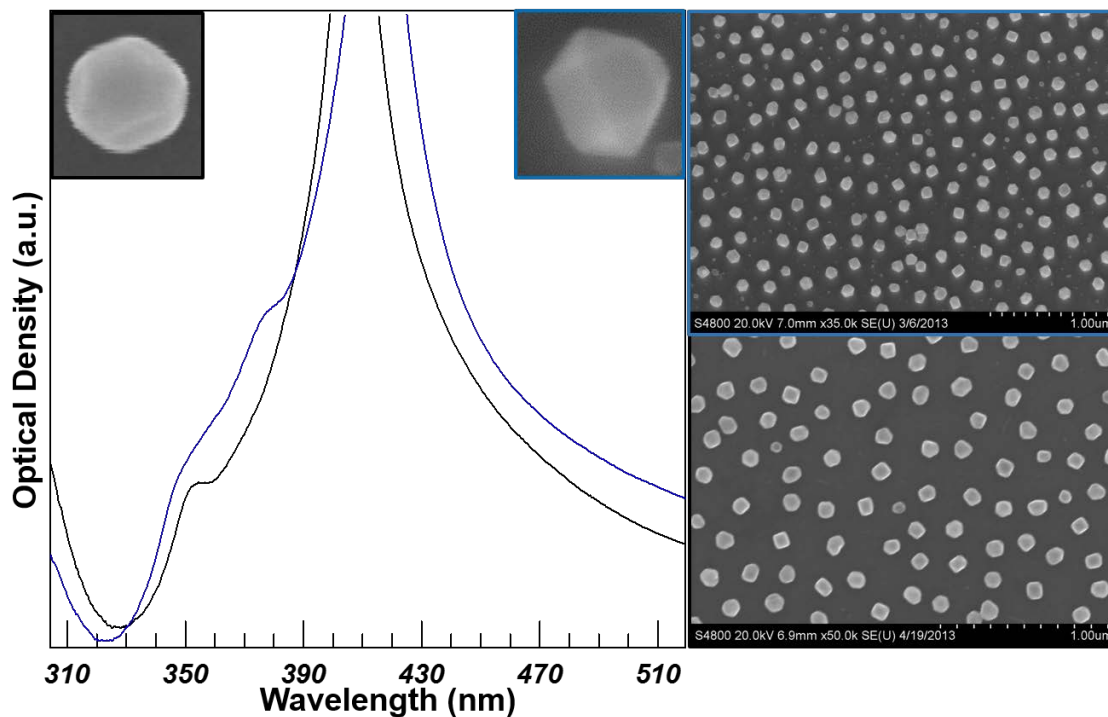


Figure 2.4 UV-Vis of polyhedron (blue) and spherical (black) AgNPs with accompanying SEM images.

The peak present at 353 nm results from silver(I) oxide on the nanoparticle surface. This was determined by exposing the rounded AgNPs seen in the above figure to silver(I) oxide and assembling into 2D arrays. The resulting UV-Vis spectrum was taken showing a peak at 353 nm. These arrays were then exposed to silver(I) oxide saturated water (A) or ultra-pure water (B) for a period of 3 days. In **Figure 2.5** we can see the 353 nm peak stay steady for the array exposed to silver(I) oxide while it decays for the slide exposed to ultra-pure water in which it is expected that the silver(I) oxide will dissolve into the surrounding water and no longer be on the AgNP surface.

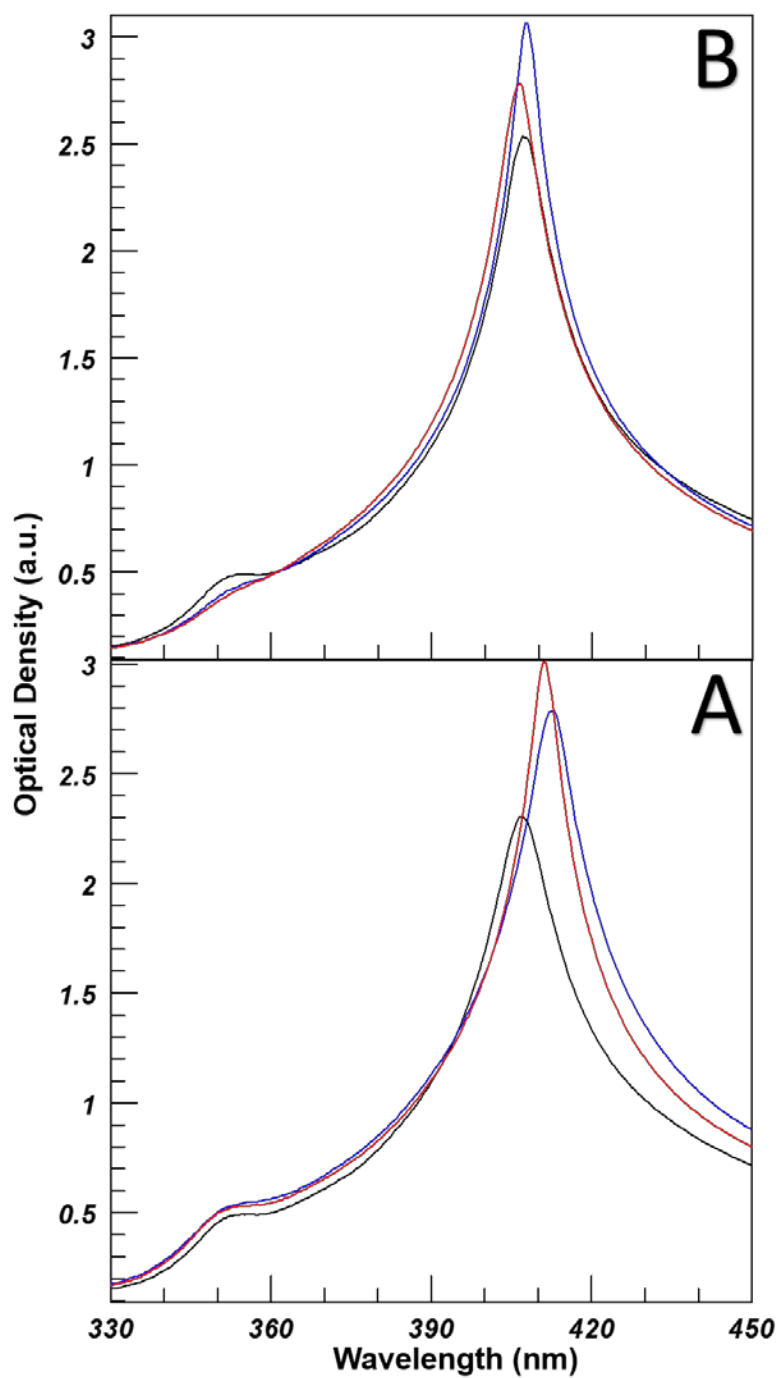


Figure 2.5 UV-Vis of 2D array of AgNPs exposed to saturated silver(I) oxide water (A) and ultra-pure water (B) showing the degradation of the 353 nm peak. Spectra taken immediately (black), 1 day (blue) and 3 days (red) later.

Based on the model that silica species catalyze the reduction of silver and growth of AgNPs, it was assumed that a very thin silica shell may exist on the particles even when grown without the addition of silica. To investigate this assumption, AgNPs were grown in a Pyrex® vessel without adding silica to the size of 100 nm and high resolution TEM was undertaken. Indeed, as can be seen in **Figure 2.6**, a very thin, ~1.1 nm shell was present around the particles. As is discussed later, the addition of silica allows further controlling of the shell thickness. This silica shell establishes the stability of AgNPs in aqueous suspensions.

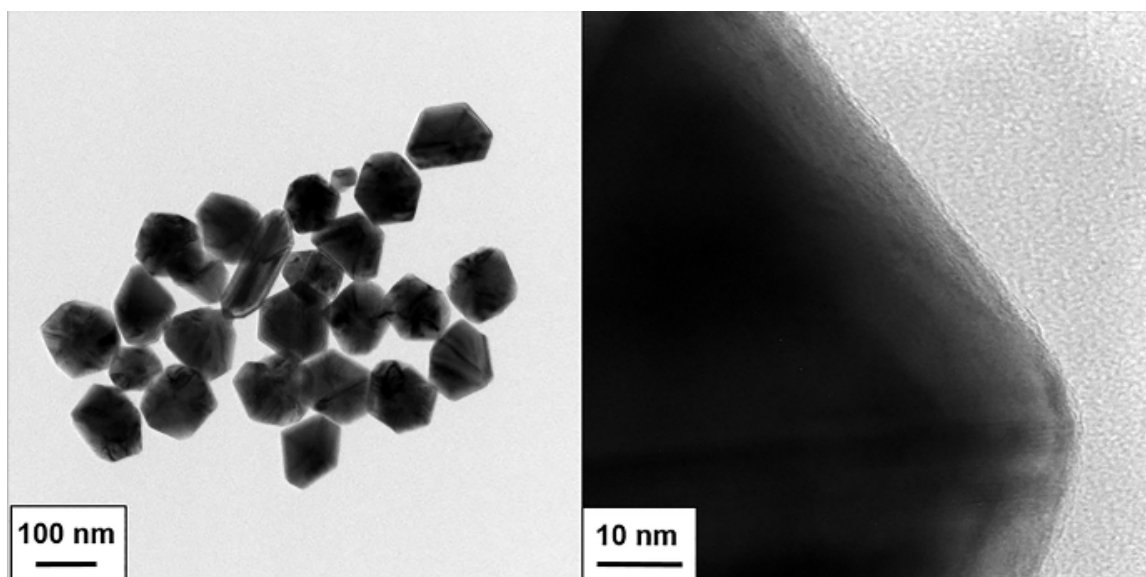


Figure 2.6 HR-TEM images of AgNPs grown to 100 nm in Pyrex® without additional silica show a ~1.1 nm silica shell.

Sodium silicate and fumed silica were added to a quartz reaction vessel in concentrations ranging from 0.1 to 6 mM to determine the effect of different silica species on the growth of the AgNPs. Both species behaved similarly in that increasing the silica concentration resulted in increased concentration of AgNPs and a longer reaction time required to reach a desired particle size. However, it is

easier to control the sodium silicate concentration as compared to fumed silica, which is difficult to measure and uniformly disperse in solution. Despite this, fumed silica would be advantageous if sodium is of concern for final applications.

To demonstrate the similarities, separate reactions were carried out with 0.8 mM sodium silicate and 1 mM fumed silica to study the AgNPs growth over time. It was previously observed that these concentrations produced the same ~1-2 nm silica shell on 100 nm AgNPs. As the reactions proceeded, aliquots were taken at 30 minute intervals starting at 5 minutes after the beginning of the reaction. The samples were washed 3 times using saturated silver(I) oxide water to remove excess of silica prior to imaging. It was previously determined that washing with saturated silver(I) oxide aqueous solution eliminated the particle aggregation during the centrifugation step contrary to when washing with deionized water alone. As can be seen in **Figure 2.7**, it appears that the shell thickness decreased as the particles grow larger; e.g. an initial shell of ~5 nm on 50 nm particles decreased to ~1 nm as the particles approached 100 nm. As the AgNPs size and their surface area increases the shell thickness decreases because the same amount of silica is available for covering a larger surface area.

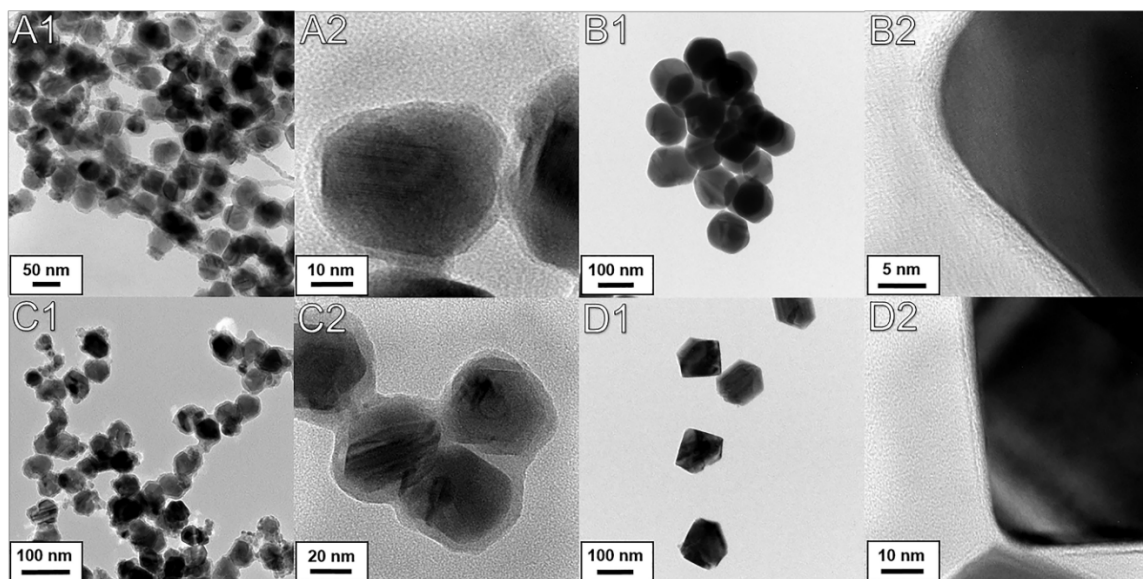


Figure 2.7 TEM of AgNPs grown with 0.8 mM Na_2SiO_3 taken at 30 minutes (A) and 4 hours (B) & AgNPs grown with 1 mM fumed silica taken at 30 minutes (C) and 4 hours (D).

The shell thickness is tied to the particle size and not the concentration of initial silica species which only results in a higher AgNP concentration. To demonstrate this behavior, 50 nm AgNP were grown in two separate reactions using 0.8 mM and 6 mM sodium silicate. The shell thickness was ~5 nm for both reactions, however it took 30 minutes to achieve 50 nm AgNPs with a final O.D. of 2.7 using 0.8 mM sodium silicate. When the concentration of sodium silicate was increases to 6 mM it took 5 hours to achieve the same size AgNPs with O.D. of 84 (**Figure 2.8**). It was concluded that increasing silica concentration results in a larger number of seeds; however since the reaction kinetics are limited by the dissolution of silver(I) oxide (approximately 50 mg/L at 73 °C) the time to achieve the same size particles was greatly increased with increasing the silica concentration.

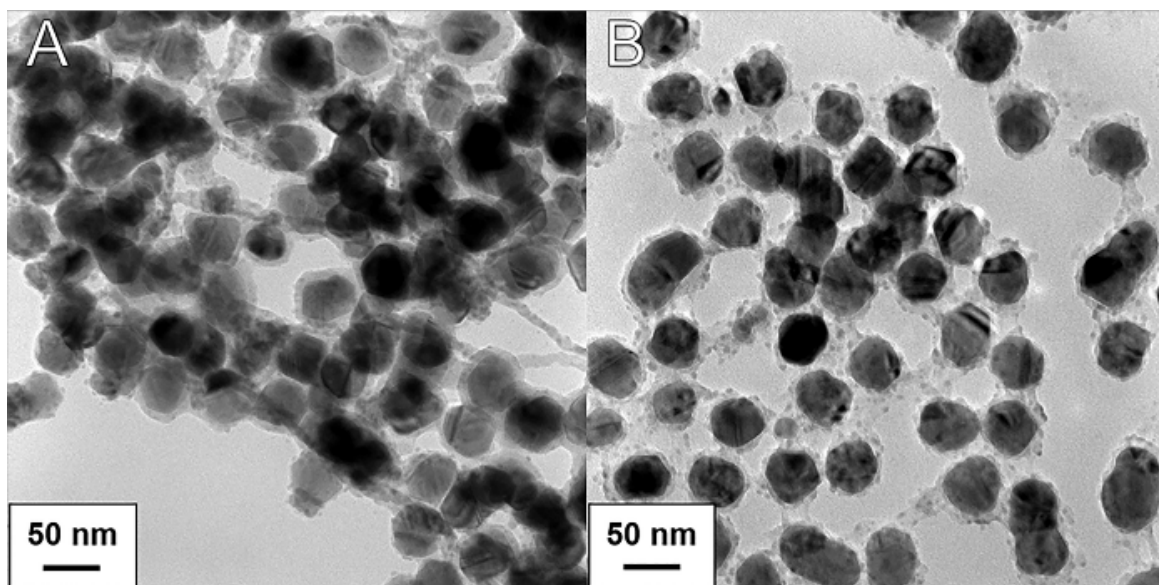


Figure 2.8 TEM images of AgNPs grown to ~50 nm AgNP with 0.8 mM (A) and 6 mM (B) of sodium silicate added. (A) with an O.D. of 2.7 was obtained after 30 minutes while (B) an O.D. of 84 required 5 hours.

The addition of silica species to the reaction also allows the synthesis of very large AgNPs. As depicted in **Figure 2.9**, particles were grown to ~250 nm and ~400 nm with the addition of 1.27 mM and 0.5 mM fumed silica, respectively. The final O.D. for the ~250 nm AgNPs was 48 while the ~400 nm AgNPs achieved an O.D. of 36. The silica shell thickness was less than 1 nm in both cases.

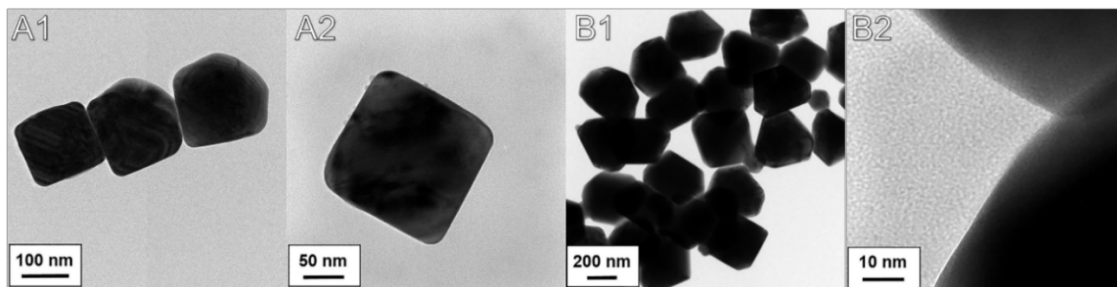


Figure 2.9 HR-TEM images of AgNPs grown to ~250 nm (A) and ~400 nm (B) with 1.27 & 0.5 mM fumed silica, respectively.

When growing AgNPs with the addition of silica, the silica shell thickness ranged from <1 nm to ~5 nm depending on the initial silica concentration and size of particle desired. If required, this thickness can be further increased. Since the AgNPs already have a layer of silica there is no need to add a silane coupling agent. A suspension of 100 nm AgNPs with 1 nm shell was diluted to O.D. of 3 with a sodium silicate solution of the concentrations varying between 0 and 2 mM. UV-Vis measurements revealed no noticeable change in the plasmon dipole position indicating absence of the shell thickening. Otherwise, a red spectral shift would be expected due to increasing the local dielectric constant by increasing the shell thickness.²³ The suspensions were then added to ethanol in a 1:4 volume ratio^{12b} to precipitate the silica onto the AgNPs and the UV-Vis was taken again. A red shift of the plasmon resonance resulted from the condensation of the additional silica on the particle surface as was further confirmed with TEM (**Figure 2.10**). No formation of free silica particles was seen. The addition of 1 mM and 2 mM of sodium silicate increased the silica shell around AgNPs to ~5 nm and ~15 nm, respectively. This approach allows for complete control of the silica shell thickness.

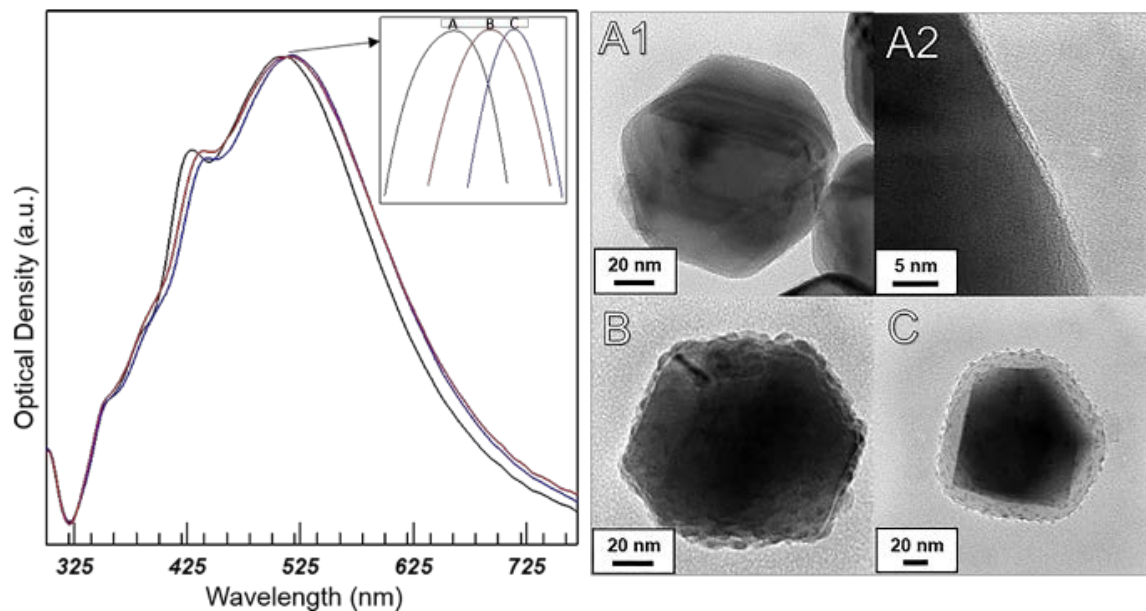


Figure 2.10 UV-Vis and TEM of AgNPs with 1.6 nm Si shell after introduction of 0 mM (A) 1 mM (B) & 2 mM (C) Na_2SiO_3 and addition to EtOH.

Sulfide, due to its high affinity to silver, was used to test the ability of the silica shell to protect the silver surface. Sodium sulfide of 3 mM concentration was added to suspensions containing AgNPs with silica shell of different thicknesses and UV-Vis spectra of the suspensions were taken over the course of 20 hours. As can be seen in **Figure 2.11**, the resonance of the AgNPs with a 1 nm silica shell quickly degraded and was completely lost by the 20 hour mark, at which the spectrum represented that of Ag_2S nanoparticles.²⁴ The trend continued, although at a slower rate, as the shell thickness was increased. The optical density decreased by only 20% for 15 nm silica shell while the shape of the plasmon resonance was retained. This decrease was likely due to the presence of a small fraction of particles with incomplete silica coverage because as this solution was monitored over a period of one month with continuous exposure to the sulfide

solution no further changes were observed. The ~15 nm silica shell completely protected AgNPs from reacting with sulfide.

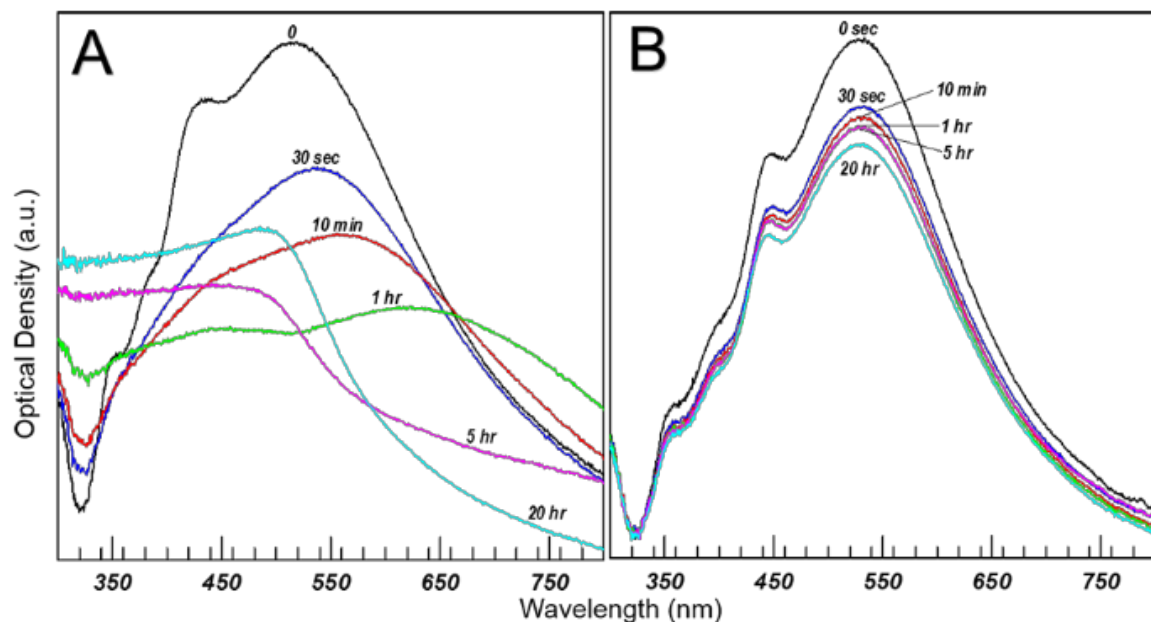


Figure 2.11 UV-Vis of AgNPs with 1 nm Si shell (A) and 15 nm Si shell (B) after exposure to 3 mM Na_2S over a period of 20 hours.

Optical densities of ~100, corresponding to $\sim 4.8 \times 10^{13}$ AgNP per litre (0.3% Ag by weight) can be easily achieved when synthesizing the AgNPs using this method. The particles can be further concentrated because of their excellent stability, imparted by the thin silica shell. For example, 100 nm AgNPs were grown in a 5L quartz vessel with the addition of 1 mM fumed silica and when centrifuged down to ~4 mL, resulted in the final concentration of $\sim 1.98 \times 10^{16}$ AgNP per liter (43% Ag by weight) corresponding to an O.D. of ~11,500. While over time a large fraction of these AgNPs precipitated on the bottom of the container yielding a silver mirror, they were easily re-dispersed via sonication and, in this way, were stable in aqueous media for more than 3 years. The particles have also exhibited

comparable stability when transferred to organic solvents, such as ethanol and 2-propanol.

2.4 Conclusion

A one-step synthesis of highly concentrated silver nanoparticles ranging in size from 40 to 400 nm with an ultra-thin silica shell from <1 nm to 5 nm was developed. It was concluded that silica species catalyze the formation of metal seeds and subsequent growth of silver nanoparticles. The silica shell, which can be further grown by the addition of sodium silicate and ethanol condensation, imparts excellent stability to suspensions with ultra-high nanoparticles concentrations as well as hinders the chemical accessibility of the metal surface. To illustrate their practical importance, these particles are used for self-assembly of a highly sensitive plasmonic sensor, for which the availability of highly concentrated and stable AgNP suspensions was crucial in Chapter 2.²⁵ In addition they are used for SERS and chemiresistor applications in Chapter 3. The method has commercial potential because it is simple, efficient, and capable of producing high concentrations of stable, silica coated silver nanoparticles. The described results also have broader implications because they highlight the importance of considering the potential effects of small concentrations of silica dissolved from glass reaction vessels on the outcome of chemical reactions, especially reactions that are carried out at elevated pH. It is also important to recognize that dissolved silica forms hydrogel particles that can act as centers for condensation and seed formations when synthesizing various nanoparticles in addition to the catalytic effects as was demonstrated here.

2.5 Acknowledgements

This research was supported by the United States Department of Energy, grant No. DE-FG02-06ER46342. We would also like to acknowledge the Clemson University Center for Optical Materials Science and Engineering Technologies.

2.6 References

1. Ahamed, M.; AlSalhi, M. S.; Siddiqui, M. K. J., Silver nanoparticle applications and human health. *Clin. Chim. Acta* **2010**, *411* (23-24), 1841-1848.
2. (a) Sarina, S.; Waclawik, E. R.; Zhu, H., Photocatalysis on supported gold and silver nanoparticles under ultraviolet and visible light irradiation. *Green Chem.* **2013**, *15* (7), 1814-1833; (b) Cuenya, B. R., Synthesis and catalytic properties of metal nanoparticles: size, shape, support, composition, and oxidation state effects. *Thin Solid Films* **2010**, *518* (12), 3127-3150.
3. Evanoff, D. D., Jr.; Chumanov, G., Synthesis and optical properties of silver nanoparticles and arrays. *ChemPhysChem* **2005**, *6* (7), 1221-1231.
4. (a) Langer, J.; Novikov, S. M.; Liz-Marzan, L. M., Sensing using plasmonic nanostructures and nanoparticles. *Nanotechnology* **2015**, *26* (32), 1-28; (b) Haes, A. J.; Van Duyne, R. P., A unified view of propagating and localized surface plasmon resonance biosensors. *Anal. Bioanal. Chem.* **2004**, *379* (7-8), 920-930.
5. Wei, L.; Lu, J.; Xu, H.; Patel, A.; Chen, Z.-S.; Chen, G., Silver nanoparticles: synthesis, properties, and therapeutic applications. *Drug Discovery Today* **2015**, *20* (5), 595-601.

6. Cobley, C. M.; Skrabalak, S. E.; Campbell, D. J.; Xia, Y., Shape-Controlled Synthesis of Silver Nanoparticles for Plasmonic and Sensing Applications. *Plasmonics* **2009**, 4 (2), 171-179.
7. (a) Tolaymat, T. M.; El Badawy, A. M.; Genaidy, A.; Scheckel, K. G.; Luxton, T. P.; Suidan, M., An evidence-based environmental perspective of manufactured silver nanoparticle in syntheses and applications: A systematic review and critical appraisal of peer-reviewed scientific papers. *Science of The Total Environment* **2010**, 408 (5), 999-1006; (b) Oćwieja, M.; Adamczyk, Z.; Morga, M.; Kubiak, K., Silver particle monolayers — Formation, stability, applications. *Advances in Colloid and Interface Science* **2015**, 222, 530-563.
8. (a) Shahzad, A.; Chung, M.; Yu, T.; Kim, W.-S., A Simple and Fast Aqueous-Phase Synthesis of Ultra-Highly Concentrated Silver Nanoparticles and Their Catalytic Properties. *Chem. - Asian J.* **2015**, 10 (11), 2512-2517; (b) Shahzad, A.; Kim, W.-S.; Yu, T., Synthesis, stabilization, growth behavior, and catalytic activity of highly concentrated silver nanoparticles using a multifunctional polymer in an aqueous-phase. *RSC Adv.* **2015**, 5 (36), 28652-28661; (c) Sondi, I.; Goia, D. V.; Matijevic, E., Preparation of highly concentrated stable dispersions of uniform silver nanoparticles. *J. Colloid Interface Sci.* **2003**, 260 (1), 75-81.
9. Shanthil, M.; Thomas, R.; Swathi, R. S.; Thomas, K. G., Ag@SiO₂ Core-Shell Nanostructures: Distance-Dependent Plasmon Coupling and SERS Investigation. *J. Phys. Chem. Lett.* **2012**, 3 (11), 1459-1464.
10. Stoeber, W.; Fink, A.; Bohn, E., Controlled growth of monodisperse silica spheres in the micron size range. *J. Colloid Interface Sci.* **1968**, 26 (1), 62-9.

11. (a) Hardikar, V. V.; Matijevic, E., Coating of nanosize silver particles with silica. *J. Colloid Interface Sci.* **2000**, *221* (1), 133-136; (b) Kobayashi, Y.; Katakami, H.; Mine, E.; Nagao, D.; Konno, M.; Liz-Marzan, L. M., Silica coating of silver nanoparticles using a modified Stober method. *J. Colloid Interface Sci.* **2005**, *283* (2), 392-396; (c) Lismont, M.; Paez, C. A.; Dreesen, L., A one-step short-time synthesis of Ag@SiO₂ core-shell nanoparticles. *J. Colloid Interface Sci.* **2015**, *447*, 40-49.
12. (a) Liz-Marzan, L. M.; Giersig, M.; Mulvaney, P., Synthesis of Nanosized Gold-Silica Core-Shell Particles. *Langmuir* **1996**, *12* (18), 4329-4335; (b) Ung, T.; Liz-Marzan, L. M.; Mulvaney, P., Controlled Method for Silica Coating of Silver Colloids. Influence of Coating on the Rate of Chemical Reactions. *Langmuir* **1998**, *14* (14), 3740-3748.
13. Iler, R. K. Particles coated with dense, hydrated, amorphous silica. US2885366, 1959.
14. Lee, P. C.; Meisel, D., Adsorption and surface-enhanced Raman of dyes on silver and gold sols. *J. Phys. Chem.* **1982**, *86* (17), 3391-5.
15. Evanoff, D. D.; Chumanov, G., Size-controlled Synthesis of Nanoparticles. 1. "Silver-only" Aqueous Suspensions via Hydrogen Reduction. *J. Phys. Chem. B.* **2004**, *108* (37), 13948-13956.
16. Zohar, N.; Haran, G., Modular Plasmonic Antennas Built of Ultrathin Silica-Shell Silver-Core Nanoparticles. *Langmuir* **2014**, *30* (26), 7919-7927.
17. (a) Lu, J.; Aydin, C.; Browning, N. D.; Gates, B. C., Hydrogen Activation and Metal Hydride Formation Trigger Cluster Formation from Supported Iridium

- Complexes. *Journal of the American Chemical Society* **2012**, 134 (11), 5022-5025;
- (b) Tate, B. K.; Nguyen, J. T.; Bacsa, J.; Sadighi, J. P., Heterolysis of Dihydrogen by Silver Alkoxides and Fluorides. *Chemistry – A European Journal* **2015**, 21 (28), 10160-10169; (c) Tate, B. K.; Wyss, C. M.; Bacsa, J.; Kluge, K.; Gelbaum, L.; Sadighi, J. P., A dinuclear silver hydride and an umpolung reaction of CO₂. *Chemical Science* **2013**, 4 (8), 3068-3074.
18. (a) Chêne, J.; Trocellier, P., Investigation of alkali borosilicate glass durability using tritium tracing, β -autoradiography, scanning electron microscopy and ion beam analysis. *Journal of Non-Crystalline Solids* **2004**, 337 (1), 86-96; (b) Rimstidt, J. D., Quartz solubility at low temperatures. *Geochimica et Cosmochimica Acta* **1997**, 61 (13), 2553-2558.
19. Perera, G.; Doremus, R. H.; Lanford, W., Dissolution rates of silicate glasses in water at pH 7. *J. Am. Ceram. Soc.* **1991**, 74 (6), 1269-74.
20. Luo, M.; Huang, H.; Choi, S.-I.; Zhang, C.; Silva, R. R. d.; Peng, H.-C.; Li, Z.-Y.; Liu, J.; He, Z.; Xia, Y., Facile Synthesis of Ag Nanorods with No Plasmon Resonance Peak in the Visible Region by Using Pd Decahedra of 16 nm in Size as Seeds. *ACS Nano* **2015**, 9 (10), 10523-10532.
21. (a) Jana, N. R.; Gearheart, L.; Murphy, C. J., Seed-mediated growth approach for shape-controlled synthesis of spheroidal and rod-like gold nanoparticles using a surfactant template. *Adv. Mater. (Weinheim, Ger.)* **2001**, 13 (18), 1389-1393; (b) Fendler, J. H.; Meldrum, F. C., The colloid chemical approach to nanostructured materials. *Adv. Mater. (Weinheim, Ger.)* **1995**, 7 (7), 607-32; (c) Frens, G., Controlled nucleation for the regulation of the particle size in

- monodisperse gold suspensions. *Nature (London), Phys. Sci.* **1973**, 241 (105), 20-2.
22. Noguez, C., Surface Plasmons on Metal Nanoparticles: The Influence of Shape and Physical Environment. *The Journal of Physical Chemistry C* **2007**, 111 (10), 3806-3819.
23. Evanoff, D. D.; White, R. L.; Chumanov, G., Measuring the Distance Dependence of the Local Electromagnetic Field from Silver Nanoparticles. *The Journal of Physical Chemistry B* **2004**, 108 (5), 1522-1524.
24. Kumari, P.; Chandran, P.; Khan, S. S., Synthesis and characterization of silver sulfide nanoparticles for photocatalytic and antimicrobial applications. *Journal of Photochemistry and Photobiology B: Biology* **2014**, 141, 235-240.
25. Willett, D. R.; Chumanov, G., LSPR Sensor Combining Sharp Resonance and Differential Optical Measurements. *Plasmonics* **2014**, 9 (6), 1391-1396.

CHAPTER THREE

LSPR SENSOR COMBINING SHARP RESONANCE AND DIFFERENTIAL OPTICAL MEASUREMENTS

3.1 Introduction

The need for low-cost biosensors capable of fast, real-time and cost-effective identification of biomarkers has motivated the drive for optical sensors based on surface plasmon resonance (SPR). SPR based sensors utilize thin gold films and exploit the dependence of the resonance frequency on the local dielectric function thereby allowing highly sensitive, label-free measurements.¹ Localized-SPR (LSPR) sensors have emerged as a promising alternative to commercial SPR systems already used in drug-screening platforms and medical diagnostics.² LSPR based sensors are attractive because they exhibit a larger degree of the EM field confinement relative to that of SPR sensors therefore resulting in high sensitivity to events occurring close to the metal surface, while remaining largely insensitive to changes in the bulk solution such as ambient temperature fluctuation. The latter are known to have a detrimental effect in commercial SPR instrumentation.³ This insensitivity to bulk refractive index also gives LSPR instrumentation the potential to be miniaturized while still maintaining high throughput and sensitivity. However, the commercial development of an inexpensive and effective LSPR substrate remains challenging.

The LSPR strongly depends on the shape, size and spacing of the plasmonic nanostructures as well as their local dielectric environment.⁴ The majority of LSPR

substrates are fabricated by top-down approaches involving various lithograph patterning techniques that allow precise control of the size, shape, and periodic arrangement of plasmonic nanostructures.⁵ Conventional lithographic techniques such as focused ion beam and electron beam lithography enable reproducible fabrication of periodic structures, however they can only produce sensing areas up to 1 cm² and require expensive, specialized equipment.⁶ Therefore, template-based techniques such as nanosphere lithography, soft lithography, and colloidal lithography have been used and encompass the majority of the currently developed LSPR substrates due to their relatively low cost, high throughput and commercialization potential.⁷

LSPR substrates prepared by bottom-up approaches typically use chemical techniques for synthesizing metal nanoparticles, often with controlled crystallinity and unique architectures, that are then chemically attached to substrates. These substrates are typically fabricated using bench top chemistry methods in relatively few steps without the need for high vacuum equipment; however they often suffer from significant polydispersity and irreproducibility.

Despite continuing advances in the fabrication of LSPR substrates that are approaching the theoretical limit for figure of merit (FOM) of traditional SPR systems,⁸ little has changed in the way the resonance frequency shift is monitored and measured. LSPR shifts can be measured by recording scattering, reflectance or extinction spectra. For substrates containing high surface density of LSPR structures, extinction measurements are the easiest way to monitor spectral shifts.⁹ A typical LSPR sensor setup consists of a white light excitation source and

a spectrometer to record scattering, reflectance or extinction spectra. This method limits the sensing resolution of the LSPR sensor to the spectral resolution of the spectrometer. It is also possible to measure LSPR shift by monitoring light transmission at a single wavelength as was demonstrated in one of the earliest examples of nanoplasmonic biosensors¹⁰ as well as in a recent work where the LSPR structure was directly fabricated on a photodiode chip.¹¹ In this way, the resolution is not limited by the spectral resolution of a spectrometer but rather by the noise and dynamic range of the detector.

In this paper we describe a simple, sensitive and real time measuring system utilizing a LSPR substrate fabricated using a bottom up approach. This substrate has a FOM that is on par with those achieved for substrates made by more complex top down lithographic techniques. The LSPR substrate is comprised of a 2D array of closely spaced silver nanoparticles (AgNPs) that exhibit a sharp resonance due to coherent plasmon coupling typically providing a typical full width at half maximum (FWHM) of ~15 nm. This sharpness of the resonance presents an opportunity for implementing an efficient differential optical measurement to improve sensitivity and detection limit beyond those typically reported for LSPR substrates with similar FOM. A coupled 2D array of AgNPs is simultaneously irradiated with two closely spaced wavelengths selected in such a way that they probe the resonance on both sides from its maximum. When the resonance shifts to either red or blue side, the extinction at one wavelength increases whereas the extinction at the other wavelength decreases. The sharper the resonance the

larger the differential signal will be for the same shift enabling more sensitive measurements (**Figure 3.1**).

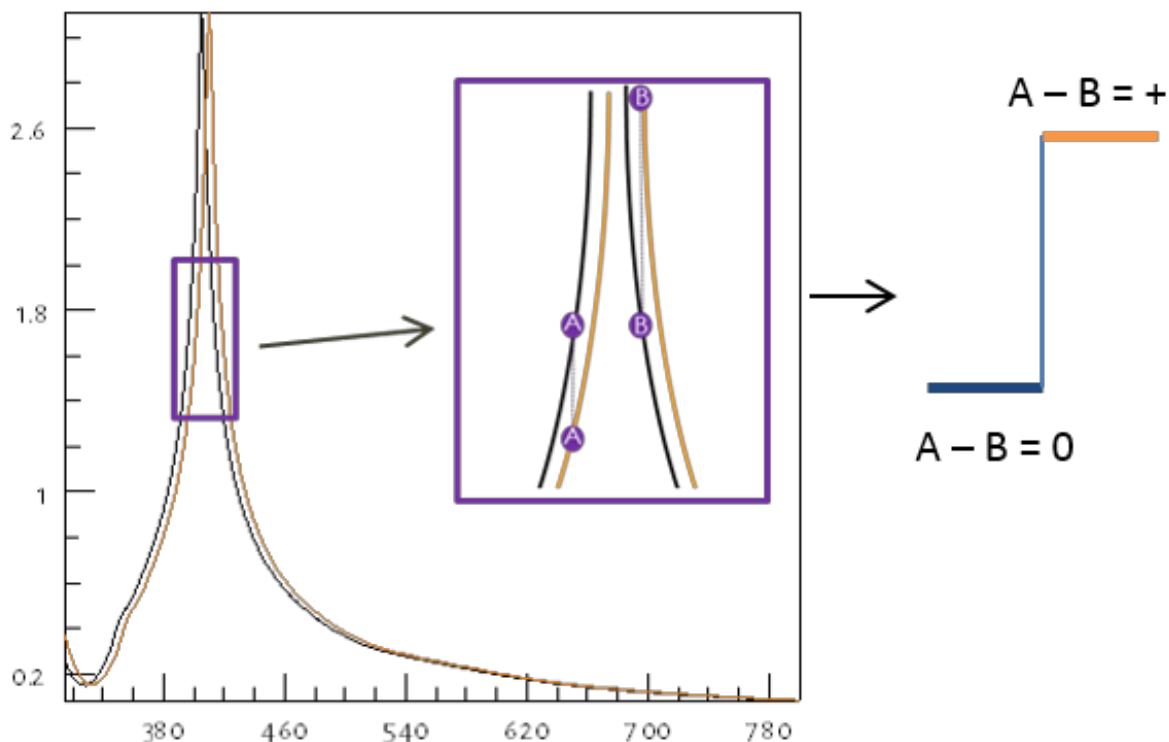


Figure 3.1 Graphic demonstrating the method for differential measurements using the sharp plasmon resonance achieved from 2D arrays of AgNPs.

3.2 Materials and Methods

3.2.1 *Materials*

Poly(4-vinylpyridine) (PVP) was purchased from Sigma Aldrich. ACS grade sucrose and anhydrous sodium sulfate were purchased from Fisher Scientific. Silver(I) oxide (99.99%) and USP absolute-200 proof ethanol were acquired from Alfa Aesar and Aaper Alcohol & Chemical Co., respectively. Fumed silica (99.8%) were purchased from Sigma-Aldrich and purified by heating at 500 °C for 5 hours

under vacuum. Deionized water with a nominal resistivity of 18 M Ω ·cm came from a Millipore Milli-Q water purification system. Ultra-high-purity hydrogen and ultra-high-purity nitrogen were purchased from Air Gas. PVP solutions were prepared by dissolving a weighed quantity in ethanol. Sucrose solutions were prepared by serial dilution from a stock solution prepared by dissolving a weighed quantity in water. Indium tin oxide (ITO) glass (8-12 Ω /sq inch) was received from Sigma and Delta Technologies, LTD. Unless specified, all reagents and solvents were used as received.

3.2.2 Instrumentation

UV-Vis spectra were recorded using a Shimadzu UV-2501PC spectrophotometer. Electron microscopy images were taken with a Hitachi SEM-4800. Home-built LSPR instrumentation consisted of a 150 Watt xenon short arc lamp (Osram), SPEX 500M monochromator equipped with 1800 g/mm grating and a SPEX MSD2 controller. A chopper (SRS) set at 1 kHz was used to modulate the signal. The output slit was replaced with two pinholes permitting the simultaneous selection of two wavelengths separated by 10 nm. The intensity of light was measured by a pair of Hamamatsu R6094 photomultiplier tubes powered by a McPherson 7640 PMT power supply with 2 McPherson 671 pre-amplifiers. Signal was processed by SRS 830 DSP lock-in amplifier (Stanford Research Systems). Data was collected using a program written in LABVIEW 2010. A schematic of the instrument design is shown in **Figure 3.2**, and a picture of the finished design in **Figure 3.3**.

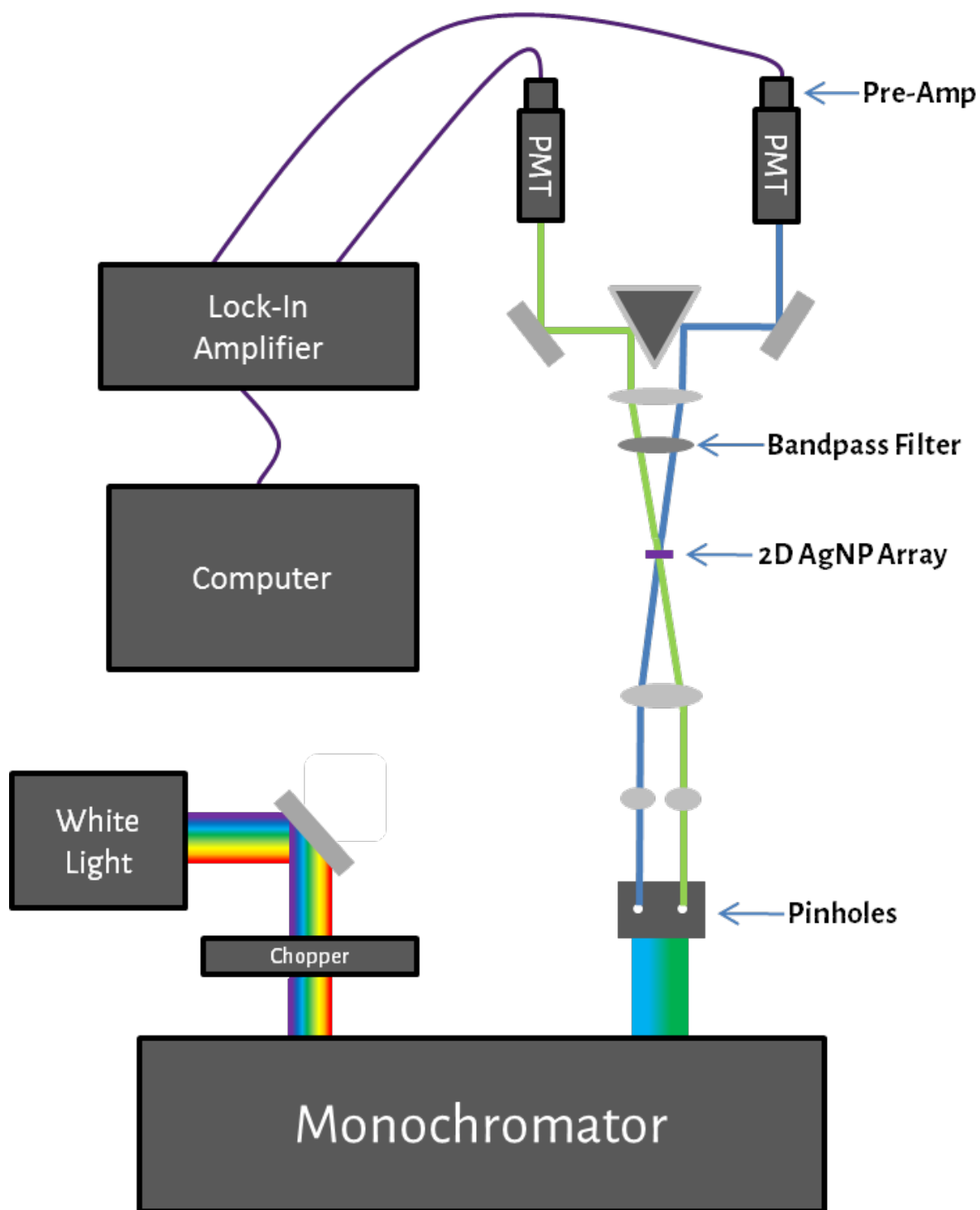


Figure 3.2 Schematic of the differential LSPR instrumentation.

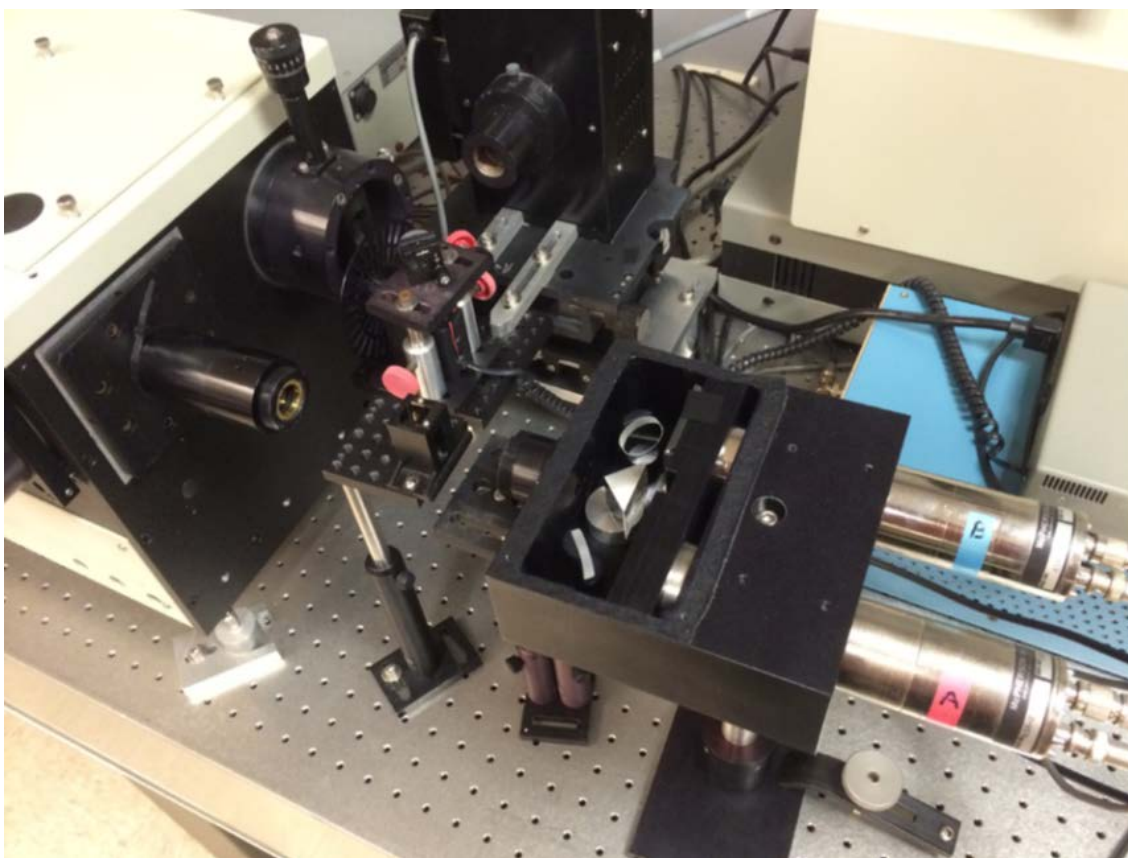


Figure 3.3 Photo of completed differential LSPR instrumentation.

3.2.3 *Synthesis of Silver Nanoparticles*

AgNPs were synthesized using the modified hydrogen reduction method describe in Chapter 2. Briefly, after the addition of silver(I) oxide to deionized water in a round-bottom flask, the synthesis was performed at 73 °C under 10 psi excess pressure of hydrogen gas in the presence of 1 mM fumed silica. All AgNPs used in this study were single crystals with a Feret's diameter of ca. 100 nm with a ~1.6 nm silica shell.

3.2.4 *Fabrication of AgNP Arrays*

Standard microscope slides were cut into 11 mm x 25 mm sized pieces and cleaned by sonication in water for 15 minutes followed by drying with nitrogen gas

and plasma treating for 10 minutes. After cleaning, the slides were placed into a 0.1% PVP solution and rotated for 4 hours. Following PVP exposure, ethanol and water rinses were performed after which the slides were dried with nitrogen gas and annealed at 120 °C for 3 hours. Next, slides were quickly cooled with a stream of nitrogen gas and rolled overnight in aqueous suspensions of ~100 nm AgNPs with an optical density (O.D.) of 3 containing 1.5 mM sodium sulfate. Optimization of sodium sulfate concentration was performed by maintaining AgNP concentration at O.D. 3 and adjusting sodium sulfate concentration to determine which concentration resulted in the strongest coupling. After the nanoparticle adsorption, the slides were rinsed with water and one side of the slide was stripped of AgNPs using a dilute nitric acid solution. The slides were thoroughly rinsed and stored in deionized water. They remained stable for up to 3 month before being used.

3.2.5 Data Collection

UV-Vis spectra of the AgNP arrays in water were first obtained in order to determine the position of the plasmon resonance and to set the correct position of the monochromator for the differential measurements, so that the two wavelengths excite the resonance on both sides of the sharp peak. The intensity at each wavelength was then measured by an individual PMT and the signals were processed by the lock-in amplifier displaying the difference between the two signals. The sensitivity of the PMT's differed by a factor of 3, however this was reduced by placing a 0.3 O.D. neutral density filter in front of the more sensitive PMT. Fine balancing was done by adjusting the monochromator to produce zero

difference between the two signals. When adjusting the monochromator, attention was paid to ensure that the two wavelengths probe the resonance on both sides of the sharp peak. After a baseline was established in DI water, varying concentrations of sucrose from 0.01% to 1% were added to change the refractive index from 1.3330 (pure water) to 1.3344 (1% sucrose solution).

3.3 Results and Discussion

Optical sensors based on LSPR exploit the dependence of the resonance frequency on local refractive index. The resonance frequency shift is determined by analyzing the position of the LSPR peak before and after analyte addition. Increasing the sensitivity of a LSPR sensor is commonly a two-fold approach: achieving the sharpest plasmon resonance and achieving the largest spectral shift of the resonance per unit change of the refractive index. Sherry *et al.*¹² defined a FOM by taking the ratio of these two factors to provide a better overall picture of the sensitivity of any given sensor and to allow for easier comparison of different sensors. The LSPR system described in this work takes advantage of an extremely sharp plasmon resonance together with differential optical measurements resulting in record sensing resolutions of bulk refractive index currently achievable by LSPR sensors.

AgNPs can undergo coherent plasmon coupling when assembled into 2D arrays leading to a sharp cooperative resonance with a FWHM of 10-15 nm (**Figure 3.4**). In this case, light interacts not with individual particles but with an ensemble of particles in the array. The resonance is characterized by the coherent

oscillations of the electron density in the neighboring particles. The coherent plasmon coupling was previously reported¹³ and was extensively studied to understand its fundamental properties and potentials for practical applications.^{4b,}

4c, 14

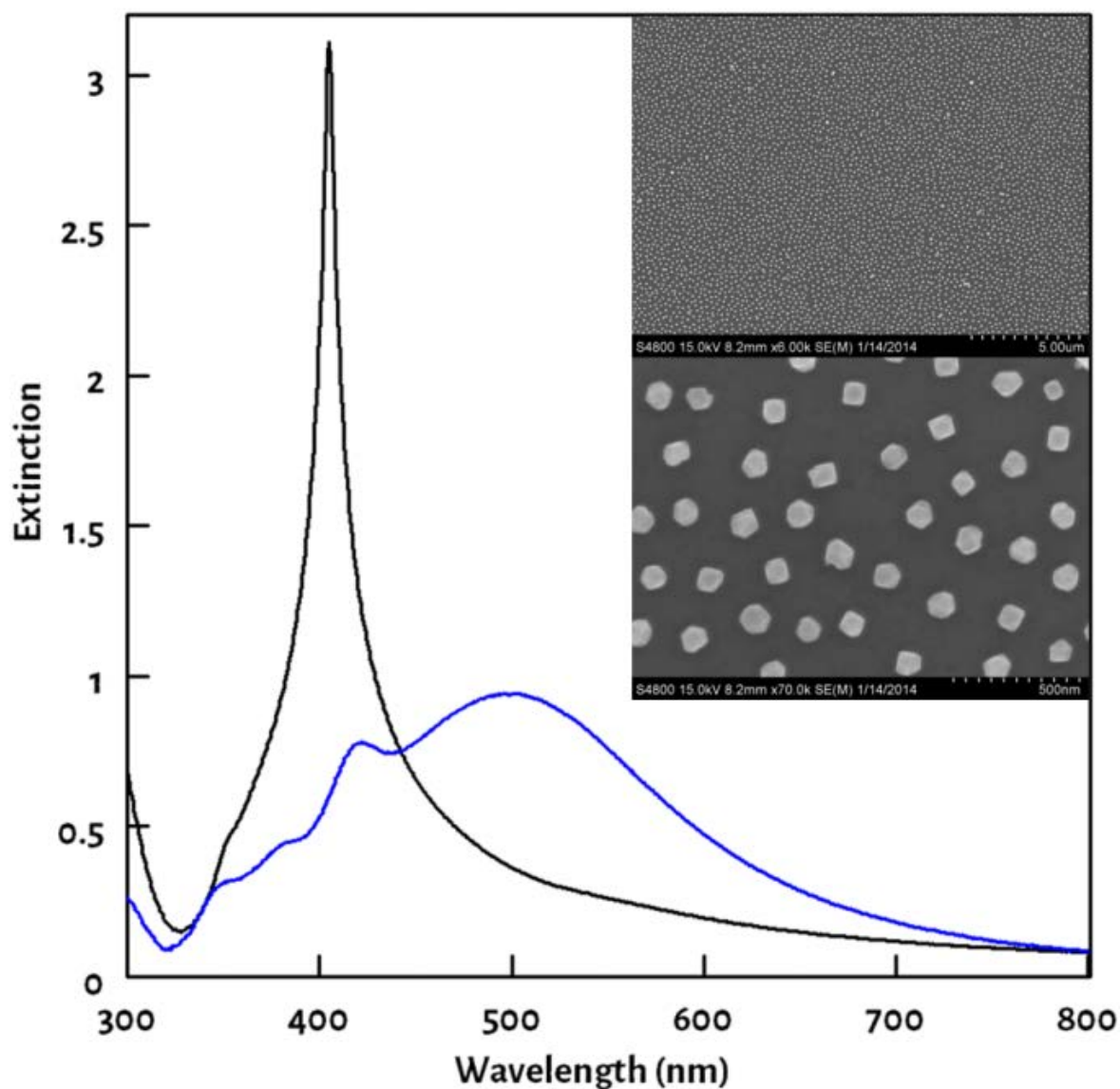


Figure 3.4 Coherent plasmon coupling in 2D array (black) and the same AgNPs in the suspension (blue). Inset: EM images of a coupled 2D array.

The strongest coupling, as evident from the sharpest resonance, occurs at the optimum inter-particle distance that, in turn, depends upon the particle size and dielectric environment. The inter-particle distance can be changed by adjusting the ionic strength of the AgNP solution prior to self-assembly.^{4b} Adjusting the ionic strength is done by addition of sodium sulfate. This was selected due to its inability to reaction with the AgNPs themselves. Since concentration of the AgNPs themselves will play a role on packing density the optical density used was set at 3 and the sodium sulfate concentration was changed from 0 to 2 in 0.5 mM increments. As can be seen the **Figure 3.5** the optimal sodium sulfate concentration for O.D. 3 AgNPs of 100 nm in diameter is 1.5 mM. Once the conditions are optimized, the resonant frequency becomes sensitive to small changes in the dielectric environment in the space between the particles as well as to the presence of different species on the particle surface.

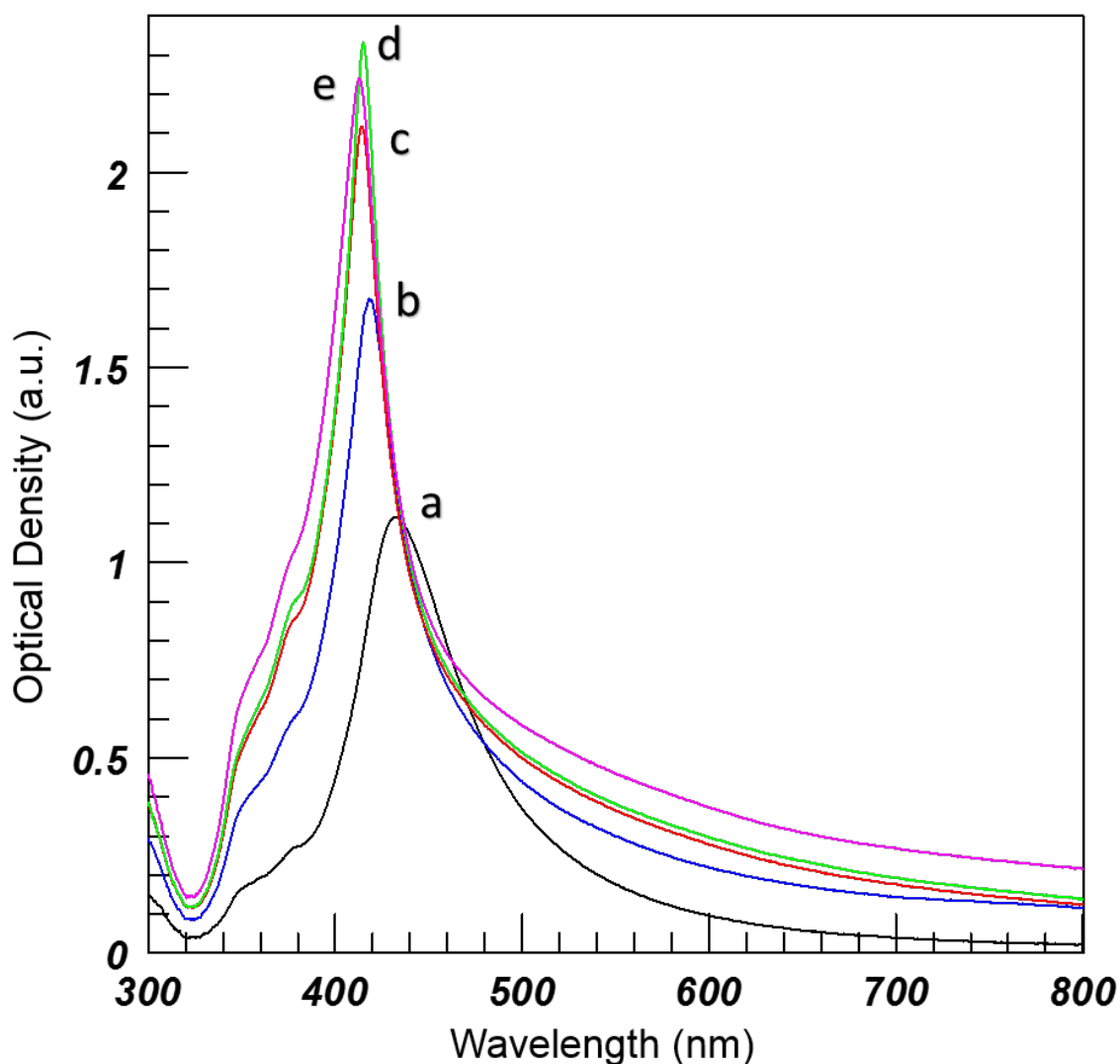


Figure 3.5 UV-Vis of coupling as a result of sodium sulfate concentration of AgNPs in 2D arrays for 0 mM (a) 0.5 mM (b) 1 mM (c) 1.5 mM (d) & 2 mM (e) salt concentrations.

As a result of being self-assembled on the substrate surface the AgNPs undergo a ripening period over the span of 2-3 days. During this time the resonance will blue shift and sharpen until a maximum is reached at which point it no longer changes and is available for use. It is believed that during this period the AgNPs are rearranging on the surface to be more energetically favorable, ultimately resulting in a more uniform interparticle distance thus providing better

coupling and a sharp resonance. **Figure 3.6** shows the change over a period of 3 days.

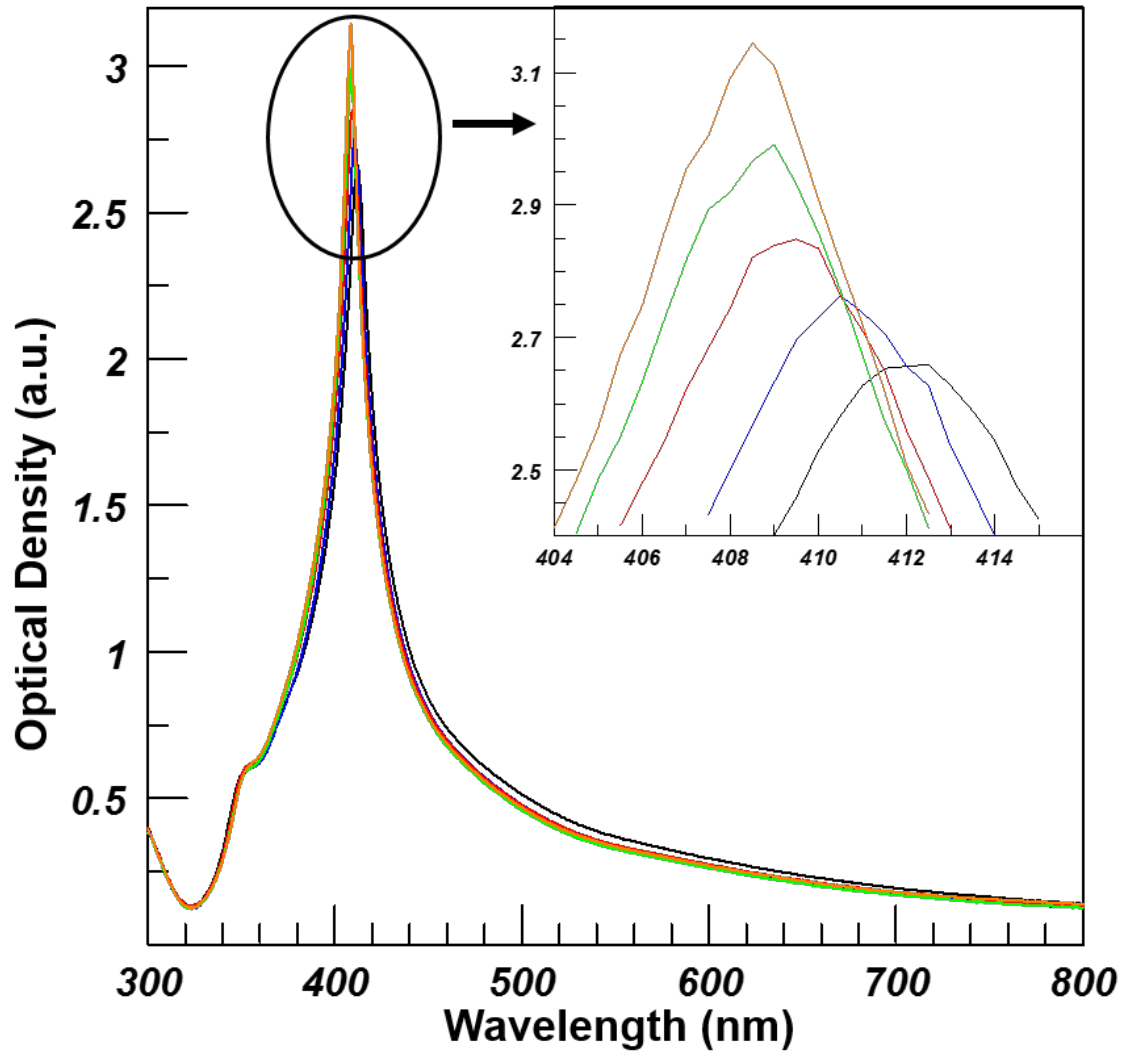


Figure 3.6 UV-Vis of a 2D array demonstrating how the resonance blue shifts and sharpens over a period of 3 days. Insert is zoomed in view of peak region.

The effect of the local dielectric function on the plasmon resonance of individual particles is well understood: the polarizability of the particles increases and the resonance shifts to the red in the media with higher dielectric function.¹⁵ This is due to the screening charges induced in the polarizable medium.^{15b, 16} The

charges produce the 'restoring force' to the oscillating electrons that increases with dielectric function. If the same argument is applied to plasmon coupling between particles, as was previously done in the literature, the medium should shield the local EM field, reducing the coupling in media with a higher dielectric function. Our experiments and modeling results demonstrate the opposite behavior: the plasmon coupling in 2D arrays increases with the increase of the surrounding dielectric function. This can be explained by recognizing that the coupling takes place by means of the local EM field produced by plasmon resonance. This field has a square dependence on the particles' polarizability that also increases with the dielectric function of the medium. Because of this square dependence, the local field increases faster than the 'restoring force', thus producing net gain in the coupling.^{4c}

A recent modification of AgNP synthesis by hydrogen reduction of silver(I) oxide, mainly the addition of fumed silica to the reaction, has eliminated the formation of rods and platelets that otherwise comprise up to ~5% of all nanoparticles. In addition, this modification also increased the concentration of AgNPs by two orders of magnitude, from an optical density (O.D.) of 1 to an O.D. typically around 100. The relevance of this modification to the preparation of LSPR substrates is that having a highly concentrated stock solution of fairly monodisperse spherical AgNPs permits reproducible fabrication of many 2D arrays. This is a cost effective way for substrate preparation since each substrate requires about 4 mL of AgNP solution at O.D. 3 thereby allowing the fabrication of ~25,000 substrates from a single batch of AgNPs. Once the method is optimized in terms

of AgNPs and sodium sulfate concentrations to yield the optimal packing density that provides the narrowest plasmon resonance, reproducible substrates can be fabricated quickly and efficiently.

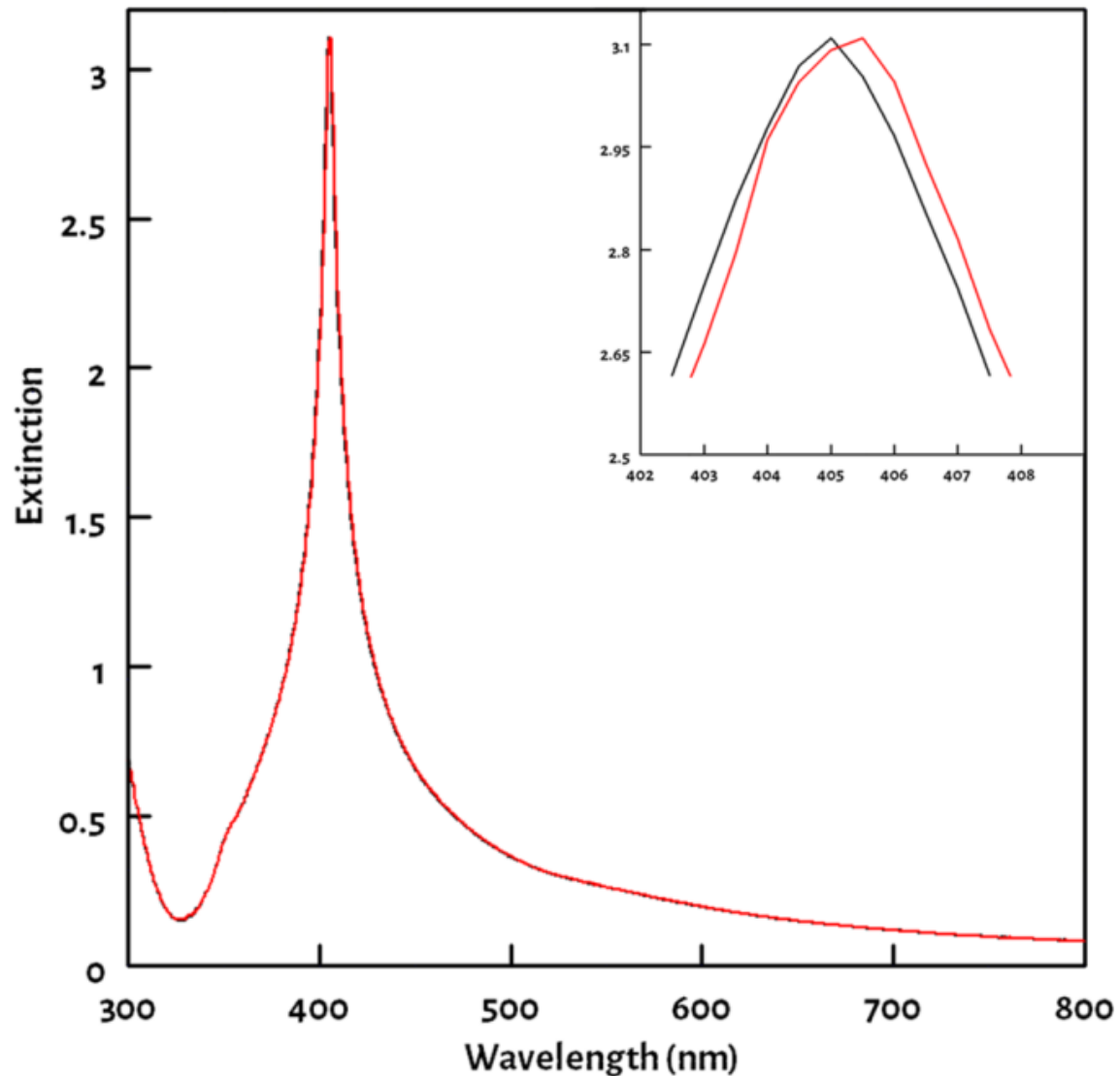


Figure 3.7 Spectral shift of the resonance after changing the refractive index of the medium by $1.4\text{E-}3$ units and measured using conventional UV-Vis spectroscopy. Insert: Magnified region around the peak of the resonance.

The instrument developed here as a part of the LSPR sensor doesn't directly provide the capability for measuring the resonance peak position, therefore

a UV-Vis spectrometer was used to estimate the FOM of the substrates. It can be seen that exposing the substrate to a 1% sucrose solution (representing 1.4E^{-3} relative change of the bulk refractive index from that of DI water) resulted in a 0.5 nm red shift of the LSPR (**Figure 3.7**). This shift could be due to the contribution from both, binding of sucrose to silver surface and the increase of the refractive index in the bulk medium surrounding AgNPs. To rule out the possible contribution from sucrose binding, the dependence of the LSPR shift on sucrose concentration was determined. A nonlinear dependence was expected in the case of sucrose binding. However, as evident from **Figure 3.8**, the dependence was linear resulting in a sensitivity of $\sim 357 \text{ nm} \cdot \text{RIU}^{-1}$. FOM was calculated to be ~ 23 using 15 nm FWHM of the LSPR. This FOM exceeds typical figures reported for metal nanoparticles of $0.9 - 5.4^{17}$ and is on par with maximum FOM reported for substrates fabricated by more common top-down lithographic techniques such as that obtained by Henzie *et al.* for ordered arrays of nanoholes fabricated by soft interference lithography in gold.¹⁸

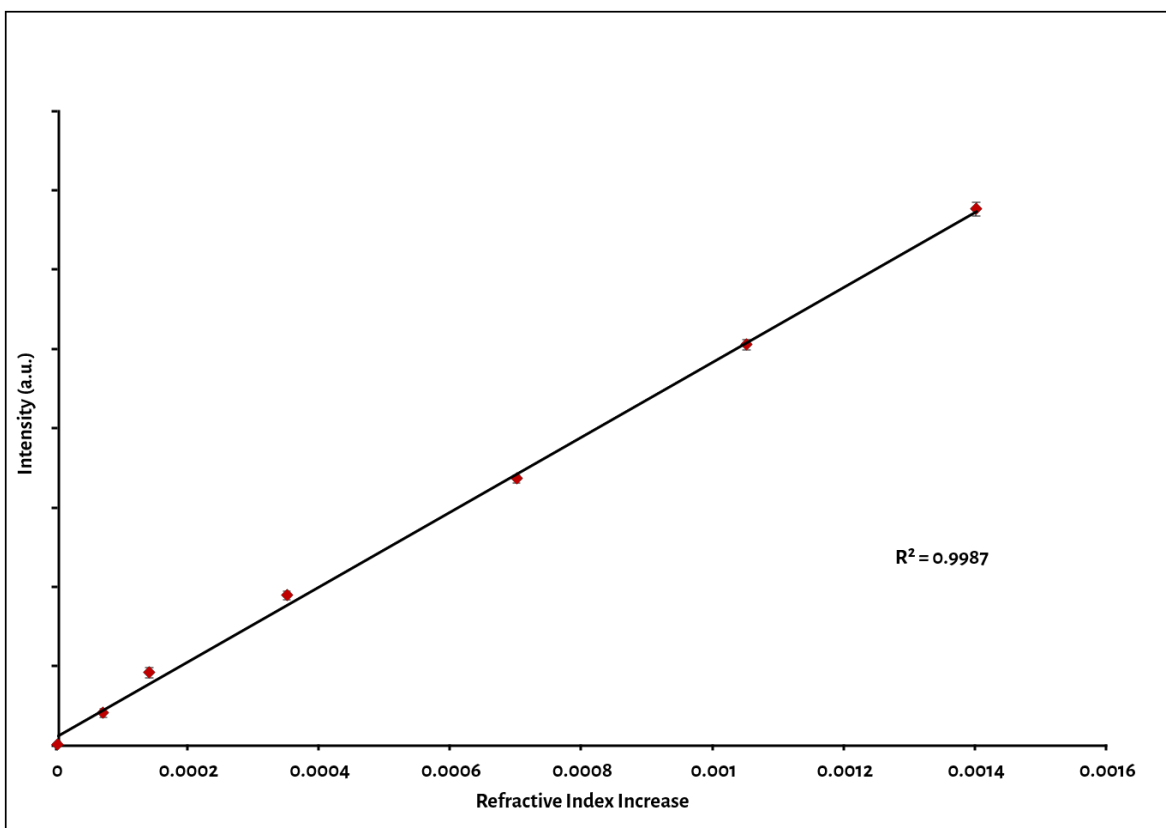


Figure 3.8 Linear relationship between the differential signal and the change of the refractive index.

The 2D arrays of AgNPs were previously demonstrated to exhibit the LSPR shift upon changing the bulk refractive index by immersing the array into various solvents. However the sensing resolution was limited to 6E-4 most likely due to the use of a standard bench top spectrometer for the measurements.¹⁴ In this work, a new approach based on differential optical measurements is implemented for monitoring LSPR shifts resulting from small changes of the bulk refractive index. This differential measurement provides clear advantages compared to using a standard spectrophotometer by significantly improving the sensing resolution and providing real time measurement capabilities. As can be seen in **Figure 3.7**, the change in the LSPR peak position using a conventional spectrometer can be

barely detected even after such relatively large change ($1.4\text{E-}3$) of the bulk refractive index, whereas using the differential measurement system the same change of the refractive index resulted in a significant increase in signal with a S/N of ~ 81 . This is illustrated in **Figure 3.9**, where the differential signal is shown as a function of the increase of the refractive index in the bulk solution over time to a maximum corresponding to a 1% sucrose solution in water.

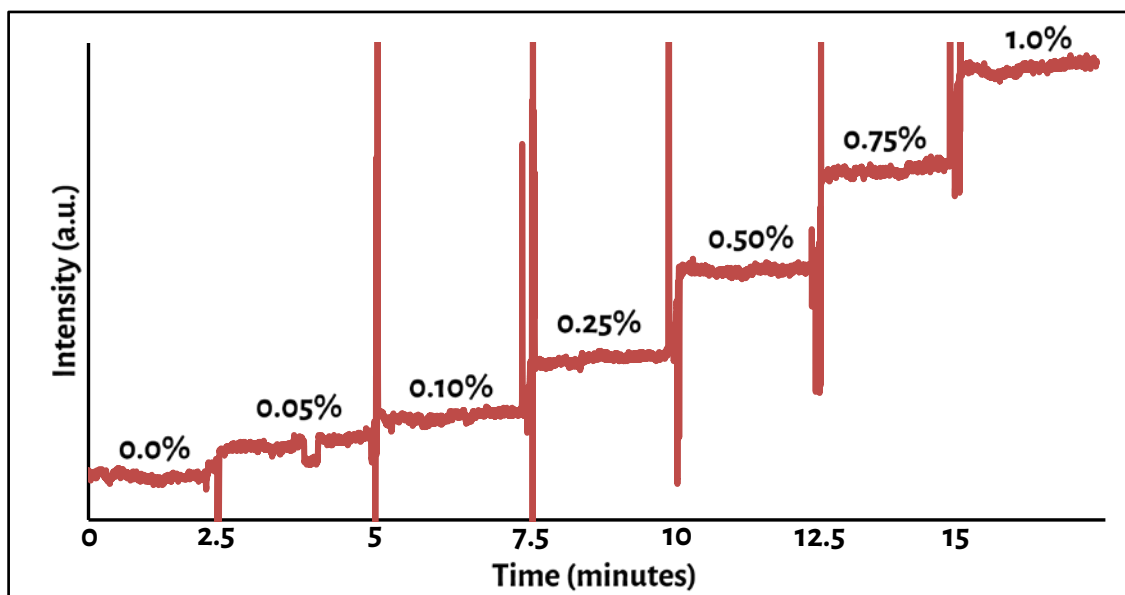


Figure 3.9 Differential signal as a function of serial addition of sucrose solution. Vertical lines correspond to the noise spikes due to the injection. Percentages correspond to final concentration of sucrose in solution. Data was collected for 2.5 minutes before next addition was performed.

After establishing the linear relationship between the differential signal and the bulk refractive index change (**Figure 3.7**), the limit of detection (LOD) was calculated by extrapolating data to a S/N of 3. According to data in **Figure 3.10**, the signal with S/N of 8.77 (noise was averaged over 60 seconds with the time constant of 300 millisecond) was produced by $1.4\text{E-}5$ change of the bulk refractive index. From this the bulk refractive index sensing resolution was calculated to be

4.8E-6 RIU corresponding to 1.7E-3 spectral shift of the LSPR. Such small spectral shifts are difficult to measure using conventional spectrometers. Hook *et al.* achieved comparable bulk sensing resolution, however this was only achieved using data analysis algorithms and an instrumental setup optimized to reduce noise.¹⁹ Therefore the differential measurement implemented here, which achieved high sensing resolutions prior to implementation of any computer assisted signal determination methods while using crude sampling methodologies and without any regards to reduction of system noise, sets a remarkable baseline that is only expected to improve. A recent publication by Wang *et al.* reported a LSPR substrate fabricated by lithographic techniques having FOM ~ 108 .⁸ Even though this FOM is significantly higher than those previously reported including the current work, their estimated sensing resolution was only $\sim 2\text{E-}4$ RIU due to the limited spectral resolution (0.1 nm) of the optical detection system, as reported by the authors. This result further emphasizes the advantages of the differential optical measurements to improve the sensing resolution of other LSPR sensors.

Typical SPR sensors based on refractometric measurements usually exhibit a sensitivity to changes in bulk solution between $1\text{E-}6$ and $1\text{E-}7$ RIU.²⁰ This high sensitivity can be partially attributed to the relatively large depth (>100 nm) for the field penetration which significantly exceeds the penetration depth typical for LSPR. However when SPR sensors are compared to similar LSPR sensors²¹ in terms of sensing local binding events, they show very similar results even though the bulk sensitivity is at least an order of magnitude better for SPR. Therefore, achieving such high bulk sensitivities for the LSPR sensor described here has promise for

even higher sensitivities to surface binding events. It is important to emphasize that the reported here record sensing resolution for LSPR sensors was obtained in an open system using a simple optical setup with off-the-shelf components and without any optimization. As is evident from **Figure 3.10**, the detector noise is likely the main limiting factor. Additional improvements of this system, such as using small balanced detector pairs or single detector with out-of-phase modulation of the optical channels, noise reduction technologies and a flow cell will lead to miniaturization and cost reduction and further improvements of the sensitivity.

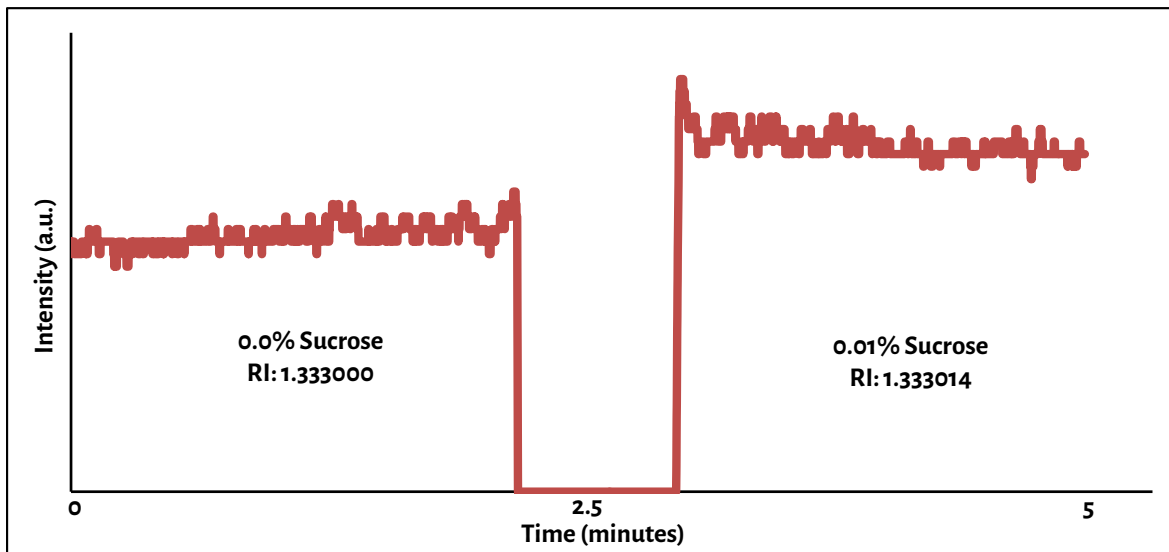


Figure 3.10 Data collected after inducing a change in refractive index of $1.4\text{E-}5$

3.4 Conclusion

A novel system based on LSPR was proposed and implemented for measuring small changes of the bulk refractive index. Record sensing resolution of $4.8\text{E-}6$ RIU was achieved. This resolution resulted from the combination of the two factors: the sharpness of the coherent plasmon resonance of 2D arrays of

AgNPs and the differential optical measurement method. In addition to the high performance, the system is simple and inexpensive to implement and is not limited by the instrument spectral resolution as many other systems are. The fabrication of LSPR substrates relies on the self-assembly process of chemically synthesized nanoparticles as opposed to more complicated lithographic techniques. The optimization of the detection system as well as the addition of a flow cell sample handling system, a standard approach in commercial instruments, will further improve the performance of this sensor. It is anticipated that this technology can be developed into more efficient and cost-effective alternatives to current commercially available instruments based on plasmon resonances.

3.5 Acknowledgments

This research was supported by the United States Department of Energy, grant No. DE-FG02-06ER46342.

3.6 References

1. Brolo, A. G., Plasmonics for Future Biosensors. *Nat. Photonics* **2012**, 6 (11), 709-713.
2. Homola, J., Surface Plasmon Resonance Sensors for Detection of Chemical and Biological Species. *Chem. Rev.* **2008**, 108 (2), 462-93.
3. Moreira, C. S.; Lima, A. M. N.; Neff, H.; Thirstrup, C., Temperature-dependent Sensitivity of Surface Plasmon Resonance Sensors at the Gold-water Interface. *Sens. Actuators, B* **2008**, 134 (2), 854-862.

4. (a) Kelly, K. L.; Coronado, E.; Zhao, L. L.; Schatz, G. C., The Optical Properties of Metal Nanoparticles: The Influence of Size, Shape, and Dielectric Environment. *J. Phys. Chem. B* **2003**, *107* (3), 668-677; (b) Kinnan, M. K.; Chumanov, G., Plasmon Coupling in Two-dimensional Arrays of Silver Nanoparticles: II. Effect of the Particle Size and Interparticle Distance. *J. Phys. Chem. C* **2010**, *114* (16), 7496-7501; (c) Kinnan, M. K.; Kachan, S.; Simmons, C. K.; Chumanov, G., Plasmon Coupling in Two-dimensional Arrays of Silver Nanoparticles: I. Effect of the Dielectric Medium. *J. Phys. Chem. C* **2009**, *113* (17), 7079-7084.
5. Wang, Q.; Yu, C. X., Chemical and Biological Sensing and Imaging Using Plasmonic Nanoparticles and Nanostructures. In *Biomedical Nanosensors*, Irudayaraj, J., Ed. Pan Stanford Publishing Pte. Ltd.: Singapore, 2013; Vol. 3, pp 59-96.
6. (a) Stewart, M. E.; Anderton, C. R.; Thompson, L. B.; Maria, J.; Gray, S. K.; Rogers, J. A.; Nuzzo, R. G., Nanostructured Plasmonic Sensors. *Chem. Rev.* **2008**, *108* (2), 494-521; (b) Guzenko, V. A.; Ziegler, J.; Savouchkina, A.; Padeste, C.; David, C., Fabrication of Large Scale Arrays of Metallic Nanodots by Means of High Resolution E-beam Lithography. *Microelectron. Eng.* **2011**, *88* (8), 1972-1974.
7. Jones, M. R.; Osberg, K. D.; Macfarlane, R. J.; Langille, M. R.; Mirkin, C. A., Templated Techniques for the Synthesis and Assembly of Plasmonic Nanostructures. *Chem. Rev.* **2011**, *111* (6), 3736-827.
8. Shen, Y.; Zhou, J.; Liu, T.; Tao, Y.; Jiang, R.; Liu, M.; Xiao, G.; Zhu, J.; Zhou, Z. K.; Wang, X.; Jin, C.; Wang, J., Plasmonic Gold Mushroom Arrays with

Refractive Index Sensing Figures of Merit Approaching the Theoretical Limit. *Nat. Commun.* **2013**, 4, 2381-2389.

9. Estevez, M. C.; Otte, M. A.; Sepulveda, B.; Lechuga, L. M., Trends and Challenges of Refractometric Nanoplasmonic Biosensors: A Review. *Anal. Chim. Acta.* **2014**, 806, 55-73.

10. Englebienne, P., Use of Colloidal Gold Surface Plasmon Resonance Peak Shift to Infer Affinity Constants From the Interactions Between Protein Antigens and Antibodies Specific for Single or Multiple Epitopes. *Analyst* **1998**, 123 (7), 1599-1603.

11. Mazzotta, F.; Wang, G.; Haegglund, C.; Hoeoek, F.; Jonsson, M. P., Nanoplasmonic Biosensing with On-chip Electrical Detection. *Biosens. Bioelectron.* **2011**, 26, 1131-1136.

12. Sherry, L. J.; Chang, S. H.; Schatz, G. C.; Van Duyne, R. P.; Wiley, B. J.; Xia, Y., Localized Surface Plasmon Resonance Spectroscopy of Single Silver Nanocubes. *Nano. Lett.* **2005**, 5 (10), 2034-2038.

13. Malynych, S.; Chumanov, G., Light-induced Coherent Interactions between Silver Nanoparticles in Two-dimensional Arrays. *J. Am. Chem. Soc.* **2003**, 125 (10), 2896-2398.

14. Malynych, S.; Chumanov, G., Coupled Planar Silver Nanoparticle Arrays as Refractive Index Sensors. *J. Opt. A: Pure Appl. Opt.* **2006**, 8 (4), S144-S147.

15. (a) Jensen, T. R.; Duval, M. L.; Kelly, K. L.; Lazarides, A. A.; Schatz, G. C.; Van Duyne, R. P., Nanosphere Lithography: Effect of the External Dielectric Medium on the Surface Plasmon Resonance Spectrum of a Periodic Array of Silver

Nanoparticles. *J. Phys. Chem. B* **1999**, *103* (45), 9846-9853; (b) Jain, P. K.; Eustis, S.; El-Sayed, M. A., Plasmon Coupling in Nanorod Assemblies: Optical Absorption, Discrete Dipole Approximation Simulation, and Exciton-coupling Model. *J. Phys. Chem. B* **2006**, *110* (37), 18243-18253; (c) Novo, C.; Funston, A. M.; Pastoriza-Santos, I.; Liz-Marzan, L. M.; Mulvaney, P., Influence of the Medium Refractive Index on the Optical Properties of Single Gold Triangular Prisms on a Substrate. *J. Phys. Chem. C* **2008**, *112* (1), 3-7.

16. (a) Choi, B. H.; Lee, H. H.; Jin, S.; Chun, S.; Kim, S. H., Characterization of the Optical Properties of Silver Nanoparticle Films. *Nanotechnology* **2007**, *18* (7), 075706; (b) Sih, B. C.; Wolf, M. O., Dielectric Medium Effects on Collective Surface Plasmon Coupling Interactions in Oligothiophene-linked Gold Nanoparticles. *J. Phys. Chem. B* **2006**, *110* (45), 22298-22301.

17. Liao, H.; Nehl, C. L.; Hafner, J. H., Biomedical Applications of Plasmon Resonant Metal Nanoparticles. *Nanomedicine-U.K.* **2006**, *1* (2), 201-8.

18. Henzie, J.; Lee, M. H.; Odom, T. W., Multiscale Patterning of Plasmonic Metamaterials. *Nat. Nanotechnol* **2007**, *2* (9), 549-554.

19. Dahlin, A. B.; Tegenfeldt, J. O.; Hook, F., Improving the Instrumental Resolution of Sensors Based on Localized Surface Plasmon Resonance. *Anal. Chem.* **2006**, *78* (13), 4416-4423.

20. (a) Bolduc, O. R.; Live, L. S.; Masson, J. F., High-resolution Surface Plasmon Resonance Sensors Based on a Dove Prism. *Talanta* **2009**, *77* (5), 1680-1687; (b) Piliarik, M.; Homola, J., Surface Plasmon Resonance (SPR) Sensors: Approaching Their Limits? *Opt. Express* **2009**, *17* (19), 16505-16517.

21. (a) Svedendahl, M.; Chen, S.; Dmitriev, A.; Kall, M., Refractometric Sensing Using Propagating versus Localized Surface Plasmons: A Direct Comparison. *Nano Letters* **2009**, 9 (12), 4428-4433; (b) Otte, M. A.; Sepulveda, B.; Ni, W.; Perez Juste, J.; Liz-Marzan, L. M.; Lechuga, L. M., Identification of the Optimal Spectral Region for Plasmonic and Nanoplasmonic Sensing. *ACS Nano* **2010**, 4 (1), 349-357.

CHAPTER FOUR

SURFACE-ENHANCED RAMAN SPECTROSCOPY AND CHEMIREซิสTOR APPLICATIONS

4.1 Introduction

To further demonstrate the applicability of these nanoparticles they were integrated into substrates for both surface-enhanced Raman spectroscopy and vapor sensing via a chemiresistor. We also show potential for stabilizing the particles in both 2D & 3D polymer matrixes. These applications take advantage of both the ultra-thin silica shell in addition to the high concentration that can be achieved with ease and stability.

4.1.1 Surface-Enhanced Raman Spectroscopy

The Raman effect occurs when a photon is incident on a molecule, interacting with the electric dipole of the molecule and causing a change in the molecules polarizability.¹ This can essentially be viewed as a perturbation of the electric field of the molecule. The scattering that is observed can be described as the excitation of a molecule to a virtual state that is lower in energy than a real electronic transition.

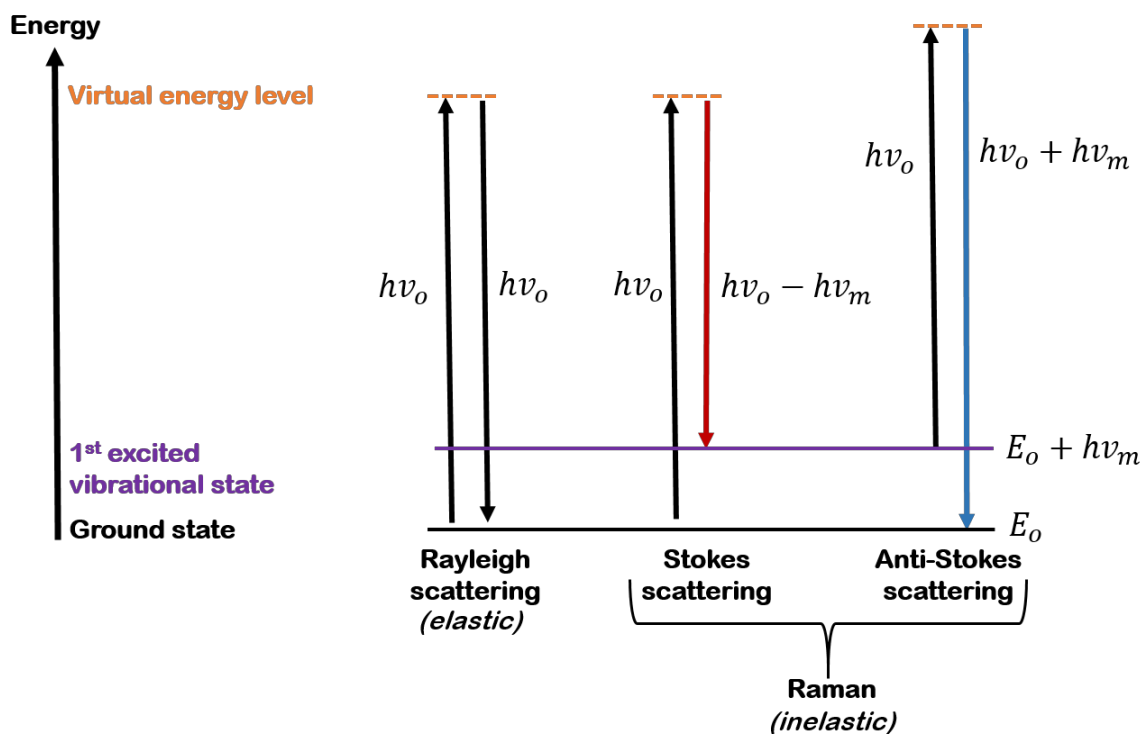


Figure 4.1 Energy level diagram illustrating Rayleigh, Stokes & anti-Stokes scattering.

The arrows in the energy level diagram (**Figure 4.1**) represent the energy difference between the incident photons and scattered photons which can be calculated using the following equation:

$$\bar{\nu} = \frac{1}{\lambda_{\text{incident}}} - \frac{1}{\lambda_{\text{scattered}}} \quad (1)$$

Where ν is the Raman shift in cm^{-1} while $\lambda_{\text{incident}}$ is the energy of the photons interacting with the molecule and $\lambda_{\text{scattered}}$ is the energy of the photon emitted from the molecule. In an inelastic scattering event these energies differ. Unfortunately, the majority of the scattered light is Rayleigh scattering with Raman scattering only occurring for a very small fraction of the incident photons, thereby requiring a high

concentration of Raman active molecules. It was observed that the Raman scattering from pyridine adsorbed on a roughened silver electrode resulted in an enhanced signal by Fleischmann in 1974 and was later confirmed and recognized as a surface-enhanced effect by van Dyne in 1977.² This phenomenon is known as surface-enhanced Raman scattering (SERS) and has gained much interest since its discovery. It is postulated that the SERS effect arises from two separate mechanisms, electromagnetic (EM) enhancement and chemical enhancement.³ EM enhancement is due to an enhanced EM field at the metal surface. When the wavelength of the incident light matches or is close to the plasmon wavelength of the metal then the electrons in the conduction band of the metal are excited into an extended surface electronic excited state (explained in Chapter 1). Molecules absorbed or in close proximity to this EM hot-spot experience an exceptionally large enhancement with vibrational modes normal to the surface experiencing the strongest enhancement. The second type of enhancement arises from the formation of a charge-transfer complex between the metal surface and the molecule of interest.

SERS has been integrated into a wide variety of applications, however the competing contributions between the two different mechanisms are still being explored and published on. Here we demonstrate a simple SERS substrate that is easily prepared and introduce a technique that allows us to probe the SERS of the un-aggregated state where we would ideally be mostly probing the chemical enhancement and then induce aggregation via drying and see a large increase in

our SERS signal while probing the same concentration of AgNPs and analyte. This is applicable for molecules that are able to absorb through the ultra-thin silica shell to adsorb on the metal surface.

While it has not yet been investigated, the AgNPs are also ideal for a technique known as shell-isolated nanoparticle-enhanced Raman spectroscopy (SHINERS) which has been explored over the past decade. In SHINERS a chemically inert shell is coated around the metal nanoparticle which both protects the particle but is thin enough (<2 nm) that the EM enhancement still plays a role. The thin shell is advantageous because it keeps the nanoparticles from agglomerating and protects them from contact with the surface being probed while still allowing it to contour to the shape of the sample. This technique has been used for applications such as detection of pesticide residue on food and fruit as well as detection of hydrogen adsorption on single-crystal flat surfaces of Pt and Si.⁴

4.1.2 Chemiresistor

Gas sensors have been used in a multitude of applications to monitor and detect a huge variety of gases, vapors, humidity and odors. Prominent examples include detection of CO₂ in exhaust gases for environmental protection and detection of trace explosives for security reasons. In a laboratory environment these things can be easily measured using techniques such as mass spectrometry or various spectroscopic or chromatography methods. However the application using these methods will be limited by cost, size and instrumentation complexity.

This has helped promote the development of solid-state gas sensors that are low-cost, mobile and are built from a bottom-up approach. These sensors should selectively transform chemical information from either a physical or chemical reaction of the gas on the substrate into a signal that can readily deliver the required response.⁵ Among the many different concepts that meet the criteria such as those based on quartz microbalances⁶ or gas sensitive field-effect transistors⁷, the most common are chemiresistors. A chemiresistor rely on a direct chemical or physical interaction between the sensing material and analyte that cause a change in its electrical resistance. A very basic chemiresistor will consist of a sensing material, which has an inherent resistance that can be changed by the presence or absence of an analyte, bridging the gap between two electrodes (**Figure 4.2**). This change in resistance can be proportional to the amount of analyte detected thus allowing for quantification or simply indicate the presence of an analyte.

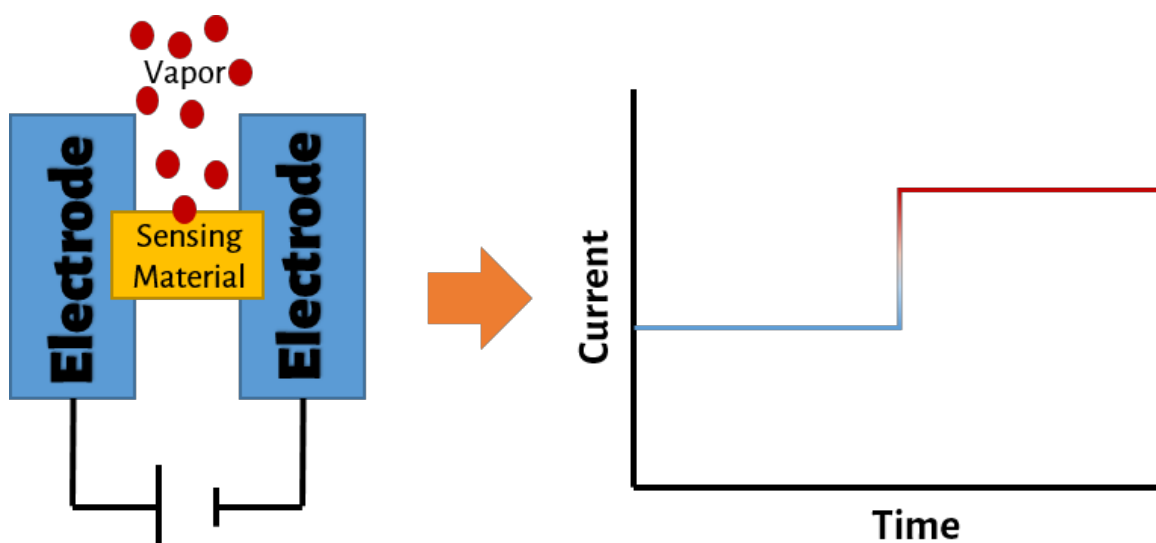


Figure 4.2 Basic schematic of a simple chemiresistor.

Several different sensing materials can be used in chemiresistor fabrication. These include metal oxide semiconductors, carbon nanotubes, graphene, conductive polymers and nanoparticles, the last of which is used to fabricate the device presented here. The sensing mechanism varies for each type of sensing material, the rest of this section will focus on the sensing mechanism undergone by metallic nanoparticles with organic spacers.

The first literature example of coated metal nanoparticles applied to a chemiresistor device appeared in 1998 when Wohltjen and Snow used a film of 2 nm gold nanoparticles coated with octanethiols to demonstrate a rapid and reversible response to several organic and water vapors. They showed that the electronic interactions such as hopping/tunneling between the particles was affected by the uptake of the different vapor molecules into the metal nanoparticle spacer.⁸ When a vapor is absorbed into the spacer layer it will decrease or increase the spacer layer thickness, thus changing the distance between the metal nanoparticles resulting in a large change in resistance. Typically, this change in resistance will vary linearly with vapor concentration and detection limits down to parts-per-billion by volume have been achieved.⁹ In addition to this swelling and shrinking mechanism, the sorption of a vapor with a different dielectric constant than the insulating matrix can result in a change in resistance.¹⁰

4.2 **Materials & Methods**

4.2.1 *Materials*

Poly(ethylene glycol) dimethacrylate M_n 550 (PEGMDA), Poly(4-vinylpyridine) (PVP), adenine (99%), guanine (98%), and zinc powder (ACS grade) were purchased from Sigma Aldrich. Acetone (ACS grade) and anhydrous sodium sulfate were purchased from Fisher Scientific. Silver(I) oxide (99.99%) and USP absolute-200 proof ethanol were acquired from Alfa Aesar and Aaper Alcohol & Chemical Co., respectively. Cyclohexane (HPLC grade) and chloroform (99.8%) were purchase from Acros Organics. Selex Reverse Primer (5' TCAAGT GGT CAT GTA CTA GTC AA 3') was obtained from Dr. Christensen. Quinoxolinol salen ligand and it's complex with uranyl were synthesized by the Anne Gorden group at Auburn University. Irgacure 819Dw initiator was obtained from BASF. Fumed silica (99.8%) was purchased from Sigma-Aldrich and purified by heating at 500 °C for 5 hours under vacuum. Deionized water with a nominal resistivity of 18 M Ω ·cm came from a Millipore Milli-Q water purification system. Ultra-high-purity hydrogen and ultra-high-purity nitrogen were purchased from Air Gas. PVP solutions were prepared by dissolving a weighed quantity in ethanol. Indium tin oxide (ITO) glass (8-12 Ω /sq inch) was received from Sigma and Delta Technologies, LTD. Unless specified, all reagents and solvents were used as received.

4.2.2 Instrumentation

UV-Vis spectra were recorded using a Shimadzu UV-2501PC spectrophotometer. Electron microscopy images were taken with a Hitachi SEM-4800. Raman spectra was measured directly from the samples using a spectrograph (SPEX, Triplemate 1377) interfaced to a thermoelectrically cooled CCD detector (Andor Technology, Model DU420A-BV) operating at -60 °C. The spectra were excited with 514.5 nm radiation from an Innova 100 (Coherent) argon ion laser. The laser power was between 5-25 mW at the sample with a total acquisition time of 100 seconds for each measurement. The scattered light was collected by a f/1.2 camera lens in a backscattering geometry, and the instrument was calibrated using an indene and chloroform/bromoform standard. The current-time curves were measured by using an electrochemical workstation (CH Instruments, CHI440) with chronoamperometry. All Raman and UV-Vis spectra and figures prepared with Spectra-Solve for Windows software (LasTek Pty. Ltd.).

4.2.3 Synthesis of Silver Nanoparticles

AgNPs were synthesized using the modified hydrogen reduction method describe in Chapter 2. Briefly, after the addition of silver(I) oxide to deionized water in a round-bottom flask, the synthesis was performed at 73 °C under 10 psi excess pressure of hydrogen gas in the presence of 1 mM fumed silica. All AgNPs used in this study were single crystals with a Feret's diameter of ca. 100 nm with a 1 nm silica shell.

4.2.4 Preparation of SERS Substrates

Standard microscope slides were cut into 11 mm x 25 mm sized pieces and cleaned by sonication in acetone, ethanol and water baths for 15 minutes each followed by drying with nitrogen gas and plasma treating for 10 minutes. After cleaning, the slides were placed into a 0.1% PVP solution and allowed to roll coat for 4 hours. Following PVP exposure, ethanol and water rinses were performed after which the slides were dried with nitrogen gas and annealed at 120 °C for 3 hours. Next, slides were quickly cooled with a stream of nitrogen gas and rolled overnight in aqueous suspensions of ~100 nm AgNPs with an O.D. of 3 containing 1.5 mM sodium sulfate. After the nanoparticle adsorption, the slides were rinsed with water and one side of the slide was stripped of AgNPs using a dilute nitric acid solution. The slides were thoroughly rinsed and stored in deionized water. Slides were then exposed to aqueous solutions of adenine, guanine and ssDNA overnight. Slides were then rinsed with DI water to remove unabsorbed analyte and placed in fresh DI water in clean 1 dram vials. Raman spectra was collected on this system after which they were dried at 100 °C for 2-3 minutes before being placed back in the DI water. SERS spectra was then collected again to see the effects of aggregation on the system.

4.2.5 Preparation of Chemiresistor Vapor Sensor

AgNPs were grown using the above method but in a 5 L quartz reaction vessel instead of the usual 500 mL vessel. AgNPs were then concentrated by centrifugation (~1000 RPM or 175 G's) for 30 minutes. This was repeated until a

volume of ~2 mL of AgNPs was obtained with an O.D. of ~2500. ITO glass was cut into 1 x 2.5 cm strips. Scotch tape was used to mask all but a ~1-2 mm strip down the middle of the glass slide. This strip was then coated with zinc powder and exposed to 2M HCl for 15 minutes to etch the ITO followed by rinsing with DI water and removal of the mask. A multi-meter was used across this strip to confirm the ITO layer had been removed. 2.5 μ L of the concentrated AgNPs were then pipetted onto this strip and allowed to dry for 1-2 minutes in the 100 °C. current-voltage curves were performed across the device afterwards and a large hysteresis effect was observed. The slides were then annealed at 100 °C for 24 hours, current-voltage curves were then taken again and showed a linear relationship. Data was collected by positioning the sensor ~2 mm above a 25 mL Erlenmeyer flask (**Figure 4.3**). Data was collect for 50 seconds before positioning the flask containing the various analytes under the sensor for 50 seconds followed by removal to show a reversible response. This was continued for a period of 500 seconds for each analyte. Data was collect at a potential of 1V & -0.05 V with a sampling interval of 0.0315 seconds and a sensitivity of 1E-3 and 5E-5, respectively.



Figure 4.3 Picture of entire chemiresistor setup & sampling method.

4.2.6 *Preparation of 2D & 3D Assemblies of AgNPs in Polymer Matrix*

In order to prepare stable suspensions of colloids in PEGMDA they first had to be conditioned with a lesser quantity. To do this, 1 mL of 1% PEGMDA in water was placed in a 1 dram vial and stirred with a flea stir bar. While stirring, 500 μL of 2,500 O.D. AgNPs in water (510 nm dipole) was added in 25 μL aliquots resulting in a suspension with an O.D. of 313 and a dipole position of 510 nm. Following this 7.5 mg of 40% initiator (Irgacure 819 dW) was added to obtain a final concentration of 0.1% after which was added 2.4 g of PEGMDA. While stirring, 0.6 g of the previously conditioned AgNP suspension was added resulting in a solution with a

dipole at 520 nm and an O.D. of 40. To prepare the 3D assemblies, 200 μL of the as prepared solution was pipetted onto a microscope slide and covered with a glass cover slip before being exposed to 365 nm UV light for 10 minutes. The resulting assembly was interrogated via UV-Vis revealing that the plasmon resonance was maintained but was red shifted with a final dipole position at 550 nm. The resonance was maintained even after exposure to 10% nitric acid.

To prepare 2D assemblies, 2D arrays of AgNPs were prepared as described above. A solution of 79.75% PEGMDA, 20% water & 0.25% Irgacure 819 dW was then mixed and sonicated for 1 minute. The 2D array was then dried and 50 μL of the PEGMDA solution was pipetted onto the slide and covered with a glass cover slip. This was then polymerized for 10 minutes using 365 nm UV light followed by peeling off of the film.

4.3 Results and Discussion

The ultra-thin silica shell that occurs during the growth of the AgNPs introduced in Chapter 2 makes them uniquely applicable for both the SERS studies on the effect of induced aggregation in addition to their use as a solid-state vapor sensor. The latter of which takes advantage of both the shell in addition to the extremely high concentrations of AgNPs that can be achieved with relative ease. The simplicity of these applications helps to illustrate the broad potential of the AgNPs grown by this method.

4.3.1 Aggregation Study of SERS Substrate.

Original attempts to use these particles as colloidal SERS systems proved unsuccessful due to the issues with inducing aggregations via increasing ionic strength of the solution, which can be attributed to the stability of the AgNPs as a result of the silica shell. As an alternative, 2D arrays of AgNPs were prepared and investigated as a SERS substrate. The ability to synthesize high concentration stable AgNP suspensions provides the prospect for a number of practical applications. The AgNPs can be readily self-assembled onto PVP modified glass slides yielding high density monolayer films of well-separated particles. By changing pH or the ionic strength of the suspension the interparticle distance can be effectively controlled. These films exhibited strong surface-enhanced Raman scattering activity (SERS) as was demonstrated using three important analytes, nucleobases adenine & guanine and a protein lysozyme. The films also provided a unique opportunity for observing the unobstructed effect of the particle aggregation on the SERS signal. Specifically, the films were exposed to the analyte solutions, thoroughly rinsed, and SERS was measured from the films in DI water. Next, the same films were dried, and SERS was measured again in DI water. The drying induced surface aggregation of the AgNPs due to the high surface tension of water, but both the amount of the analyte and the number of NPs interrogated by the laser beam remained approximately the same. **Figure 4.4** demonstrates this with electron microscopy images of 2D arrays dried from a low

surface tension solvent (ethanol) compared to the a 2D array prepared the same way but dried from water to induce aggregation.

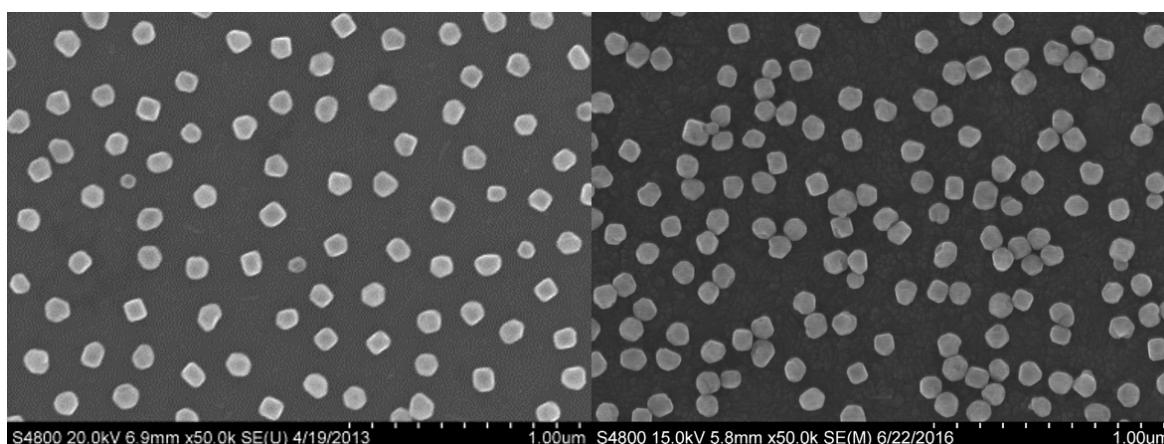


Figure 4.4 SEM images of 2D array dried from a low surface tension solvent (left) and water (right)

To demonstrate that the analytes themselves don't induce a large degree of aggregation the 2D arrays were monitored by UV-Vis. In **Figure 4.5** we see a strong, narrow plasmon resonance in the black curve that corresponds to a strongly coupled, un-aggregated 2D array. The slide was then exposed to 10 μ M guanine overnight and the UV-Vis spectrum was taken again. The blue curve corresponds to this second reading and illustrates that, while a drop is noticeable, the AgNPs still maintains a relatively strong coupling with a sharp plasmon resonance and a low baseline.

Evidence of aggregation is not only seen by a decrease in the plasmon resonance but also by an increase in the baseline due to scattering from aggregates which now can be treated as larger particles and thus exhibit elevated extinction at higher wavelengths where the appearance of a new peak around 750

can be observed. This is evident in the red curve in **Figure 4.5** where we have UV-Vis after drying of the slide with the resulting SEM of the slide after drying in the insert.

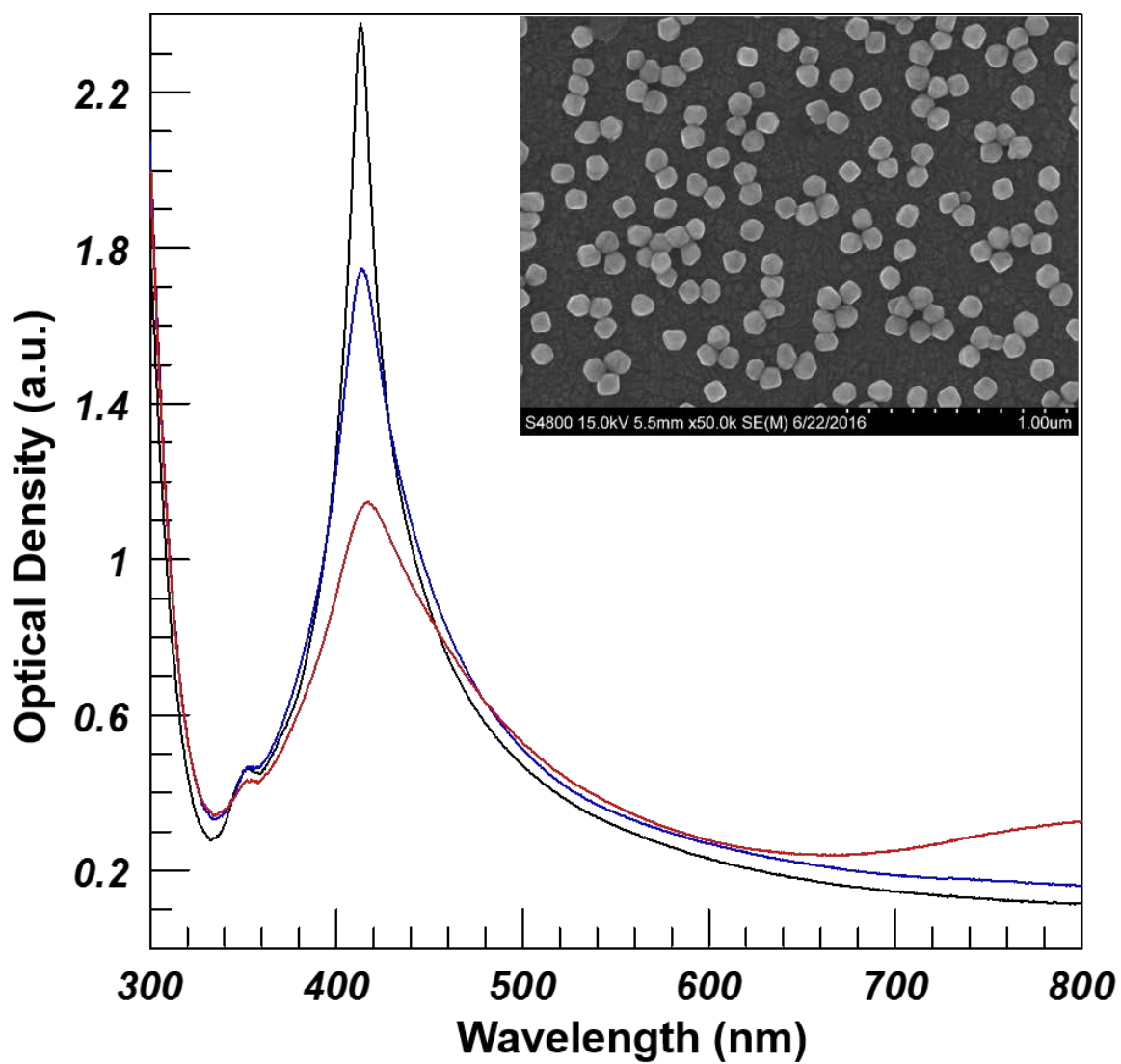


Figure 4.5 UV-Vis of slide exposed to 1 mM guanine in water before (black) and after (blue) drying. Insert: SEM of slide after drying.

As can be seen in **Figure 4.6**, the SERS signal from guanine and adenine increased by 3.5 and 15 fold, respectively, when compared to that from the pre-aggregated state. The poor enhancement of guanine can possibly be attributed to its insolubility in aqueous solution compared to adenine which is water soluble, if poorly. Therefore, while they were both exposed to analyte overnight, the guanine remained a fine dispersion and would have a more difficult time attaching to the analyte surface. Since the AgNPs are assembled on slides and therefore solvent induced aggregation is not as large of a concern, it can be advantageous to select an appropriate solvent for exposure as will be demonstrated with an insoluble analyte in acetone. The additional SERS enhancement resulted from the aggregation signifies the EM enhancement mechanism, in which the local field is concentrated in the spaces between the aggregated particles where the analyte molecules are sandwiched.¹¹ The real enhancement due to the aggregation is most likely larger than that reported in **Figure 4.6** because not all the analyte molecules that are covering the individual NPs ended up in the spaces between the particles. These SERS active films can be fabricated within minutes using the simple self-assembly technique from high concentration AgNP suspensions.

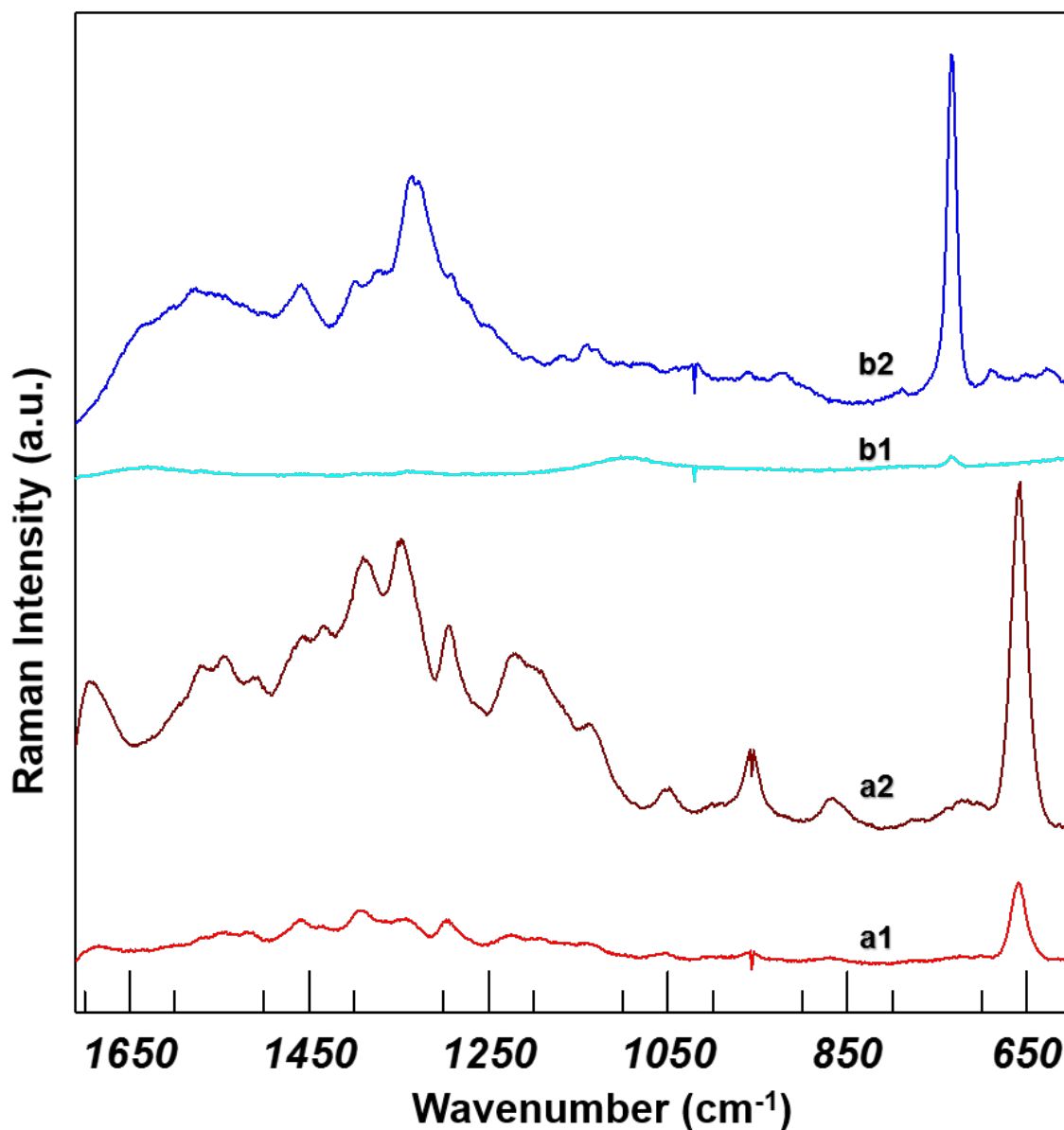


Figure 4.6 SERS of 2D arrays of AgNPs exposed to 10 μM guanine (a) & 10 μM adenine (b) in water (1) then dried to induce aggregation and back in water (2)

Building on this use of nucleobases for our SERS studies, ssDNA was also selected as an analyte. A reverse selection primer with the following sequence, 5' TCA AGT GGT CAT GTA CTA GTC AA 3', was acquired from Dr. Christensen and

diluted to 1 μM followed by overnight exposure to a fresh 2D array. SERS was then obtained pre and post aggregation of the slide in water and the unscaled spectra can be seen in **Figure 4.7**. From this spectra we can see peaks at 796, 733 & 664 cm^{-1} . These match the previous peak positions obtained for the strongest peaks in adenine (733 cm^{-1}) and guanine (664 cm^{-1}). In addition the 796 cm^{-1} peak closely matches the literature value for cytosine (798 cm^{-1}).¹² The peak appearing at 1161 cm^{-1} increased in intensity with exposure to the analyte surface and would decay before increasing again when the surface was scanned, therefore being a result of a photo-effect on the sample. Photo-effects in the SERS spectrum of ssDNA have been investigated by Etchegoin *et al.* and have been attributed to an oxygen rich atmosphere by the Burstein mechanism in which the photon driven transfer of an electron from a metal state to an unoccupied molecular orbital of the adsorbate is enhanced by external causes (presence of oxygen in this case).¹³ When the samples in the Etchegoin study were placed under nitrogen, the peaks attributed to photo-effects enhanced by external causes disappeared.

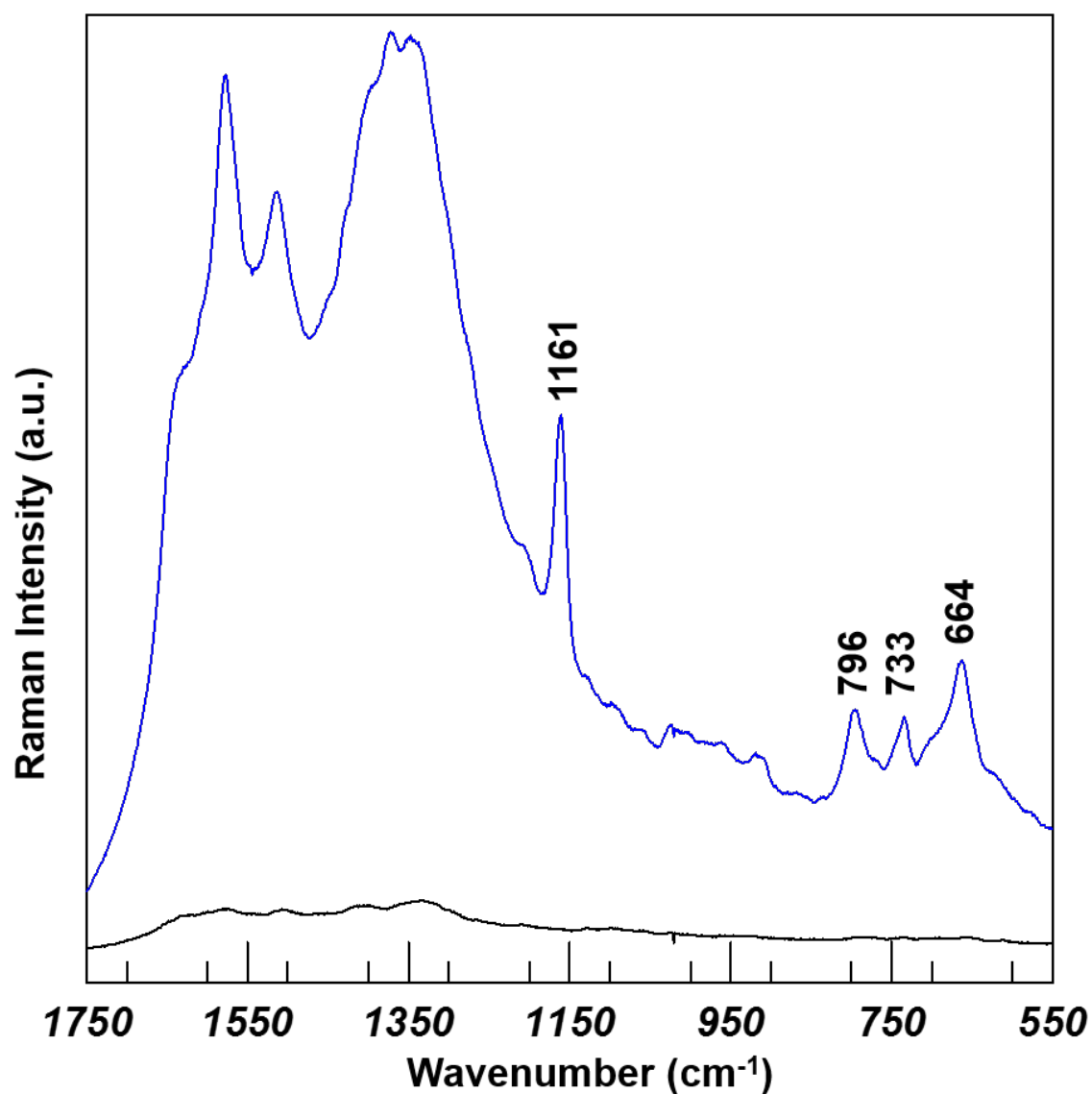


Figure 4.7 SERS of 1 μM ssDNA on 2D array of AgNPs before (black) and after (blue) drying. Spectra taken in water in both cases.

Lastly, these 2D arrays were used to investigate quinoxolinol salen ligands as selective ligands for uranium. To perform this, SERS of quinoxolinol ligand and the ligand bound to uranyl ion were obtained from samples provided by Anne Gorden at Auburn University. These ligands are insoluble in water and soluble in

acetone. This provided a unique opportunity for further application of the 2D arrays as SERS substrates since the AgNPs themselves would quickly aggregate in acetone but when assembled into the 2D arrays remained stable and were not affected by the acetone. 2D arrays were exposed to 10 μ M concentrations of the ligand and its complex with uranium (**Figure 4.8**) for 10 minutes before being removed, rinsed with acetone and then water followed by acquisition of SERS in water. Slides were then dried and placed back in DI water resulting in $\sim 10\times$ signal enhancement. A kinetic study was then performed to see how well these ligands bound the uranyl complexes since they are being investigated for their ability to detect uranyl species for environmental concerns.¹⁴ . As can be seen in **Figure 4.8** slides were monitored 10 minutes (a) after exposure, 1 day (b) and 4 days (c & d) with a, b & c showing the time evolution of the uranyl bound ligand while d represents the SERS of the ligand by itself which did not change over the course of the 4 days. The uranyl ion is highly stable and water-soluble and we can see the evolution of the SERS spectra as it starts to increasingly resemble that of the unbound ligand indicating release of the uranyl species into the DI water. This allows for identification of peaks associated with binding of the uranyl complex, some of which have been highlighted, which in turn can provide a possible identification mechanism for this species.

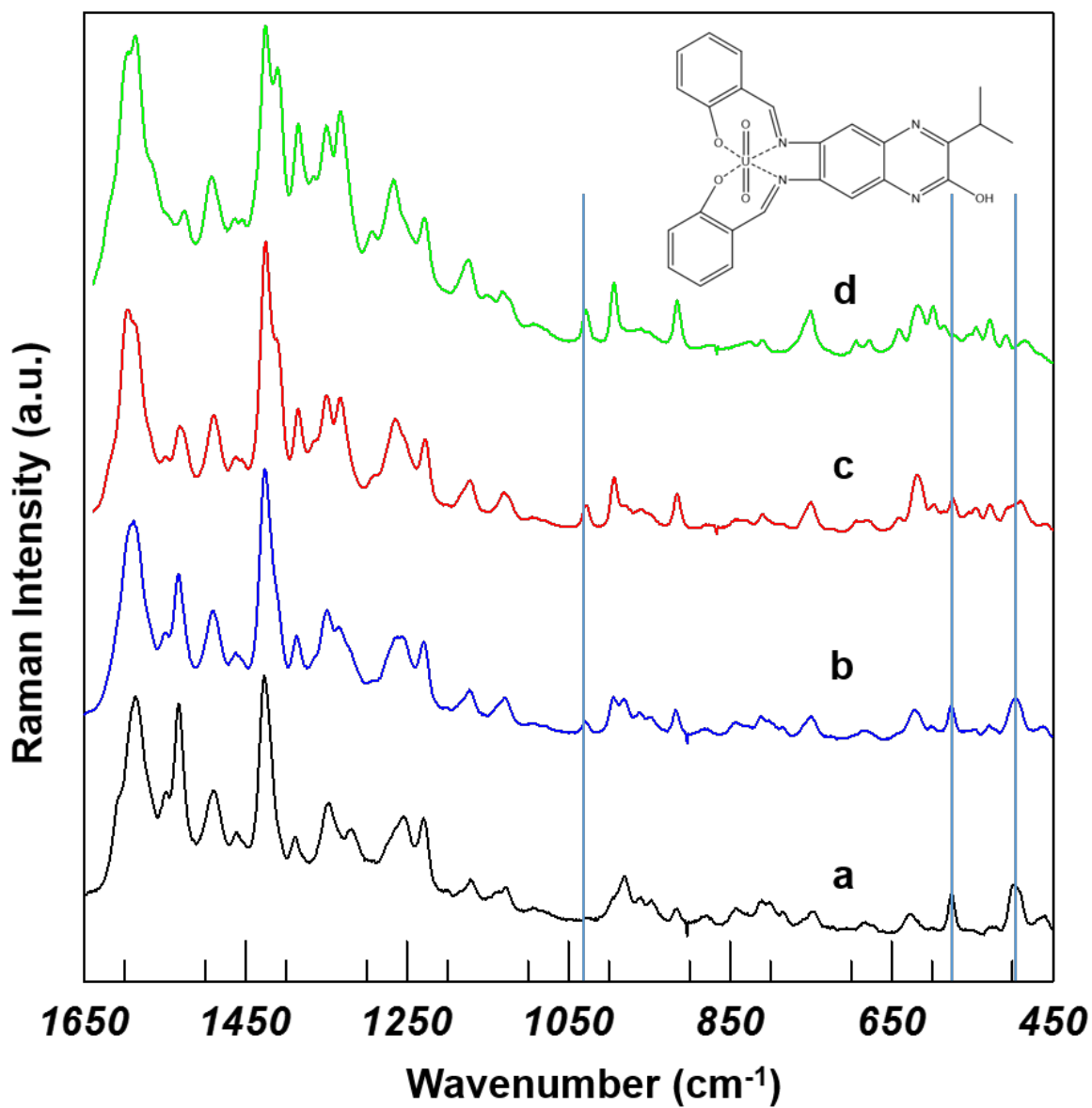


Figure 4.8 SERS of quinoxalinol salen ligand bound to uranyl ion after 10 minutes (a), 1 day (b) 4 days (c) and the ligand itself after 4 days (d) to show time release of uranyl species into DI water.

4.3.2 Chemiresistor Vapor Sensor

Another application that takes advantage of high concentration suspensions of AgNPs with ultra-thin silica shells relates to chemiresistor vapor sensors. The

high concentration of AgNPs allows the fabrication of high density films by a simple drop-casting and drying procedure. The ultra-thin silica shell provides a semi-insulating layer such that the overall electrical conductivity of the nanocomposite films can be controlled between the fully conducting metallic and fully non-conducting states by changing the thickness of the shell. In addition, the silica shell affords the sensing medium by either changes of its intrinsic properties or via chemical modifications, imparting the sensitivity to analytes of interest. Here, this sensor is illustrated by giving an example for sensing acetone and water vapors. The high density nanocomposite films were drop-casted from 2,500 O.D. (10%) AgNP suspensions with a 1-2 nm silica shell and dried between two ITO electrodes spaced ~1 mm apart yielding the measured resistance of several hundred Ohms after annealing overnight at 100 °C. As a result of the etching process, the ITO remains hydrophobic while the etched strip becomes hydrophilic allowing for easy fabrication of the sensing strip from an aqueous solution while still providing a connection between the two ITO electrodes. **Figure 4.9** provides an optical microscopy image taken under a 20x objective to show the particle distribution as the particles dry on the surface. A higher concentration of AgNPs can be seen on the edge as opposed to the center area and it is possible that repeated layering could improve the sensing response.

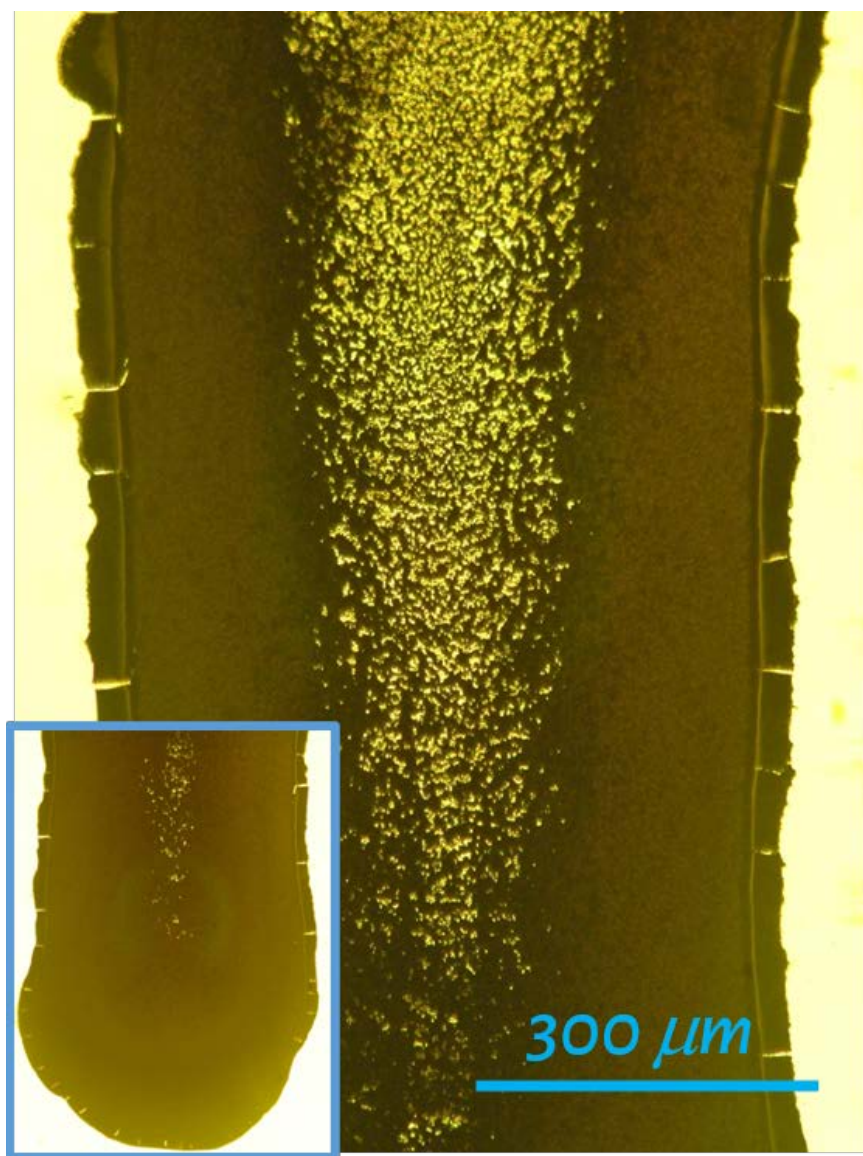


Figure 4.9 Photo of sensor taken on an optical microscope under 20x objective. Insert shows the AgNP distribution on the edges of the sensor.

Figure 4.10 provides an electron microscope image of a 2.5 μL drop of AgNPs dried on ITO. From this image we can see that instead of the monolayer coverage obtained for the 2D arrays used as SERS substrates, we now have a highly concentrated 3D nanocomposite film which provides the sensing area for our device.

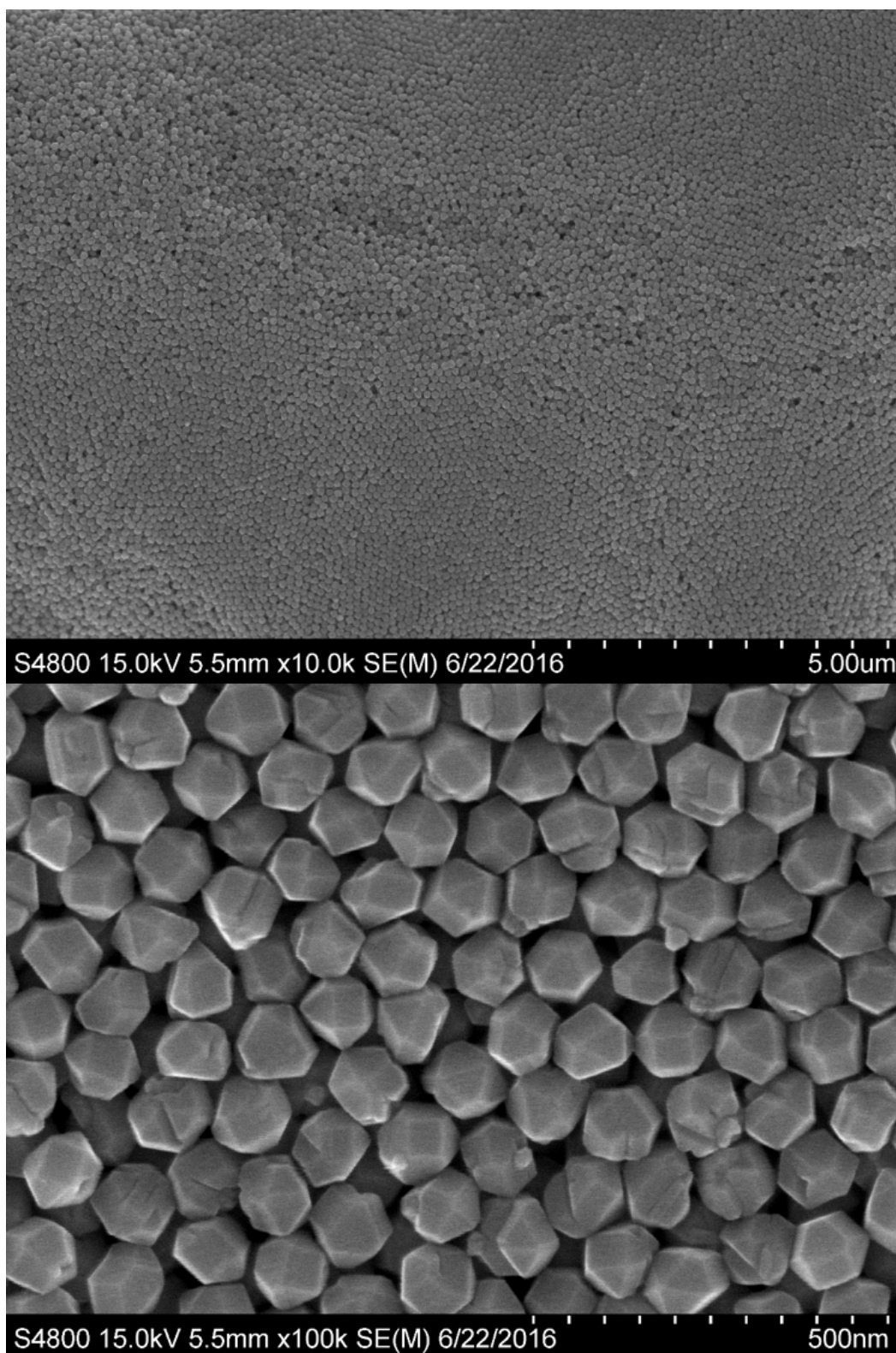


Figure 4.10 SEM of 2.5 μL of O.D. 2500 AgNPs (510 nm dipole) used to fabricate chemiresistor.

The current through the films was measured at 1 V potential difference as a function of time for the films at ambient conditions as well as films exposed to acetone and additional water vapor. As can be seen in **Figure 4.11**, a reversible and reproducible response was observed for both water and acetone vapors on top of the steady state decline of the overall current with time. The nature of this decline is currently under investigation and is hypothesized to result from voltage induced changes in the shell or oxidation of the silver surface. It was noted that the water and acetone vapor responses were out-of-phase due to the acetone vapor increasing conductivity and the water vapor decreasing conductivity. Acetone can act as a reducing agent. For acetone vapor sensing, it is known that sorption of oxygen plays a vital role in the electrical transport properties and therefore reduction of the oxygen species would generate electrons and increase conductivity. The reduction in conductivity as a result of exposure to water vapor can be attributed to swelling of the silica layer as it adsorbs the water vapor. Exposure to both analytes resulted in rapid responses in both directions within 10 seconds, this is particularly advantageous since comparable systems typically have response times on the order of hundreds of seconds. It is expected that various chemical modifications of the silica shell will extend the applicability of this simple chemiresistor sensor to different analytes of practical importance. The sensors also exhibited measurable response, albeit with a lower signal-to-noise ratio, when the applied potential difference was as low as 0.05 V (**Figure 4.12**). This property opens a possibility of operating the sensors in liquid environments

because fewer electrochemical reactions are expected at such low potential differences.

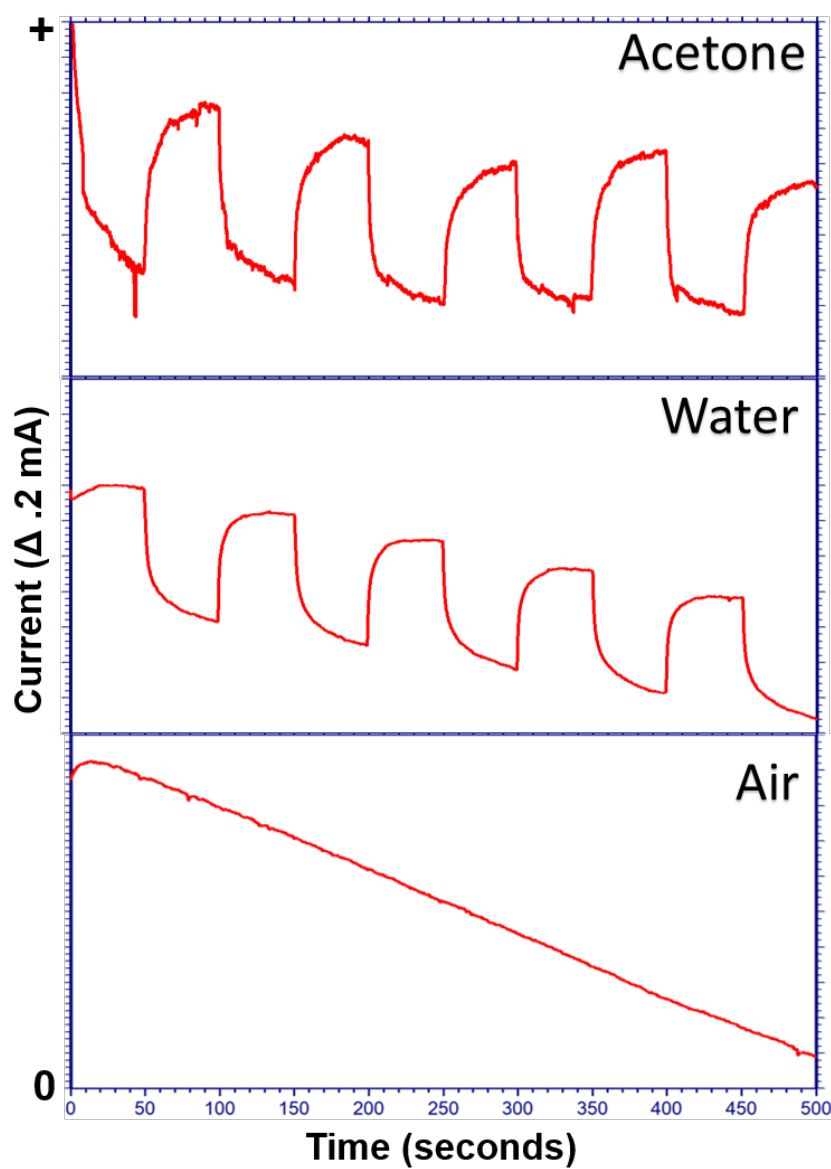


Figure 4.11 Conductivity response for air, water vapor & acetone vapor over a period of 500 seconds at a potential of +1 V. Water & acetone were introduced on and off for 50 seconds starting at 50 seconds to show reversible response.

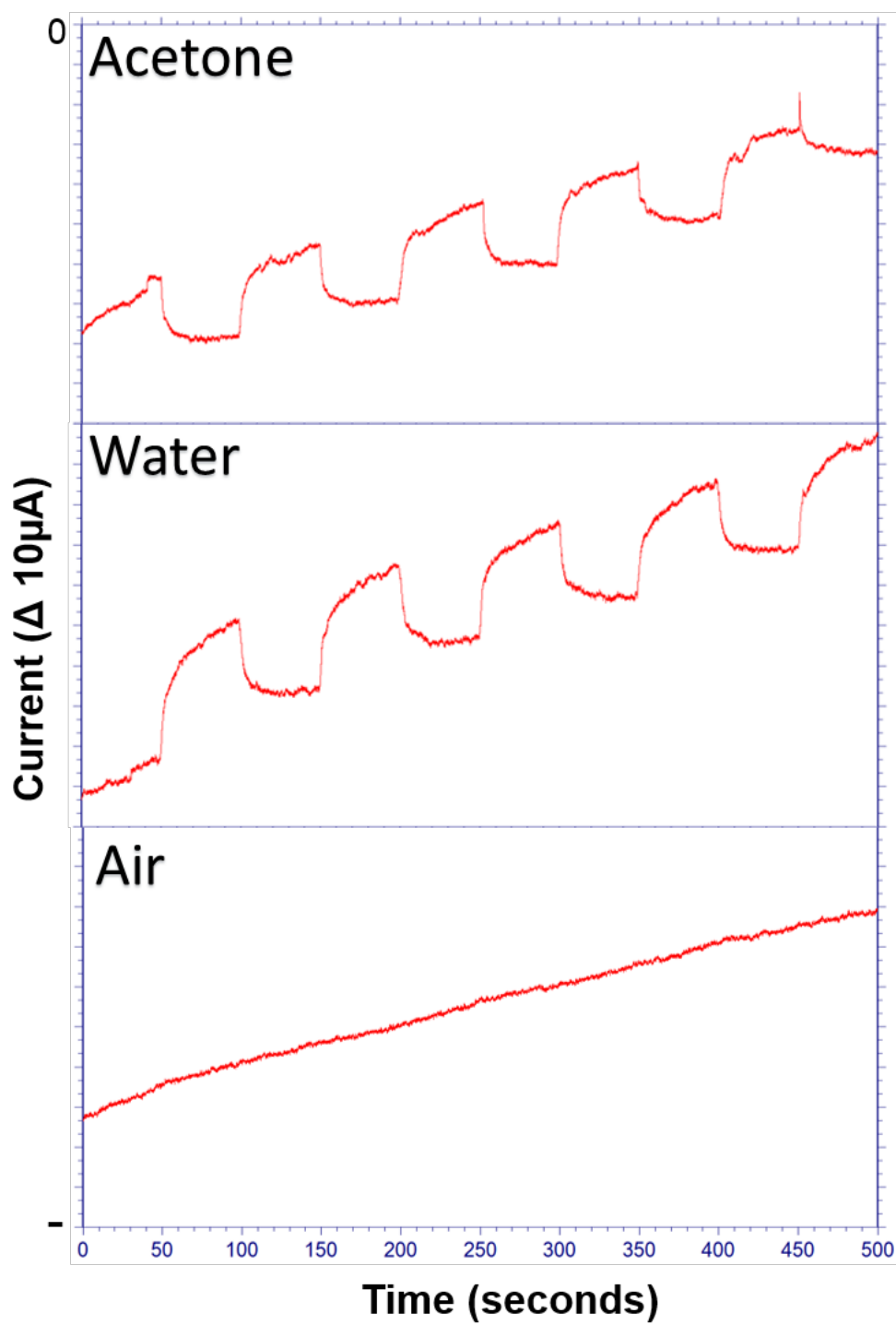


Figure 4.12 Conductivity response for air, water vapor & acetone vapor over a period of 500 seconds at a potential of -0.05 V. Water & acetone were introduced on and off for 50 seconds starting at 50 seconds to show reversible response.

4.3.3 *Fabrication of 2D & 3D Assemblies of AgNPs in a Polymer Matrix*

A final application that was explored for these AgNPs was their integration into 2D & 3D polymer matrixes. This originally came about due to outside interest in integrating these AgNPs into a light harvesting cladding in hopes of increasing the efficiency of photovoltaic fabrics under development. Previous work performed in this group involved fabrication of optically active flexible polymer films with embedded chain-like arrays of AgNPs.¹⁵ However, this was originally done by curing poly(dimethylsiloxane) (PDMS) on top of AgNPs assembled into 2D arrays followed by lifting off of the film. This leaves an exposed 2D array imbedded in the polymer matrix which could then be coated again to ensure stabilization. This means they couldn't simply be cast from solution and also resulted in relatively thick films due to the curing process of PDMS. The project required solutions that could be prepared with at least 20% water that would be stable and wet fibers that could then be drawn through a UV chamber for polymerization.

To accomplish this, AgNPs with both a ultra-thin silica shell for stability and a high concentration were required. To ensure stability the particles were first “conditioned” with a low concentration of PEGMDA prior to being made into the final solution. **Figure 4.13** shows the UV-Vis of the “conditioned” solution (black) which maintained the same resonance as that of original colloid and the resulting 10 nm dipole shift when it was added to achieve a final PEGMDA concentration of 80% (blue), these were then cast into a film and the UV-Vis was taken of the film showing that the AgNPs did not aggregate since the resonance (red) resembled

that of original colloid, but with a shifted dipole (550 nm) due to the higher refractive index of the local environment.

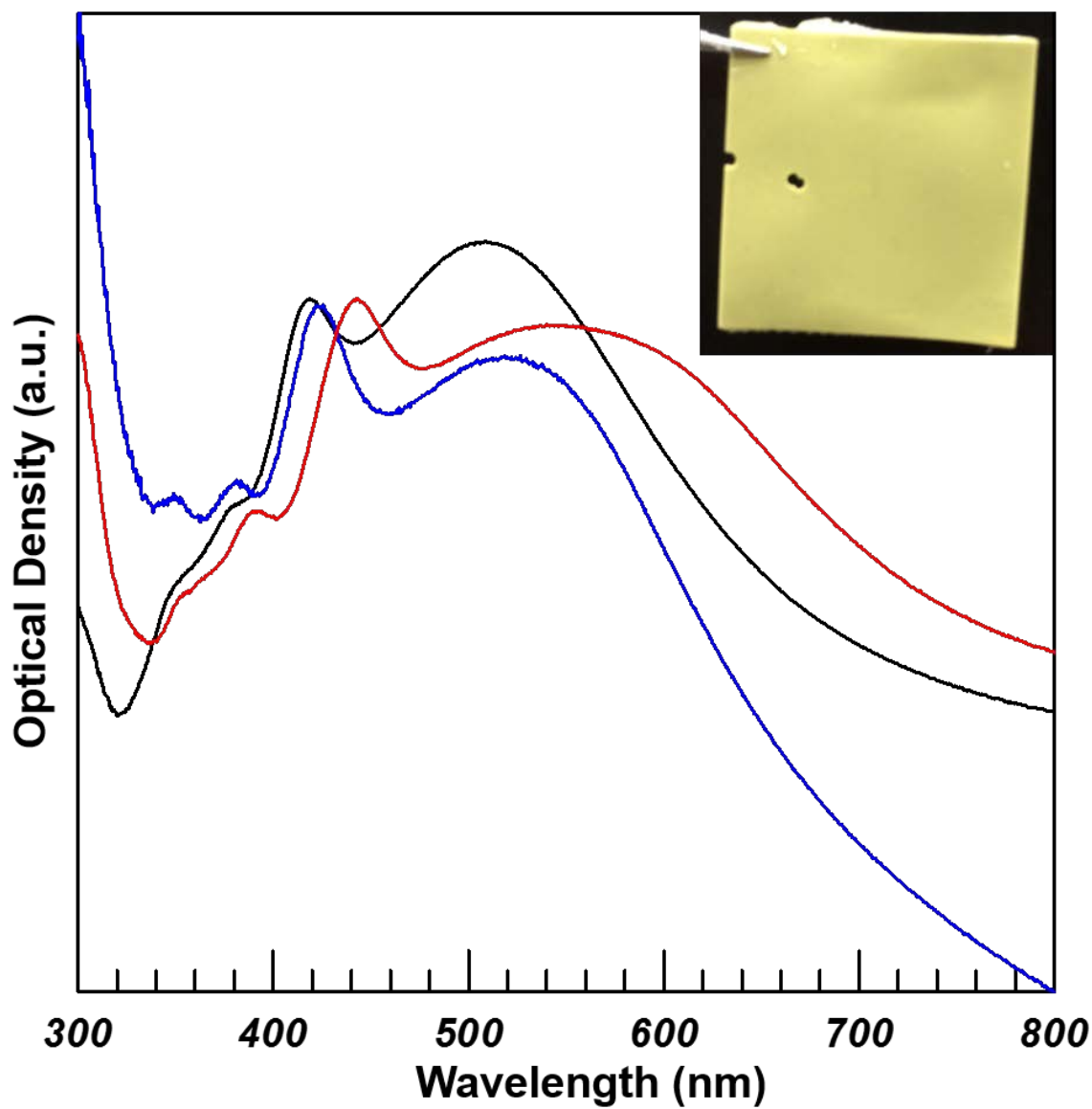


Figure 4.13 UV-Vis spectra of “conditioned” AgNP solution (black), prepared casting solution (blue) and polymerized film (red). Note: Spectra are offset to the quadrupole of “conditioned” solution for easier comparison of resulting shift.

To demonstrate that 2D arrays could also be achieved as well as the 3D matrix seen above, the lift-off technique in the previous publication was incorporated. **Figure 4.14** shows the UV-Vis progression as the slide transitioned from wet (black), to dry (blue) and finally embedded in polymerized PEGMDA film (red) where sharpness of the resonance was retained, indicated the AgNPs retained their 2D configuration, however unlike PDMS they are embedded in the film as shown by their stability when dipped in 10% nitric acid and also resulting in films much thinner and therefore more flexible than could be obtained by PDMS curing.

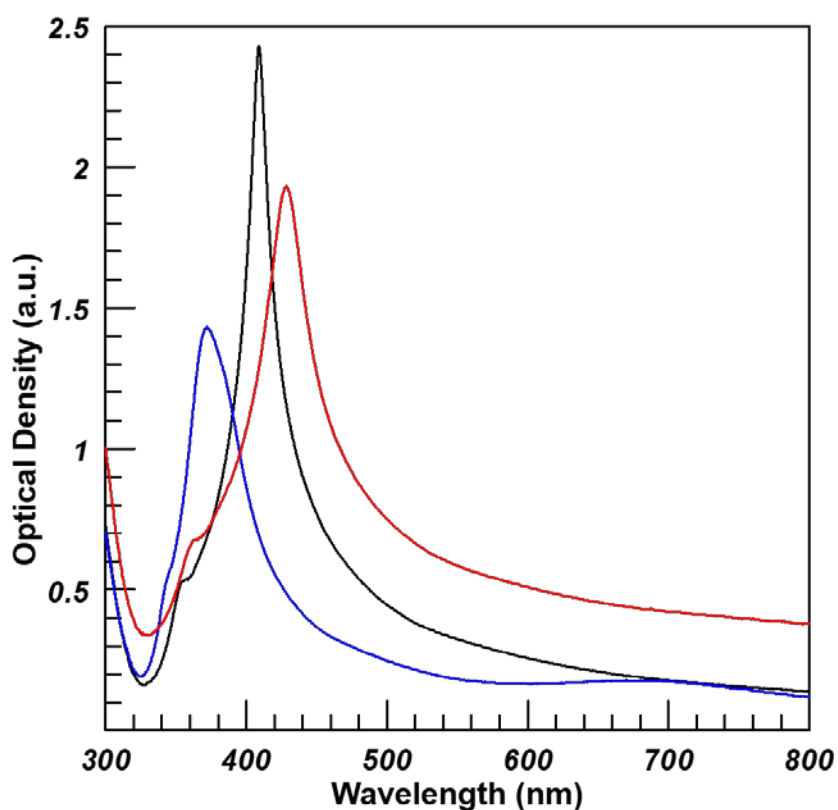


Figure 4.14 UV-Vis spectra of 2D array of AgNPs in water (black), dry (blue) and embedded into polymerized PEGMDA film (red)

4.4 Conclusions

The highly concentrated AgNPs with an ultra-thin silica shell synthesized in Chapter 2 have been integrated into a novel SERS substrate that allows for potential investigation of the chemical and EM enhancement components in addition to allowing for adsorptions of analytes in solvents that would normally induce AgNP aggregation. These AgNPs were also made into a simple chemiresistor with a unique matrix for gas vapor sensing. The AgNPs were immobilized in 2D & 3D assemblies in polymer matrixes for light harvesting applications related to photovoltaics. These preliminary results show promise for advancing the design and application of these two sensors into powerful analytical tools that will be explored further in this laboratory.

4.5 Acknowledgement

I would like to acknowledge Yi Jin for his assistance in assistance in etching the ITO & instruction in the use of the electrochemical workstation and Anne Gorden for providing the quinoxolinol salen ligands used in the uranyl study.

4.6 References

1. Raman, C. V.; Krishnan, K. S., A new type of secondary radiation. *Nature (London, U. K.)* **1928**, 121, 501-2.
2. (a) Albrecht, M. G.; Creighton, J. A., Anomalous intense Raman spectra of pyridine at a silver electrode. *J. Am. Chem. Soc.* **1977**, 99 (15), 5215-17; (b) Otto, A.; Mrozek, I.; Grabhorn, H.; Akemann, W., Surface-enhanced Raman scattering. *J. Phys.: Condens. Matter* **1992**, 4 (5), 1143-212; (c) Jeanmaire, D. L.; Van Duyne, R. P., Surface raman spectroelectrochemistry. *Journal of Electroanalytical Chemistry and Interfacial Electrochemistry* **1977**, 84 (1), 1-20; (d) Fleischmann, M.; Hendra, P. J.; McQuillan, A. J., Raman spectra of pyridine adsorbed at a silver electrode. *Chemical Physics Letters* **1974**, 26 (2), 163-166.
3. Le Ru, E. C.; Blackie, E.; Meyer, M.; Etchegoin, P. G., Surface Enhanced Raman Scattering Enhancement Factors: A Comprehensive Study. *J. Phys. Chem. C* **2007**, 111 (37), 13794-13803.
4. (a) Li, J.-F.; Tian, Z.-Q. In *Shell-isolated nanoparticle-enhanced raman spectroscopy (SHINERS)*, John Wiley & Sons Ltd.: 2014; pp 163-192; (b) Tian, X.-D.; Liu, B.-J.; Li, J.-F.; Yang, Z.-L.; Ren, B.; Tian, Z.-Q., SHINERS and plasmonic properties of Au Core SiO₂ shell nanoparticles with optimal core size and shell thickness. *J. Raman Spectrosc.* **2013**, 44 (7), 994-998; (c) Li, J. F.; Huang, Y. F.; Ding, Y.; Yang, Z. L.; Li, S. B.; Zhou, X. S.; Fan, F. R.; Zhang, W.; Zhou, Z. Y.; Wu, D. Y.; Ren, B.; Wang, Z. L.; Tian, Z. Q., Shell-isolated nanoparticle-enhanced Raman spectroscopy. *Nature (London, U. K.)* **2010**, 464 (7287), 392-395.

5. Franke, M. E.; Koplin, T. J.; Simon, U., Metal and metal oxide nanoparticles in chemiresistors: Does the nanoscale matter? *Small* **2006**, 2 (1), 36-50.
6. Lieberzeit, P. A.; Rehman, A.; Najafi, B.; Dickert, F. L., Real-life application of a QCM-based e-nose: quantitative characterization of different plant-degradation processes. *Analytical and Bioanalytical Chemistry* **2008**, 391 (8), 2897-2903.
7. Lloyd Spetz, A.; Tobias, P.; Unéus, L.; Svenningstorp, H.; Ekedahl, L.-G.; Lundström, I., High temperature catalytic metal field effect transistors for industrial applications. *Sensors and Actuators B: Chemical* **2000**, 70 (1–3), 67-76.
8. Wohltjen, H.; Snow, A. W., Colloidal Metal–Insulator–Metal Ensemble Chemiresistor Sensor. *Analytical Chemistry* **1998**, 70 (14), 2856-2859.
9. Saha, K.; Agasti, S. S.; Kim, C.; Li, X.; Rotello, V. M., Gold Nanoparticles in Chemical and Biological Sensing. *Chemical reviews* **2012**, 112 (5), 2739-2779.
10. Steinecker, W. H.; Rowe, M. P.; Zellers, E. T., Model of Vapor-Induced Resistivity Changes in Gold–Thiolate Monolayer-Protected Nanoparticle Sensor Films. *Analytical Chemistry* **2007**, 79 (13), 4977-4986.
11. Schatz, G. C.; Young, M. A.; Van Duyne, R. P., Electromagnetic Mechanism of SERS. In *Surface-Enhanced Raman Scattering: Physics and Applications*, Kneipp, K.; Moskovits, M.; Kneipp, H., Eds. Springer Berlin Heidelberg: Berlin, Heidelberg, 2006; pp 19-45.
12. (a) Bell, S. E. J.; Sirimuthu, N. M. S., Surface-Enhanced Raman Spectroscopy (SERS) for Sub-Micromolar Detection of DNA/RNA

- Mononucleotides. *J. Am. Chem. Soc.* **2006**, 128 (49), 15580-15581; (b) Otto, C.; Van den Tweel, T. J. J.; De Mul, F. F. M.; Greve, J., Surface-enhanced Raman spectroscopy of DNA bases. *J. Raman Spectrosc.* **1986**, 17 (3), 289-98.
13. (a) Burstein, E.; Chen, Y. J.; Chen, C. Y.; Lundquist, S.; Tosatti, E., "Giant" Raman scattering by adsorbed molecules on metal surfaces. *Solid State Communications* **1979**, 29 (8), 567-570; (b) Etchegoin, P.; Liem, H.; Maher, R. C.; Cohen, L. F.; Brown, R. J. C.; Hartigan, H.; Milton, M. J. T.; Gallop, J. C., A novel amplification mechanism for surface enhanced Raman scattering. *Chemical Physics Letters* **2002**, 366 (1-2), 115-121.
14. DeVore li, M. A.; Kerns, S. A.; Gorden, A. E. V., Characterization of Quinoxolinol Salen Ligands as Selective Ligands for Chemosensors for Uranium. *European Journal of Inorganic Chemistry* **2015**, 2015 (34), 5708-5714.
15. (a) Zdyrko, B.; Kinnan, M. K.; Chumanov, G.; Luzinov, I., Fabrication of optically active flexible polymer films with embedded chain-like arrays of silver nanoparticles. *Chemical Communications* **2008**, (11), 1284-1286; (b) Malynych, S.; Robuck, H.; Chumanov, G., Fabrication of Two-Dimensional Assemblies of Ag Nanoparticles and Nanocavities in Poly(dimethylsiloxane) Resin. *Nano Letters* **2001**, 1 (11), 647-649.

(blank)

CHAPTER FIVE

SUMMARY & FUTURE WORK

The aim of this dissertation was to investigate and improve the original synthesis of silver nanoparticles (AgNPs) by hydrogen reduction followed by exploring various applications that took advantage of the unique characteristics of these AgNPs. Chapter 1 outlines modifications to the synthesis that results in highly concentrated AgNPs with an ultra-thin silica shell. This work has been submitted to *RSC Advances*. It highlights both the importance of considering all aspects of a synthesis, including the glass surface of the reaction vessel, as well as introduces the idea of silica species catalyzing the seeding and growth of the AgNPs. Chapter 3 has been published by *Plasmonics* and is a detailed study of a novel method of detecting localized plasmon resonance shifts using differential measurements that takes advantage of the sharp plasmon resonance that occurs when these AgNPs are assembled into 2D arrays. Chapter 4 is unpublished work that explores the integration of these AgNPs into novel SERS substrates followed by preparation of simple chemiresistors with a unique matrix for vapor sensing along with 3D & 2D assemblies of the nanoparticles into a flexible polymer for light harvesting to improve photovoltaics devices.

The research presented here has established the base knowledge necessary to continue the work on both the utilization of the particles for shell-

isolated nanoparticle-enhanced Raman spectroscopy as well as development of easily prepared chemiresistors using a novel matrix. The original design of the chemiresistor was more proof-of-concept, since it was second to the synthesis itself, and has the most potential for further improvement. The LSPR sensor designed in Chapter 3 showed exceptional sensitivities to bulk refractive index, this indicates that sensing for local binding events should be even more promising due to the small sensing depth of LSPR systems. Future work for this system will involve miniaturization using a 405 nm LED with a prism, as well as the addition of a flow cell sample handling system, which is a standard approach in commercial instrumentation. Optimization of the detection system may include using a single detector with out-of-phase modulation of the optical channels. After this has been performed it will allow for the system to be applied to detection of analytes of practical importance rather than as a simple refractive index sensor.

Groundwork has also been laid to apply the differential LSPR system for quantification of an analyte on the 2D arrays of AgNPs followed by allowing them to dry to induce aggregation to then obtain relevant chemical information via SERS. In addition the substrates have potential for even greater SERS enhancement if prepared with the goal of SERS in mind and not focused on controlling inter-particle distance to generate a sharp resonance. The packing density has the ability to be greatly increased in the 2D array using increased nanoparticle and sulfate concentrations which should provide amplified SERS signal. This lay also lead into the ability to design a substrate for combing both SERS and chemiresistor

devices. Future studies will continue to optimize the preparation of these devices, determine the analytical figures of merits under various operating conditions, and use them to solve challenging analytical problems.

APPENDICES

APPENDIX A.

SYNTHESIS OF COPPER IODIDE NANOPARTICLES FOR DENTAL ADHESIVE APPLICATIONS

A.1 Introduction

Adhesive resins used currently in dental applications have not proven successful in preventing recurrent decay despite many advances made in restorative materials.¹ Over 70% of new dental restorations performed currently have been estimated as a result of a failure of a previous restoration.² A resin based composite (RBC) is the most commonly used dental restorative material due to their wear resistance and life-like esthetics, with the second factor being critical for most patients.^{1f} However, unlike alternatives such as high copper amalgam (HCA) fillings which have an average lifespan of 11-12 years, RBC fillings last an average of 6-7 years.^{1c, 3}

A major reason for fewer failures in HCA fillings can be attributed to the antimicrobial properties of the silver and copper used in these materials, especially in nanoparticle form attributing to a large surface to mass ratio.⁴ For copper nanoparticles the localized leaching of copper ions creates an infinite electron sink causes lysis in the homeostatic bacterial membranes.⁵ They are also relatively stable and less expensive than silver while still being easily incorporated into polymers. While they have a higher success rate and longer lifetime they still are

secondary to RBC in applications where esthetics are of importance, due to the discoloration caused by impregnating resins with these materials.⁶ Copper nanoparticles are especially egregious due to being black in color. To address these issues copper iodide nanoparticles were investigated due to being white in color and therefore having a negligible effect to the color of the materials to which they were added.^{5a} Polyacrylic acid (PAA) was used to coat the particles to act as a surfactant and for easier mixing in hydrophilic mediums commonly used in dental adhesive primers.

The copper iodide nanoparticles were used by the College of Dental Medicine at the Medical University of South Carolina and were shown to be a highly effective antimicrobial agent without negatively effecting the mechanical properties or colors of adhesive resins.⁷ As a result of their promising performance a patent was obtained for the incorporation of copper iodide into dental adhesives of which Dr. Chumanov is a listed holder.

A.2 Materials & Methods

A.2.1. Synthesis of PAA Coated Copper Iodide Nanoparticles

Copper(II) sulfate (Puratonic, 99.999% metal bases, Alfa-Aesar), potassium iodide (99.995%, Acros) and poly(acrylic) acid (50 wt% in water, MW=5000, Acros) were used as received. All solutions were prepared using deionized 18.2 MΩ water (Milli-Q, Milipore). In a typical reaction, 78.8 mL of 0.2M CuSO₄ was

combined with 7.8 mL of 20 wt% of PAA followed by an addition of 100 mL of 400 mM KI. Subsequently, more potassium iodide (50 mL of 400 mM) was added to drive the reaction to completion. The resulting white precipitate was washed with deionized water 4 times using centrifugation and dried under vacuum at 50°C. The powder was characterized by scanning electron microscopy (SEM) and energy dispersive x-ray (EDX) analysis using 4800 SEM (Hitachi). The resulting white powder showed stability for a period greater than 2 years stored in glass under ambient conditions.

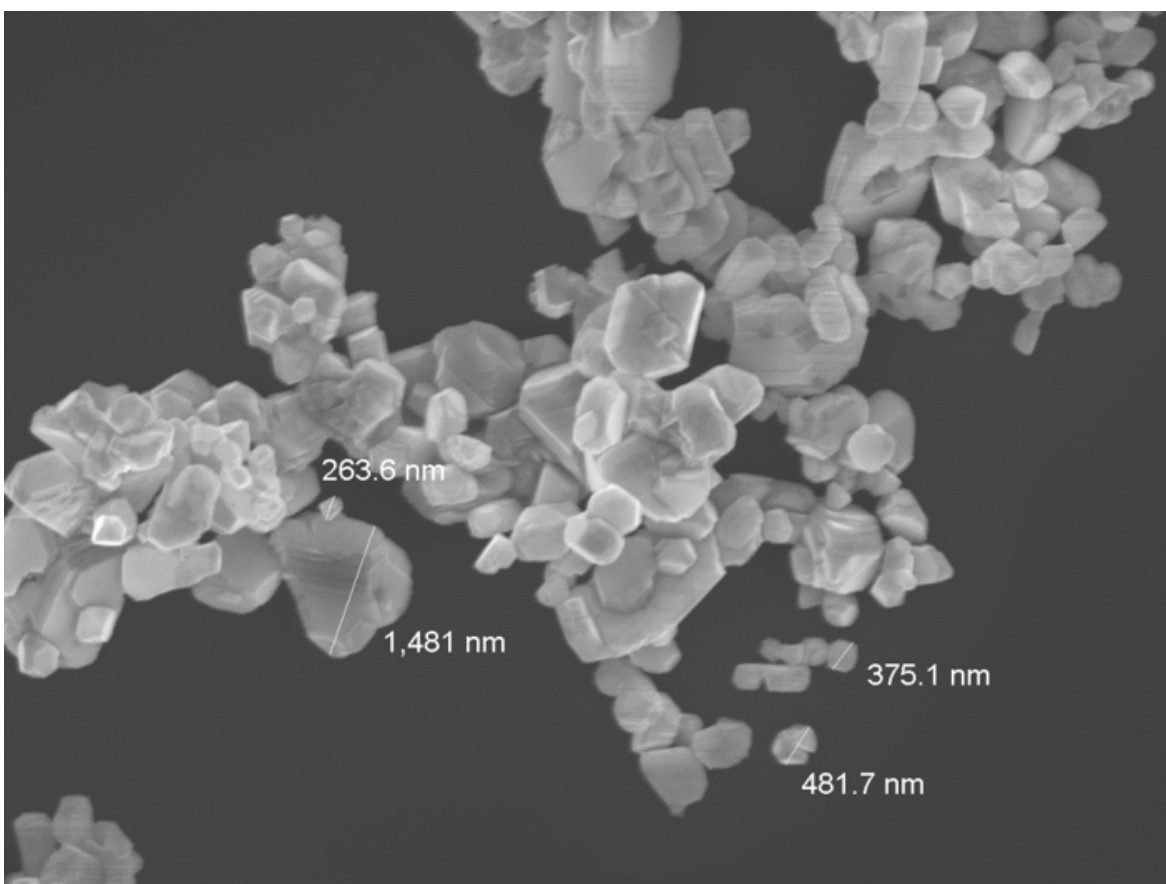


Figure A.1 SEM from the synthesized CuI nanoparticles demonstrating polydispersity in size.

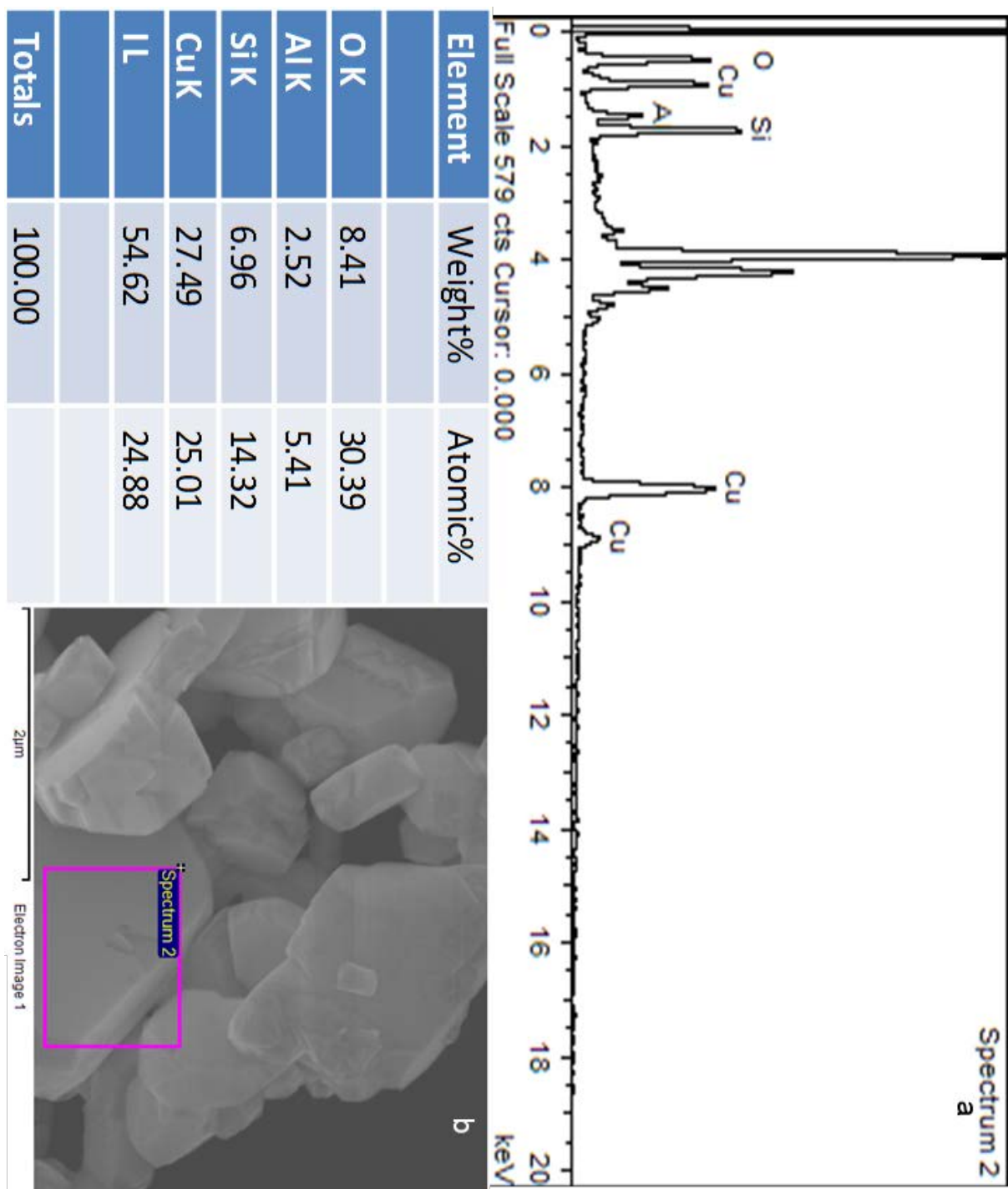


Figure A.2 EDX spectrum (a) from the selected area of the sample outlined by the magenta triangle (b). The measured elemental composition is in the figured table

A.3 References

1. (a) Beazoglou, T.; Eklund, S.; Heffley, D.; Meiers, J.; Brown, L. J.; Bailit, H., Economic impact of regulating the use of amalgam restorations. *Public Health Rep* **2007**, 122 (5), 657-63; (b) Bernardo, M.; Luis, H.; Martin, M. D.; Leroux, B. G.; Rue, T.; Leitao, J.; DeRouen, T. A., Survival and reasons for failure of amalgam versus composite posterior restorations placed in a randomized clinical trial. *J Am Dent Assoc* **2007**, 138 (6), 775-83; (c) Christensen, G. J., Should Resin-Based Composite Dominate Restorative Dentistry Today? *The Journal of the American Dental Association* **2010**, 141 (12), 1490-1493; (d) DeRouen, T. A.; Martin, M. D.; Leroux, B. G.; Townes, B. D.; Woods, J. S.; Leitao, J.; Castro-Caldas, A.; Luis, H.; Bernardo, M.; Rosenbaum, G.; Martins, I. P., Neurobehavioral effects of dental amalgam in children: a randomized clinical trial. *JAMA* **2006**, 295 (15), 1784-92; (e) Garcia-Godoy, F.; Krämer, N.; Feilzer, A. J.; Frankenberger, R., Long-term degradation of enamel and dentin bonds: 6-year results in vitro vs. in vivo. *Dental Materials* **2010**, 26 (11), 1113-1118; (f) Khalichi, P.; Cvitkovitch, D. G.; Santerre, J. P., Effect of composite resin biodegradation products on oral streptococcal growth. *Biomaterials* **2004**, 25 (24), 5467-72.
2. Murray, P. E.; Windsor, L. J.; Smyth, T. W.; Hafez, A. A.; Cox, C. F., Analysis of pulpal reactions to restorative procedures, materials, pulp capping, and future therapies. *Critical reviews in oral biology and medicine : an official publication of the American Association of Oral Biologists* **2002**, 13 (6), 509-20.

3. Mjor, I. A.; Dahl, J. E.; Moorhead, J. E., Age of restorations at replacement in permanent teeth in general dental practice. *Acta odontologica Scandinavica* **2000**, 58 (3), 97-101.
4. (a) Mohan, R.; Shanmugharaj, A. M.; Sung Hun, R., An efficient growth of silver and copper nanoparticles on multiwalled carbon nanotube with enhanced antimicrobial activity. *Journal of biomedical materials research. Part B, Applied biomaterials* **2011**, 96 (1), 119-26; (b) Orstavik, D., Antibacterial properties of and element release from some dental amalgams. *Acta odontologica Scandinavica* **1985**, 43 (4), 231-9; (c) Morones, J. R.; Elechiguerra, J. L.; Camacho, A.; Holt, K.; Kouri, J. B.; Ramirez, J. T.; Yacaman, M. J., The bactericidal effect of silver nanoparticles. *Nanotechnology* **2005**, 16 (10), 2346-53.
5. (a) Allaker, R. P., The use of nanoparticles to control oral biofilm formation. *Journal of dental research* **2010**, 89 (11), 1175-86; (b) Kim, Y. H.; Lee, D. K.; Cha, H. G.; Kim, C. W.; Kang, Y. C.; Kang, Y. S., Preparation and characterization of the antibacterial Cu nanoparticle formed on the surface of SiO₂ nanoparticles. *The journal of physical chemistry. B* **2006**, 110 (49), 24923-8; (c) Ruparelia, J. P.; Chatterjee, A. K.; Duttagupta, S. P.; Mukherji, S., Strain specificity in antimicrobial activity of silver and copper nanoparticles. *Acta biomaterialia* **2008**, 4 (3), 707-16; (d) Yoon, K. Y.; Byeon, J. H.; Park, J.-H.; Ji, J. H.; Bae, G. N.; Hwang, J., Antimicrobial Characteristics of Silver Aerosol Nanoparticles against *Bacillus subtilis* Bioaerosols. *Environmental Engineering Science* **2008**, 25 ((2)), 289-294.

6. Yamamoto, K.; Ohashi, S.; Aono, M.; Kokubo, T.; Yamada, I.; Yamauchi, J., Antibacterial activity of silver ions implanted in SiO₂ filler on oral streptococci. *Dental materials : official publication of the Academy of Dental Materials* **1996**, 12 (4), 227-9.
7. Sabatini, C.; Mennito, A. S.; Wolf, B. J.; Pashley, D. H.; Renné, W. G., Incorporation of bactericidal poly-acrylic acid modified copper iodide particles into adhesive resins. *Journal of Dentistry* **2015**, 43 (5), 546-555.

APPENDIX B.

SINGLE CRYSTAL RAMAN SPECTROSCOPY OF $\text{Ca}_{19}\text{Al}_{13}\text{Si}_{18}\text{O}_{71}(\text{OH})_7$

B 1. Introduction

The examination of single crystals by Raman spectroscopy is a powerful technique. Vibrational modes give rise to Raman scattering when a change in the polarizability of the crystal occurs during a vibration. The physical parameter for each mode described by the Raman tensor is subject to restrictions by the symmetry of the scattering system. This tensor may be used to predict directional properties and Raman activities.¹

B 2. Experimental

Raman measurements were performed using an Olympus IX71 inverted microscope with a 20x objective lens coupled to a TRIAX 552 spectrometer equipped with a thermoelectrically cooled CCD detector (Andor Technology, Model DU420A-BV) operating at -60 °C. An argon ion laser (Innova 100, Coherent) was used to excite the Raman signal with 514.5 nm light in a 180° backscattering geometry. A PR-550 broadband polarization rotator (Newport Corp.) was used to rotate the polarization of the incident laser source. All spectra were processed and figures prepared with Spectra-Solve for Windows software (LasTek Pty. Ltd.)

B 3. Discussion

A crystal of $\text{Ca}_{19}\text{Al}_{13}\text{Si}_{18}\text{O}_{71}(\text{OH})_7$ (vesuvianite²) with dimensions 0.25 x 0.08 x 0.08 mm was obtained from the Kolis group at Clemson University. It had a tetragonal symmetry with the unique 4-fold axis corresponding to the crystallographic c-axis. This corresponds to the longer dimension of the columnar crystal which was mounted to be parallel to the longitudinal direction of the glass fiber. The crystallographic a- and b- axis are identical and normal to the c-axis. The goniometer was placed in the micro-Raman set-up to obtain Raman spectra along the c-axis, **Figure B.1** provides an illustration of how this was performed along with optical microscopy image of the crystal with the incident laser beam along the c-axis.

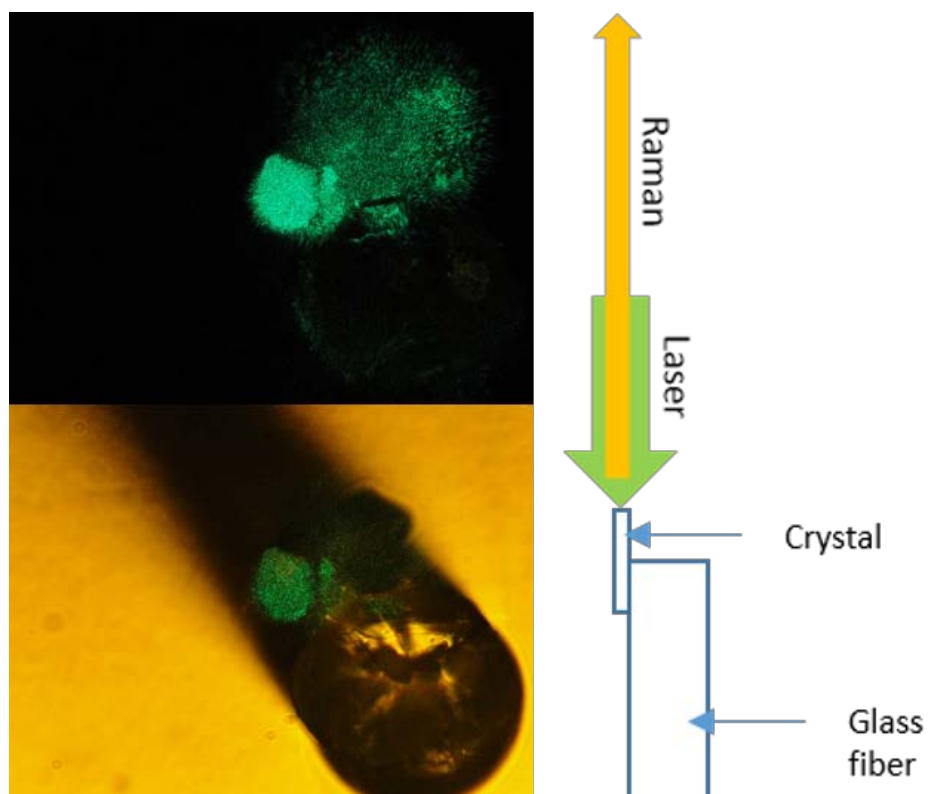


Figure. B.1 Schematic & microscope image illustrating laser illumination along the crystallographic c-axis using a 20x objective prior to micro-Raman measurements.

To obtain Raman along the identical a- & b-axis the goniometer was oriented according to the illustration in **Figure B. 2** in a head-on configuration with the optical microscopy images to show the exact area being probed. It is important to note that while the amorphous nature of the mounting epoxy has no effect on the x-ray data obtained, it does exhibit a large Raman signal. In order to account for this the Raman of the epoxy was first obtained on a glass slide and the resulting spectra was then subtracted from the Raman obtained in the head-on orientation. The epoxy provided no signal contamination when collected along the c-axis due to the small focusing depth associated with micro-Raman.

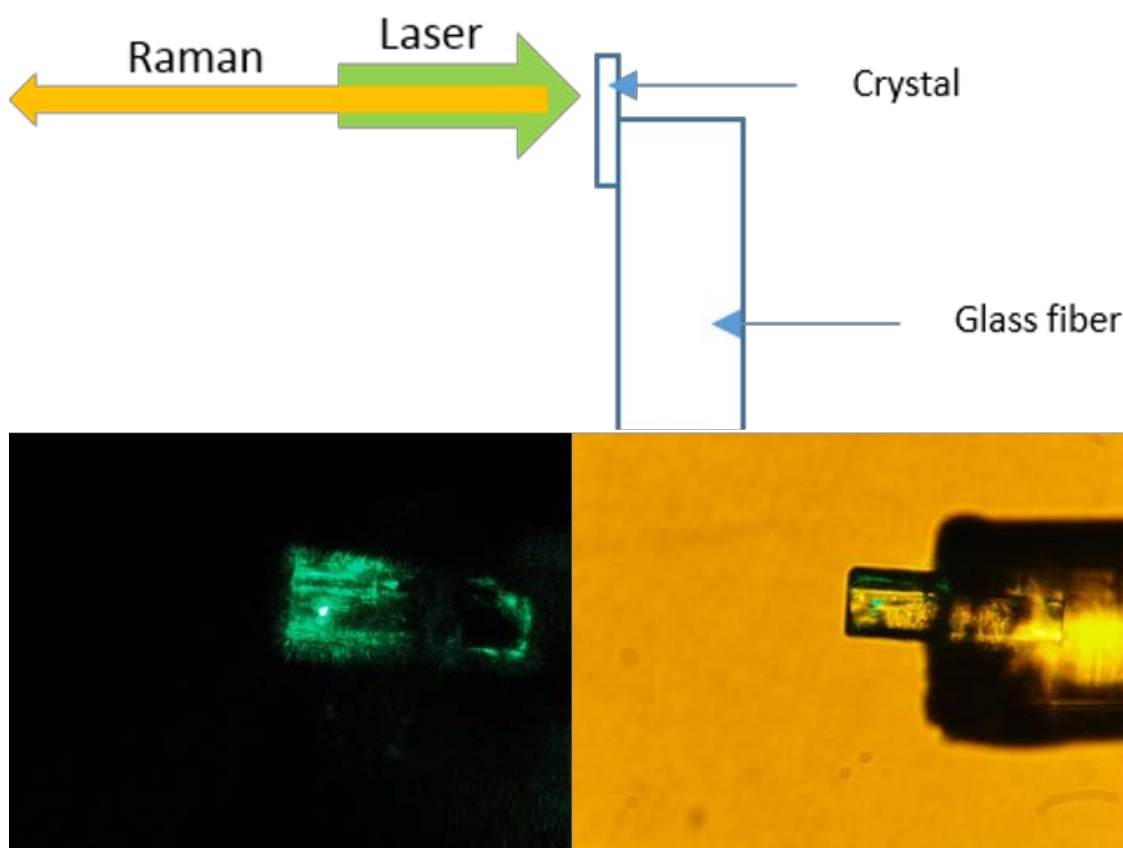


Figure. B.2 Schematic & microscope image illustrating laser illumination along the crystallographic a/b-axis using a 20x objective prior to micro-Raman measurements

The Raman obtained in both orientations using both P & S polarized light is presented in **Figure B.3**. In addition the literature values for vesuvianite available from the RRUFFTM database with P & S polarized light is presented.³ Good agreement can be seen between the literature values (E & F) and the obtained Raman. Discrepancies can be attributed to variances among elemental composition in vesuvianite samples. When oriented along the c-axis no observable difference is seen between the different polarizations of light. However when looking at the identical a- & b-axis noticeable difference in the sub-600 cm⁻¹ region appear. **Figure B.4** provides a zoomed in spectra of this region to highlight the differences. In particular the strength of the 365 cm⁻¹ peak seen under P-polarized light is diminished under S-polarization. This is in strong agreement with the literature spectra which demonstrates the same trend for P & S polarized light indicating it was probably taken under the same orientation though that information was unfortunately not reported on the RRUFFTM database. Another strong difference can be seen looking at the two peaks in the 590-650 cm⁻¹ region that are inverted in intensity from one polarization to the next. This helps to highlight the importance of obtaining high quality Raman of single crystals with carefully controlled polarization. Identification of the vibrational modes in these crystals excited by the different orientations of polarized light unfortunately requires outside computational modeling.

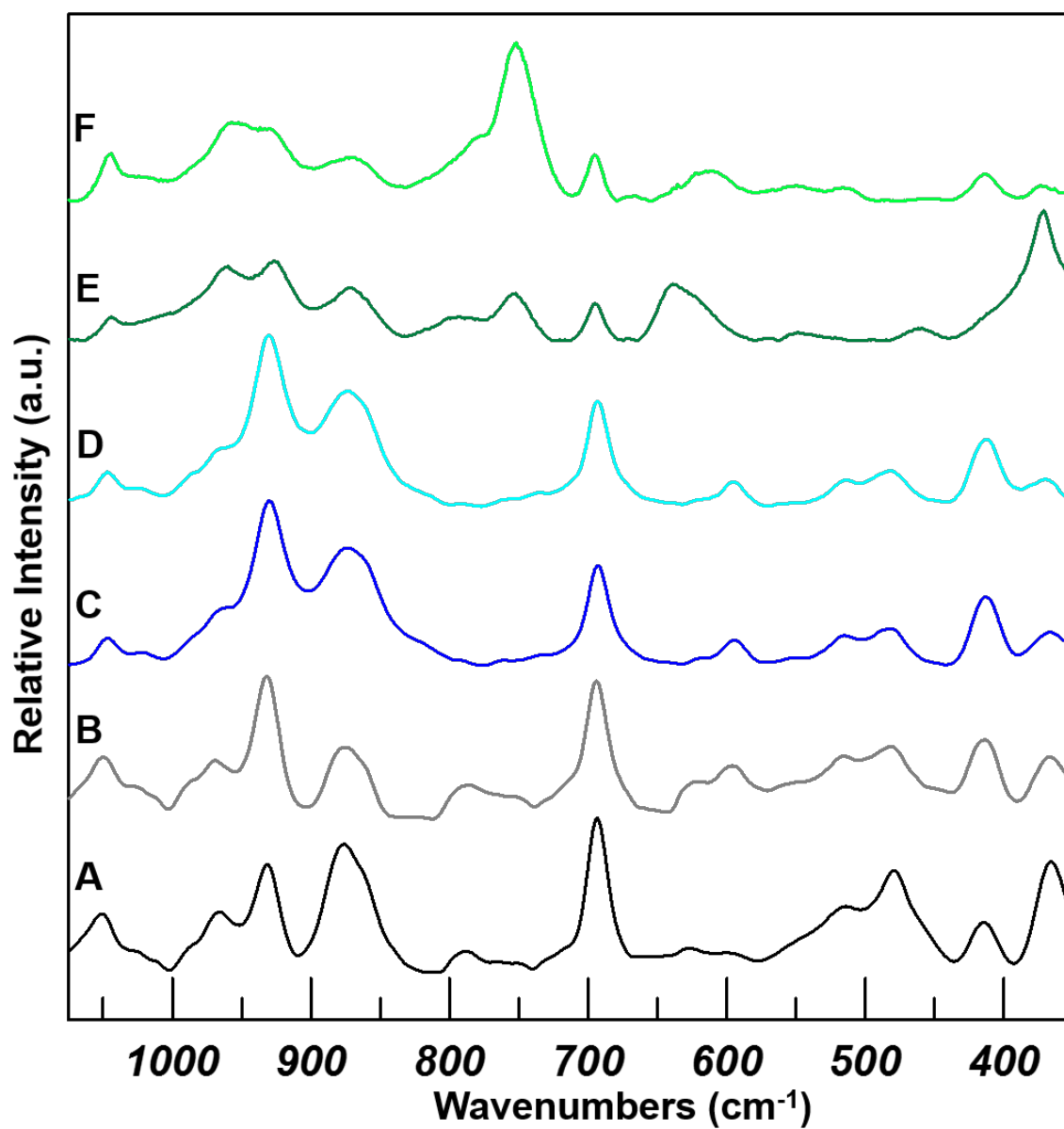


Figure. B.3 Raman of a/b-axis with P-polarized (A) & S-polarized (B) light. Raman of c-axis with P-polarized (C) & S-polarized (D) light. Literature Raman spectra of vesuvianite from RRUFF database for P-polarized (E) & S-polarized (F) light.

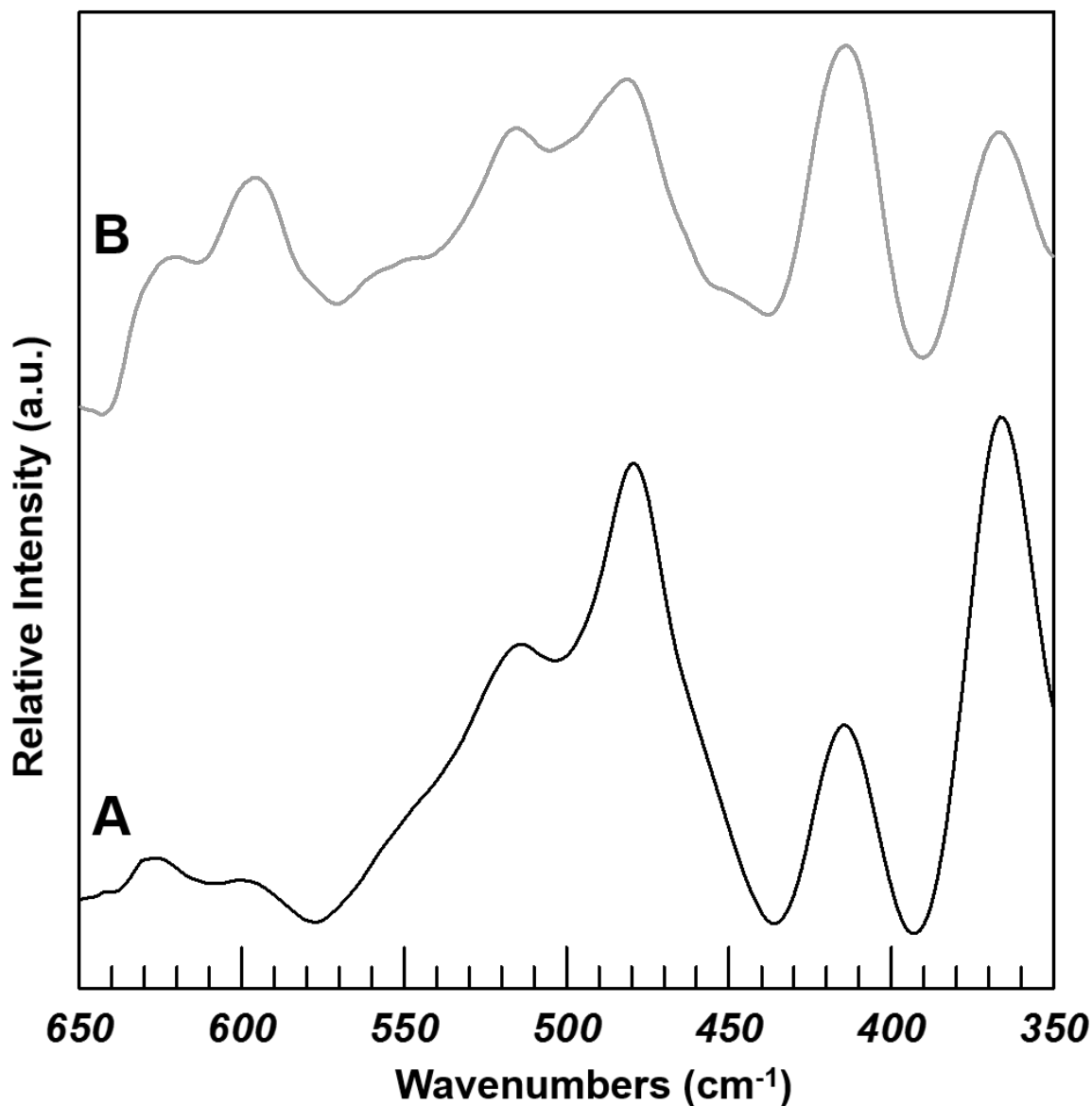


Figure. B.4 Zoomed in region of the Raman of the a/b-axis with P-polarized (A) & S-polarized (B) light to highlight the area with the most differences between the two polarizations.

B 4. Conclusion

In conclusion we have demonstrated the capability of our lab to obtain high quality Raman of single crystals. We have adapted our micro-Raman set up in such a way that a goniometer can be used to obtain x-ray data prior to being

taken to our lab and being directly placed into our system for Raman measurements along the desired axis and with the desired angle of polarization. This ease and speed with which this data can be acquisitioned opens the potential for rapid collaboration with research groups working on inorganic crystal synthesis. In addition it is hoped that this research will attract collaborations interested in modeling these vibrational modes for even more collaborative projects.

B 5. Acknowledgement

I would like to acknowledge Dr. Colin McMillen for his assistance in work with the single crystal Raman studies along with the Kolis group for preparation of the samples.

B 6. References

1. Swanson, B. I., Polarized Raman scattering from small single crystals. *Appl. Spectrosc.* **1973**, 27 (3), 235-7.
2. Paluszkiewicz, C.; Żabiński, W., Vibrational spectroscopy as a tool for discrimination of high and low vesuvianite. *Vibrational Spectroscopy* **2004**, 35 (1–2), 77-80.
3. Lafuente B, D. R. T., Yang H, Stone N, The Power of Databases: The RRUFF Project. In *Highlights in Mineralogical Crystallography*, Berlin, Germany, 2016.
1. Swanson, B. I., Polarized Raman scattering from small single crystals. *Appl. Spectrosc.* **1973**, 27 (3), 235-7.
2. Paluszkiewicz, C.; Żabiński, W., Vibrational spectroscopy as a tool for discrimination of high and low vesuvianite. *Vibrational Spectroscopy* **2004**, 35 (1–2), 77-80.
3. Lafuente B, D. R. T., Yang H, Stone N, The Power of Databases: The RRUFF Project. In *Highlights in Mineralogical Crystallography*, Berlin, Germany, 2016.
1. Swanson, B. I., Polarized Raman scattering from small single crystals. *Appl. Spectrosc.* **1973**, 27 (3), 235-7.
2. Paluszkiewicz, C.; Żabiński, W., Vibrational spectroscopy as a tool for discrimination of high and low vesuvianite. *Vibrational Spectroscopy* **2004**, 35 (1–2), 77-80.

3. Lafuente B, D. R. T., Yang H, Stone N, The Power of Databases: The RRUFF Project. In *Highlights in Mineralogical Crystallography*, Berlin, Germany, 2016.